Old Dominion University

ODU Digital Commons

Summer 2012

Development and Validation Methodology of the Nuss Procedure Surgical Planner

Krzysztof J. Rechowicz
Old Dominion University

Follow this and additional works at: https://digitalcommons.odu.edu/msve_etds

Part of the Biomedical Engineering and Bioengineering Commons, and the Surgery Commons

DEVELOPMENT AND VALIDATION METHODOLOGY OF THE NUSS

PROCEDURE SURGICAL PLANNER

by

Krzysztof J. Rechowicz
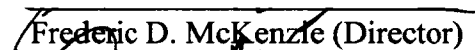M.S. January 2006, Warsaw University of Technology

A Dissertation Submitted to the Faculty of
Old Dominion University in Partial Fulfillment of the
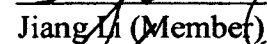Requirements for the Degree of

DOCTOR OF PHILOSOPHY
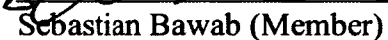
MODELING AND SIMULATION

OLD DOMINION UNIVERSITY
August 2012

Approved by:

Frederic D. McKenzie (Director)

Roland Mielke (Member)

Jiang Li (Member)

Sebastian Bawab (Member)

ABSTRACT

DEVELOPMENT AND VALIDATION OF THE NUSS PROCEDURE SURGICAL PLANNER

Krzysztof J. Rechowicz
Old Dominion University, 2012
Director: Dr. Frederic D. McKenzie

Pectus excavatum (PE) is a congenital chest wall deformity which is characterized, in most cases, by a deep depression of the sternum. A minimally invasive technique for the repair of PE (MIRPE), often referred to as the Nuss procedure, has been proven to be more advantageous than many other PE treatment techniques. The Nuss procedure consists of placement of a metal bar(s) underneath the sternum, thereby forcibly changing the geometry of the ribcage. Because of the prevalence of PE and the popularity of the Nuss procedure, the demand to perform this surgery is greater than ever. Therefore, a Nuss procedure surgical planner would be an invaluable planning tool ensuring an optimal physiological and aesthetic outcome.

In this dissertation, the development and validation of the Nuss procedure planner is investigated. First, a generic model of the ribcage is developed to overcome the issue of missing cartilage when PE ribcages are segmented and facilitate the flexibility of the model to accommodate a range of deformity. Then, the CT data collected from actual patients with PE is used to create a set of patient specific finite element models. Based on finite element analyses performed over those models, a set force-displacement data set is created. This data is used to train an artificial neural network to generalize the data set.

In order to evaluate the planning process, a methodology which uses an average shape of the chest for comparison with results of the Nuss procedure planner is

developed. This method is based on a sample of normal chests obtained from the ODU male population using laser surface scanning and overcomes challenging issues such as hole-filling, scan registration and consistency.

Additionally, this planning simulator is optimized so that it can be used for training purposes. Haptic feedback and inertial tracking is implemented, and the force-displacement model is approximated using a neural network approach and evaluated for real-time performance.

The results show that it is possible to utilize this approximation of the force-displacement model for the Nuss procedure simulator. The detailed ribcage model achieves real-time performance.

This dissertation is dedicated to my parents
for teaching me I could be anything in the world
I wanted to be

ACKNOWLEDGMENTS

Though only my name appears on the cover of this dissertation, a great many people have contributed to its production. I owe my gratitude to all those people who have made this dissertation possible and because of whom my graduate experience has been one that I will cherish forever.

My deepest gratitude is to my advisor, Dr. Frederic McKenzie. I have been amazingly fortunate to have an advisor who gave me the freedom to explore on my own and at the same time the guidance to recover when my steps faltered. His actions and support as my advisor and Graduate Program Director have, in many instances, exceeded the responsibilities defined by his position.

I would like to thank my committee members Dr. Sebastian Bawab, Dr. Jiang Li, Dr. Roland Mielke for their guidance over the years.

I would like to take this opportunity to thank Dr. Robert Kelly and his team members from the Children's Hospital of the King's Daughters for helping me understand aspects of the Nuss procedure and their work and providing constructive feedback about my work. A very special thank you to Amy Cohee, a former Pediatric Surgery and Pectus Research Coordinator, whose professionalism and kindness made data collection enjoyable and much easier.

A lot of problems would not have been solved without the help of Hector Garcia, Senior Project Scientist at VMASC and my friend. His knowledge, enthusiasm and integrity have always been an example to me.

I would like to thank those who, instead of giving advice, solutions, or cures, have chosen rather to share my pain and joy. Especially, I would like to express my highest gratitude to Helen Borges for her love and patience, Piotr Starzynski for being my

lifetime friend, Mariusz Balaban with his wife Dorota for opening their home and taking care of me far away from home.

My very special thanks to the people whom I owe everything, my parents, Małgorzata and Dr. Przemysław Rechowicz. It was them who planted the seed of curiosity and have been encouraging me in the pursuit of knowledge.

I would also like to thank my brother Jan and my sister Joanna for their love and support.

NOMENCLATURE

E Modulus of Elasticity, MPa

F Force, N

K Stiffness Matrix

TABLE OF CONTENTS

Page

LIST OF TABLES

LIST OF FIGURES

CHAPTER 1

INTRODUCTION

Pectus excavatum (PE) is a congenital chest wall deformity which is characterized, in most cases, by a deep depression of the sternum. This condition affects primarily children and young adults and is responsible for about 90% of congenital chest wall abnormalities [1]. Typically, this deformity can be found in approximately one in every 400 births [2].

A minimally invasive technique for the repair of PE (MIRPE), often referred to as the Nuss procedure, has been proven to be more advantageous than many other PE treatment techniques due to a short hospital stay, minimal trauma, and allowance for skeletal growth [2, 3]. PE patients that undergo minimally invasive surgery, report an improved ability to exercise, and measures of cardiac and pulmonary function show improvement in the long term [4,5]. The Nuss procedure consists of placement of a metal bar(s) underneath the sternum, forcibly changing the geometry of the ribcage. Apart from a physical improvement, positive psychological results are attributed to surgical correction [6, 7] because the normal shape of the chest is restored, reducing embarrassment, social anxiety, and depression associated with PE [8].

Because of the prevalence of PE and the popularity of the Nuss procedure, the demand to perform this surgery is greater than ever. Surgeons begin to perform this procedure often with little training after a single direct observation or even just with reading a written or verbal description. Therefore, a Nuss procedure surgical planner would be an invaluable planning tool ensuring an optimal physiological and aesthetic outcome.

1.1 Problem Statement

The Nuss procedure is a relatively simple surgical method but with a steep learning curve with several nuances. According to surgeons from the Children's Hospital of the King's Daughters, where the Nuss procedure was developed, an inexperienced surgeon goes directly from observing to practicing without supervision. Since the main goal of the procedure is to establish a physiological improvement and a positive aesthetic look of the chest, an appropriate shape and location of the bar underneath the sternum is crucial.

Interestingly, evaluation of aesthetic results is subjectively performed by a surgeon during the surgery, just after the surgery and/or after removing the bar [3]. Unfortunately, according to various patients who underwent the Nuss procedure in different facilities, the aesthetic outcome has not always been satisfactory [9]. An objective measurement of improvement and aesthetics along with a planning and training tool to achieve the desired outcome would provide surgeons needed training on the nuances of the Nuss procedure while serving as a guide to outline the best path to physiological and aesthetic success. Further, methods to objectively measure these results will provide the ability for surgeons to compare and improve patient specific approaches to surgery.

An objective measurement of the aesthetic outcome can be achieved by comparisons with an average shape chest derived from 3D scans of normal subjects. Seo *et al.* [10] pointed to several problems related to finding an average or normal shape and the directions in which the largest variability occurs in the whole human body or its parts

and organs. Before statistical analysis over a large sample of 3D object instances can be applied, chest surface scans have to be obtained and pre-processed, which includes hole-filling, scan registration, and shape vector creation. Even more useful would be to apply this technique before surgery in a surgical planner to predict better individual outcomes for the Nuss procedure.

Although surgical planners for various medical procedures have been a rapidly growing area of research, a surgical planner for the Nuss procedure has not been introduced to date and a training simulator is even more problematic because of the real-time requirements.

Nagasao *et al.* [11] simulated the Nuss procedure using finite element analysis (FEA) software for studying stress distribution in the ribcage after surgery. The authors came across problems with obtaining patient specific geometry of the ribcage using segmentation since the cartilage on CT slices is almost indistinguishable from the background. Additionally, mechanical properties have not been defined in vivo which makes FEA not fully reliable.

The approach presented in [11], while being suitable for scientific use, cannot be used by a person without engineering experience and requires dedicated computer aided design (CAD) and FEA software. Additionally, pre-surgical planning capabilities are still limited to two dimensional CT slices. 2D views give only a general idea concerning geometry of the PE ribcage and insufficient information to ensure appropriate geometry of the bar which is bent directly in an operating room to match particular chest geometry at the deepest point of depression. Therefore, the optimal aesthetic shape of the chest is not assured.

A Nuss procedure surgical planner would face similar obstacles as the ones found by Obaidellah *et al.* [12] when developing a finite element model (FEM) based maxillo-craniofacial surgical planner. Similar to the Nuss procedure, in maxillo-craniofacial surgery a positive aesthetic outcome is crucial for surgical success. However, the FEM approach presented in [12] cannot be executed in real-time since it is a computationally demanding task. Additionally, even though Berkley *et al.* [13] developed a FEM based suturing simulator working in a real-time-mode, this was only for small and low resolution models. Hence, using a FEM could be a barrier for an easy transition from a Nuss procedure surgical planner to a trainer simulator.

1.4 Methods and Procedure

The development of a Nuss procedure surgical planner is proposed which should utilize a patient specific ribcage and skin surface geometry. Moreover, a model of the ribcage should incorporate biomechanical properties specific for PE, and, since it is still an unresolved issue, such a planner should be able to accommodate new properties if new information becomes available.

Given the geometry and position of a bar, the planner will generate the deformation of the ribcage and the surface skin model will be visualized allowing subjective and objective aesthetic assessment of the outcome.

Instead of a subjective assessment performed by a surgeon in the planning process, objective evaluation of the simulated shape of the chest will be based on comparison with an average shape chest. The average shape chest will be obtained by means of statistical analysis over a set of normal surface scans.

Even though a real-time mode is not often required of surgical planners, such a capability would make a transition from the planner to a trainer simulator straightforward. Therefore, the planner will provide immediate feedback displaying the new geometry of the ribcage by finding a mathematical relationship between force and deformation using an approximation of FEM results.

The application will provide an easy to use interface without requiring engineering knowledge from a user. Furthermore, no additional software will be needed for routine use. However, updating the planner with new cases will require off-line modifications.

1.5 Contributions

There are three contributions as a result of this dissertation: an integrated Nuss procedure surgical planner, a training simulator for the Nuss procedure, and methods for validation and objective evaluation of aesthetic results.

1.5.1 An Integrated Nuss Procedure Surgical Planner

A finite element method and visualization engine are combined in order to provide a real-time methodology for surgical planning of the Nuss procedure. To date, there has not been a system supporting surgeon's decisions concerning location and shape of the bar taking into account the geometry of the patient's ribcage.

A target group for this system is less experienced surgeons who completed their training by observing how the Nuss procedure is performed or assisted in only a few cases. It would fill a gap in the learning process ensuring good aesthetic results in patients. Moreover, when more difficult cases are added, the application can be used by

experienced surgeons for evaluation of the developed plan by comparing the simulated shape of the chest with a normal one.

1.5.2 A Training Simulator for the Nuss Procedure

Because of the prevalence of PE and the popularity of the Nuss procedure, the need to perform this surgery is greater than ever. In this case, simulation would be an invaluable training tool to mitigate the steep learning curve of the Nuss procedure supplementing the training process.

Although the main purpose of the proposed system is the pre-surgical planning, it is possible to utilize it as a simulator of the Nuss procedure for basic training due to the real-time mode. In this case, instead of a particular patient's geometry of the ribcage, a surgeon can choose different cases of the PE deformation.

1.5.3 A Methodology for Validation and Objective Aesthetic Measurement

Statistical shape analysis in order to extract an average shape chest and directions in which the largest variability occurs has been used in many studies. However, they require a lot of preprocessing including utilization of a template mesh in order to maintain consistency among samples. The novelty of the proposed approach lies in converting each shape in a sample to a set of polylines and using points which define their segments to fit a polynomial which is later used to sample points which results in consistent shape vectors representing each scan.

This approach is suitable for 3D scanner data coming from partial scans of the body where the shape has no distinctive features. The result is a patient adjustable normal (average) shape. For validating the results of a specific case, the planner is compared

against the actual outcome. For an objective aesthetic measurement, the planner outcome

is compared to the average norm.

CHAPTER 2

BACKGROUND

To better understand the problem, attention needs to be focused on surgical simulation, including virtual and physical models, a surgery planning process, deformation of the virtual models and validation. Additionally, the pectus excavatum condition and the Nuss procedure need to be characterized in order to model the surgery with a high level of fidelity.

2.1 Surgical Simulation

No surgery is risk free. Even a fairly simple appendectomy has a death rate in the U.S. at a level of 1.5% [14]. However, risk can be minimized by developing appropriate surgical planning. Although, there is not a universally accepted definition of surgical planning, it can be regarded as a multilevel decision process in order to achieve the optimal treatment outcome. From the surgeon's point of view, it is the iterative cycle of designing or modification, simulation and evaluation, as well as anticipating any possible problems that may occur during the procedure (fig. 1) [15].

Nowadays, there is a trend in the U.S. to reevaluate the dominating model in surgical education – the apprenticeship, which is formalized in the form of residency. During this program, which requires 5 to 7 years to complete, a resident is trained by opportunity, i.e. s/he masters only those skills that are needed to treat cases s/he is subjected to in a clinic. Additionally, there are other constraints that can negatively influence the learning process of a resident: healthcare insurance providers favor outpatient surgery [16] making fewer patient contact hours available, frugal economic

models drastically reduce physician teaching time and regulations limit the number of hours a resident can work and the number of days that can be worked successively.

Figure 1. An iterative cycle of the surgical simulation process

Currently, the certification of surgeons focuses mostly on a written and an oral examination with a visible lack of an objective technical skills examination. Development of surgical simulators may address issues mentioned earlier. Simulation can provide scenarios with varying difficulty adjusted to the level of a resident. Additionally, simulators may ensure that skills of surgeons are quantifiable. Moreover, complex procedures may be practiced without endangering the patient and, lastly, students can practice on their own schedule reducing teacher-student time dependency.

2.1.1 Planning Simulations

Since in reality a trial and error method is very often not possible due to its non-reversibility, upon definition of the plan, it may be necessary to simulate the surgery on anatomically accurate models to select the best technical approach based on predicted

results [17]. In many cases, the design and simulation stage is performed in the same environment – a surgical planner. Surgical planners are typically concerned only with digital models and simulations. However, a surgery can be simulated utilizing a physical model and real tools.

Simulation with physical models can be performed directly in an operating theater. It is most suitable for procedures where cutting, fixing or placing implants are involved (fig. 2). This approach allows better "look and feel" than digital simulations and does not require a computer to perform the simulation. However, each model can be used only once, and different material properties are hard to simulate.
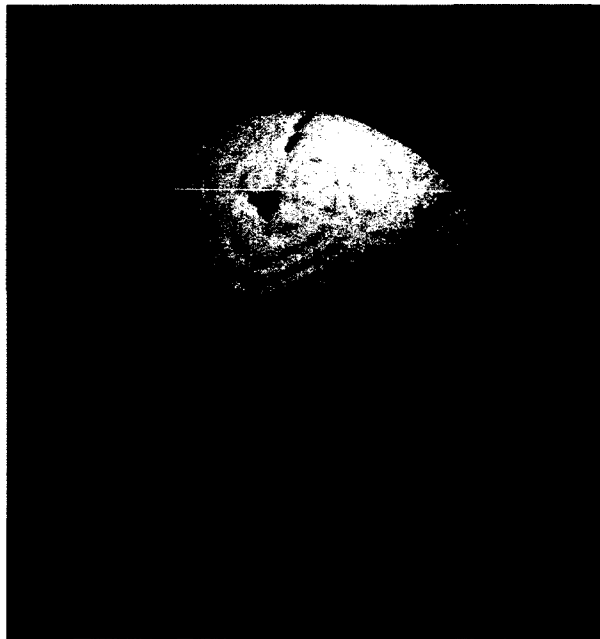
Figure 2. Pre-surgical rehearsal on a physical model

Another approach is based completely on computer simulations (fig. 3). In contrast to simulations based on physical models, this approach provides unlimited views, freedom of dissection, in situ linear and volume measurement, low cost and reuse.

The main purpose of the volume of interest definition is to prepare a strategy for accessing the target, especially, if it cannot be approached in a straight line, like when a curvature trajectory is required due to necessity of avoiding critical normal regions. Rendered 3D representations of the possible entry areas are also of interest in order to avoid oversized openings, which happen during traditional planning procedures [15].

Figure 3. Pre-surgical rehearsal on a physical model ©[2007] IEEE

A very important aspect of surgical planning lies in the possibility of avoiding damaging healthy tissue. It plays a key role in prescribing dosage in brachytherapy where catheters and seeds are defined and modified based on the calculation of dosage distribution. Dosage should cover as much of the target volume and only the target volume as possible.

Each plan can be modified in three ways: automatically, semi-automatically and manually by a surgeon. Automatic optimization can be done by translating the objective of a surgery into a cost function. By its minimization, the most efficient and safest approach can be calculated.

2.1.2 Planner Design Considerations

Development of an intervention strategy for each part of the operative procedures (devising a route to approach the target, bone cutting angles, location of screws, etc.) starts with analyzing individual data of each patient. Before development of 3D imaging methods, a surgeon used to base surgical planning on 2D images – cross-sectional X-rays, and extrapolate them mentally into 3D. Nowadays, a surgeon can plan surgical approaches in the virtual environment or utilizing physical models.

A 3D model representing volumes of interest (VOI) is typically comprised of medical images such as Computed Tomography (CT) and Magnetic Resonance Imaging (MRI), using segmentation methods.

Digital geometry processing is used in CT to generate voxelized three-dimensional images of the internals of an object from a large series of two-dimensional X-ray data slices taken around a single axis of rotation, whereas MRI uses a powerful magnetic field to align the nuclear spin of usually hydrogen atoms in water in the body. Radio frequency fields are used to systematically alter the alignment of this magnetization, causing the hydrogen nuclei to produce an alternating magnetic field detectable by the scanner. This signal can be manipulated by additional magnetic fields to build up enough information to construct an image of the body. Even though it is possible

to obtain surface models, both techniques are primarily used to collect information about internal organs.

In the case of collecting surface data from a patient, 3D optical scanners are the most suitable devices. A 3D optical scanner is a device that analyzes a real-world object or environment to collect data about its shape and possibly its appearance. Many different technologies can be used to build these 3D scanning devices; each comes with its own limitations, advantages and costs. It is also possible to combine a surface model, like face or chest, with a solid model of a structure inside a patient's body, like the skull or cartilage.

In addition, anatomical physical models, which require the apriori creation of virtual counterparts, have been successfully used for surgical planning in maxillofacial surgery, reconstructive surgery, heart surgery, and orthopedic surgery [18-20]. In early years, physical models were manufactured using machine milling, other techniques where material is removed to obtain the desired shape, or casting. However, the development of additive 3D printing techniques in the late 80s, called rapid prototyping (RP), changed the view on how physical models are made.

In surgical planning utilizing physical models, a virtual model is typically converted to the triangular mesh and then converted to a set of perpendicular cross-sections. Each cross-section or layer is printed separately according to each RP technique. As a result, a 3D physical model is obtained, which may require further post-processing, such as infiltration, curing or sanding.

Figure 4. Intra-operative use of the physical model

Physical models (fig. 4) do not require significant spatial perception from surgeons and make structural conflicts more apparent than virtual models that actually are 2D projections. An existing physical replica can be used for preparation of a fixation plate or an implant when needed, which is impossible with a digital model. However, in terms of time and costs, physical models are not as efficient as digital ones, making digital models more attractive in surgical planning.

2.1.3 Deformable Models for Surgical Planning

Based on a review of papers, the easiest simulation method for surgical procedures where by changing the underlying bone structure an aesthetic goal is achieved similarly to the Nuss procedure, is to simply rotate and translate objects in CAD or other 3D visualization software. It applies mostly to bone cutting and changing the position of its fragments [21].

In order to better meet the requirements of interactivity and motion realism, deformable objects in surgical simulation have been an emerging trend in recent years. Figure 5 presents a classification of different deformable models adopted from Meier *et al.* [22] and supplemented by techniques currently gaining popularity.

Of the existing models, the most important are mass-spring models (MSM), finite element modeling (FEM) and boundary element models (BEM). A MSM is a mesh where edges represent springs, characterized by stiffness, and nodes represent discretized mass points. Equilibrium state can be expressed using Newton's law of motion:

$$m_i \frac{d^2 s_i}{dt^2} + b \frac{ds_i}{dt} + f_i^{\text{int}} = f_i^{ext}, \tag{1}$$

where m_i is the mass of node i, s_i the current position of that node, b the damping coefficient of the adjacent springs, f_i^{int} the internal force acting on node i and f_i^{ext} is the external force applied to the node i. The internal force is trying to maintain the initial position of the latter with respect to the nodes with which it is connected through springs. Equation (1) is solved by discretization into intervals, typically with finite Euler differences [23]. This method requires the utilization of small intervals to account for stiff objects. It can be solved by employing the Runge-Kutta technique.

Simplicity and easy implementation are the main advantages of MSMs. Since each node depends only on its nearest neighbor, it allows the representation of even great deformations with high realism. In addition, any topological manipulations like incisions are easily represented, as the modifications in the system of equations are very confined. Nonetheless, when cutting into volumetric objects, their interior still has to be created [24].
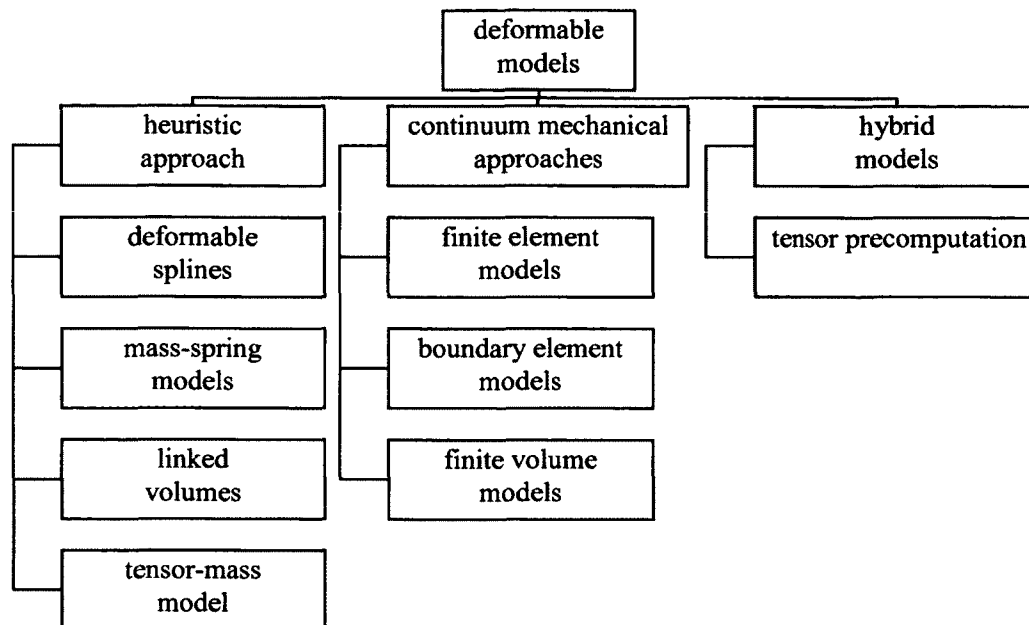
Figure 5. Taxonomy of deformable models for surgical simulation

The local structure of MSM delays the rapid global propagation of deformations, which causes a visibly limited volumetric behavior. An object modeled in this way does not even approximately maintain a constant volume, and when acting on one of its sides, the opposing side only reacts after a noticeable delay. This effect is more visible in the softer objects undergoing large deformation, thus limiting the realism of large deformations.

A MSM also has a tendency to oscillate affecting realism, and a conversion of the solution largely depends on the selection of an appropriate time step and on the parameters of the mesh. Therefore, they have to be determined experimentally each time. If a simulation requires removing and/or adding springs, it is extremely difficult to establish a new set of parameters. Moreover, convergence of the whole system may be affected.

The other example of modeling deformable objects is the finite element method. Originally, FEMs were developed to approximately solve differential equations defined for a certain domain with some corresponding boundary conditions. For structural analysis, an object is divided into a finite number of elements. Then, the displacement is approximated with polynomial equations over each element and is represented as a function of the values at some corresponding control nodes.

Using an assumption of linearity, the system of equations is in the form of:

$$KU = F, \qquad (2)$$

where K is the symmetric and sparse stiffness matrix, U is the nodal displacement matrix and F is the matrix with force vectors.

Typically, there is no force associated with most of the nodes and displacements are unknown. The nodes that are in contact with a tool have their displacement set, but the resultant force is unknown. Therefore, almost all entries in F are zero with the exception of some unknown values for the contact nodes. U is mostly comprised of unknowns with only a few known values. It leads to reordering of (2) every time the set of nodes with boundary conditions assigned changes in order to group all the known and unknown values together. Then, U refers to the vector of unknown values and F refers to the vector of known values.

If the mechanical properties of a studied body are defined, a system is relatively easy to solve. The main issue remains the time needed for computations which almost solely depends on the algorithm utilized. This problem is solved by simplifications, mainly to the underlying mechanical models.

In order to overcome issues related to FEM, BEM attempts to use the boundary conditions to fit their values into the integral equation, rather than values throughout the

space defined by a partial differential equation. Once this is done, the integral equation can be used to calculate the solution directly at any desired point in the interior of the solution domain. The boundary element method is often more efficient than other methods, including finite elements, in terms of computational resources for problems where there is a small surface to volume ratio.

For the linear case, a system is described by the set of equations equivalent to (2):

$$BU = GD, \tag{3}$$

where the influence matrices B and G are of significantly smaller size than the stiffness matrix K in the FEM case. However, typically, they are fully populated and are not symmetric or positive which could make calculations simpler. U and D are the nodal displacement and surface force vectors, respectively.

The BEM approach is just as robust and quick as the FEM, and both techniques branch from the same linearly elastic assumption so that their realism is equally limited for large or rapid deformations. However, BEM tends to give even more exact results than FEM, in particular for force peaks like those created with the tips of surgical instruments. The same applies to topological changes, in which case, the matrix has to be modified as well to consider new, additional nodes. Thus, local incisions can be represented but with some moderate computational effort.

Modern technology in interactive computer graphics has enabled the building of dedicated simulators or surgical planners. The major premise for their use is that many medical conditions are not alike as there are significant differences in human physiology. This is an important point in maxillo-craniofacial surgery where deformities are not identical and, despite a surgeon's experience, require a specific plan for each case. In addition, surgical planners allow the prediction of the aesthetic and/or physiological

outcome of the surgery which is a very important aspect of surgical planning for some procedures.

Variability in the location, size and type of pathologies is another motivation for simulators. The right choice of defined trajectory of a surgical tool, volume for resection, or the optimal seed location can be improved by simulating each aspect.

2.1.4 Validity

Surgical simulators utilize models that are simplified approximations of real organs, tissues and tools. Even though it is possible to create geometrically accurate digital models using current medical imaging modalities, it has been pointed out that developing accurate biological models for surgical simulation is still challenging. Biological tissues are generally inhomogeneous, anisotropic, and viscoelastic, and require complex experimental techniques to measure accurate tissue characteristics in a laboratory. Further, development of organ models requires measurement of tissue properties in vivo, since organs have significantly different dynamics due to variations in temperature and blood circulation, which are impossible to precisely replicate during ex vivo experiments. Moreover, the task of choosing an appropriate constitutive law that describes the stress–strain response of the tissue under various loading conditions is not straightforward [25].

The validity of a simulation can be increased by reflecting surrounding structure, tool-tissue interaction and behavior of a tool. However, research is currently limited to two dimensions due to the amount of computational power needed to simulate the behavior of the mesh under pressure and its rendering at rates of 10 to 20 times per second in order to produce realistic video [26].

2.1.5 Evaluation of a Surgical Procedure

After simulation, surgeons have accurate information concerning possible surgical processes for the planned strategy. Based on the outcome of a simulation, a surgical plan is evaluated whether it is the final approach or it needs further refinements.

In reality, the definition of success for each actual surgical procedure differs. Typically, the first assessment is provided by a surgeon, based on his experience. Since this kind of evaluation is subjective due to variation in surgeons' preferences, quantifiable methods are used if possible. Measurements, physical and performance tests, comparisons with a standard condition are examples of objective evaluation. This is still challenging since in many cases a reference has not yet been established.

Evaluating the outcome of a simulation suffers from the same limitations since it mimics real actions. However, there are some additional constraints when long term observations or measurements of patient's performance are required to fully assess results. Therefore, the evaluation of a surgical strategy is based mainly on visual assessment and direct measurements.

If a surgical plan is the best among others, the surgical planning process is finished and can be applied during surgery. If refinement is necessary, the whole cycle is repeated again from the modification stage.

2.2 Pectus Excavatum

Pectus excavatum (PE), also called sunken or funnel chest, is a congenital chest wall deformity which is characterized, in most cases, by a deep depression of the sternum. This condition affects primarily children and young adults and is responsible for about 90% of congenital chest wall abnormalities [1]. Typically, this deformity can be

found in approximately one in every 400 births [2] and, since it occurs in families, is inherited in many instances. In addition, PE affects males five times more often than females. This deformation can be seen just after birth and develops over time to its maximum extent after the growth period. Unaided-improvement of this condition is observed very rarely due to the fixation of cartilages and ligaments.

For the objective assessment of PE, a classification method was developed based on various charts, preoperative photographs, and CT scans [27]. The method consists of a set of six focus points describing each patient's deformation: Haller index (fig. 6), asymmetry index – rib cage right side diameter to rib cage left side diameter multiplied by 100, relative length of depression to sternum, fraction of the sternum affected, degree of sternal torsion-angle of deviation between the line of the sternum and the transverse diameter of the ribcage, and localized versus diffuse morphology.
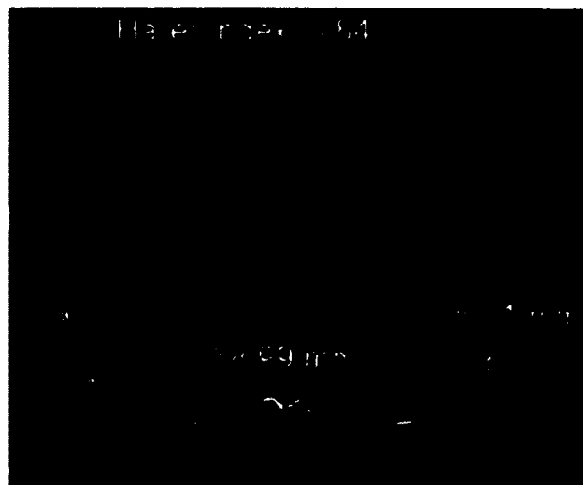
Figure 6. Haller index calculated from a CT scan, HI=265.01/68.99=3.84

The advantage of characterizing the morphology of PE is that it allows the practitioner a more controlled approach to diagnosis and could possibly support in the determination of treatment options. In addition, these objective measures can help to eliminate ambiguities in and reliability of PE diagnosis.

PE often limits respiratory and cardiac function of the patient's body. The sternum is very frequently pushed back toward the spine and is asymmetric - it courses to the right (most frequent), or left in this depression. This deformation also pushes the midline structures so that the lungs and the heart are compressed. Additionally, the heart can be displaced due to the pressure of the sternum. On the contrary, some researchers report that surgical treatment of PE does not necessarily lead to the significant improvement of pulmonary function [28]. Moreover, while teenagers with PE have a lower tolerance for exercise, it cannot be categorically attributed to PE. Testing 36 teenagers in order to establish whether the PE deformity results in cardiopulmonary problems and the effects of surgical treatment showed that while exercise tolerance and blood oxygen saturation improved, the correction had no effect on the present restrictive lung disease [29].

Other studies have found that PE patients that undergo minimally invasive surgery report an improved ability to exercise, and measures of cardiac function show improvement [4]. In this case, patients also showed a decline in pulmonary function after surgery and follow-up measures in [5] showed improvement that did not reach normal levels. This improvement in pulmonary function was not compared with previous patient values.

Contrary to these findings, a number of studies, including a meta-analysis of past research efforts, have found that surgical correction of PE does result in not only subjective physiological improvement, but also improvement in objective measures as well [6, 28, 30, 31].

The investigated psychological aspects of PE showed that the effects of PE affect all areas of life because they can manifest as embarrassment, social anxiety, and depression [8]. Such reactions begin at a very early age and become more serious as the patient gets older. As such a life disturbance can be an indication for long-term psychological counseling, the authors state that permanent correction in the form of surgery can often alleviate the tediousness of this process. In [4], the psychological effects of PE in addition to its physical manifestations are listed and other researchers attributed positive psychological results to surgical correction in [6] and [7]. However, psychological premises for physical intervention are not always taken into account due to their subjectivity. For example, if certain functional criteria are not met, an insurance company may consider corrective surgery for PE to be cosmetic and deny coverage [32].

As shown above, physiological effects of PE pre-surgery and improvements post-surgery is a largely controversial area of study. While the focus of PE effects on the patient is important to the growing body of knowledge, many studies lack the broad analyses necessary to draw strong conclusions. As a result, it is clear that there remains a strong need for further investigation and analysis of the causes, treatment, and effects of PE.

2.2.1 Treatment of Pectus Excavatum

There have been a number of procedures developed over time to cure or camouflage the PE deformity, including rib resection, sternoturnover and funnel costoplasty, chest wall implants, the vacuum bell, and Nuss' MIRPE.

Although, over the years, the approach to the repair of PE has evolved, currently two procedures are mostly used to treat this particular chest deformity – the Ravitch procedure and the much later introduced Nuss procedure.

Rib resection, known also as the Ravitch procedure, had been successfully used with modifications since 1941 [33]. It consists of resecting all deformed costal cartilages from the sternum and performing a lateral wedge-shaped osteotomy on the sternum where the downward slope begins. The repositioned sternum is then sutured into place, and the incision is closed, leaving a large scar across the chest.

Other, lesser known, corrective procedures are the sternoturnover and the funnel costoplasty [34]. In the sternoturnover procedure, the sternum is disconnected from the surrounding cartilages, tissues, and mammary arteries, then flipped over and flattened by a number of osteotomies. The sternum is sutured back in place using steel wire, and the adjacent cartilages are sutured to one another using silk cable.

In the funnel costoplasty, all deformed costal cartilages are disconnected from the sternum and multiple wedge resections are imposed, resulting in straightened cartilages. Results of these procedures were highly successful with satisfactory results.

Another approach, recognized as positive both subjectively and clinically speaking, was placing first generic and then patient specific chest wall implants [35-39].

One non-surgical PE correction is the vacuum chest wall lifter, also known as the vacuum bell, which uses negative pressure to pull the depression anteriorly away from the spine. Research accounts of this approach state that consistent daily application of this treatment can greatly improve the appearance of PE, with limited cases making a full recovery [40, 41].

2.2.2 The Nuss Procedure

In 1987, Dr. Donald Nuss of the Children's Hospital of the King's Daughters, Norfolk, VA, in cooperation with Walter Lorenz Surgical, Inc., developed the minimally invasive technique for the repair of pectus excavatum (MIRPE), often referred to as the Nuss procedure [3]. In contrast to the other techniques that modify the costal cartilages and/or sternum by resection, the Nuss procedure is minimally invasive. A steel bar is used to elevate the sternum, thereby correcting the deformity over time.

In the beginning of the surgery, small bilateral incisions are made in the chest wall at the deepest point of the depression. Using a metal introducer, the surgeon opens a pathway from the incision, up underneath the skin to the chest cavity entry point, under the sternum, taking care not to puncture the lungs or heart, back through the ribs out of the chest cavity and down the opposite incision, trailing a piece of umbilical tape (fig. 7a). After leaving the chest, the tape is fixed to the end of the steel bar, previously bent to suit the patient (fig. 7b). Then, the bar is pulled through the pathway until the tape can be removed through the first incision. At this time, if the position of the bar is correct, the surgeon can slowly elevate the bar to loosen the cartilage connections to the inner thorax (fig. 7d). After this step, the concave bar is then flipped convex so that the arch elevates and supports the sternum in a normal position. The bar is then sutured into place, often

with the addition of a stabilizer to prevent movement. When PE is severe or when a patient is adult, a second and even a third bar may be inserted. After a period of at least two years, the bar is removed, resulting in a largely permanent result.

Post-operative assessment, performed by a surgeon, patient and parents, is typically subjective in regards to an aesthetic improvement [42, 43]. CT is not typically included in a post-operative follow-up protocol. Therefore, objective measures, like the Haller index, cannot be easily obtained. However, an anthropometric index, measured on a patient, was proven to have high correlation with the Haller index and to be an efficient comparison between the pre-operative measurement and the post-operative results [44].

The Nuss procedure has revolutionized the surgical treatment of PE. The advantage is a short hospital stay, minimal trauma, and allowance for skeletal growth [2]. However, the main aesthetic advantage is the presence of short bilateral scars as compared to a long one in the middle of the chest from the Ravitch procedure.

There are some disadvantages of the Nuss procedure mentioned in various publications. Cost is increased due to usage of thoracoscopy and associated equipment [2] which is a reason for some institutions to avoid using video guidance. However, in a review of this approach it is "extremely risky" with possible complications being "difficult to foresee" [42]. The cost of equipment is reduced by using aftermarket tools and bars. This may be unintentional since the original Lorentz equipment has not been approved by local authorities in some countries [42]. Other disadvantages mentioned are the necessity of the bar removal surgery and possibility of capnothorax in thoracoscopy [2].
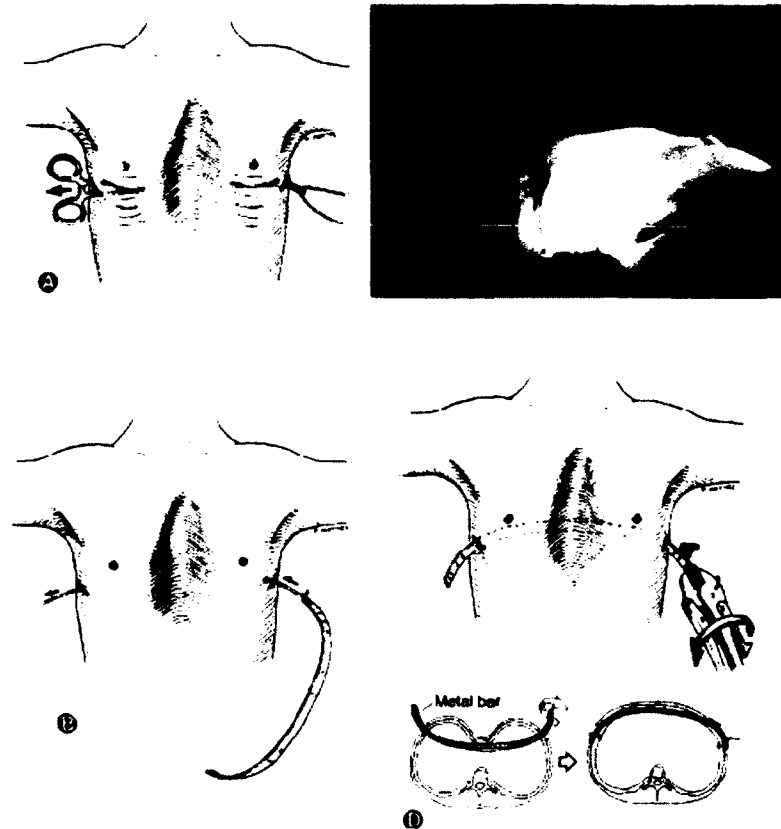
Figure 7. (A) Long curved Kelly clamp advanced across mediastinum deep to sternum. (B) Diagram shows convex steel bar being guided into the tunnel using umbilical tape to keep it on track. (C) Pectus bar positioned deep to sternum with concavity facing posterior [3]

As long term reviews of the Nuss procedure indicate, complications are caused mostly by improperly introduced bars, bar displacement or asymmetry of the deformation. Therefore, for asymmetric deformations a modified Ravitch procedure seems to be more advantageous [45, 46]. A precise classification of the defect in [27] can be useful in the accurate qualification for Nuss or modified Ravitch methods that will undoubtedly improve the results of pectus excavatum repair.

In recent years, a few modifications of the Nuss procedure have been proposed, like an asymmetric pectus bar [47] or a progressive correction of the chest deformity

using an elastic rod instead of the rigid one in order to increase the comfort of the patient [48]. In addition, as Dr. Nuss said "[...]we fully expected that people would come up with better ways and more sophisticated ways to do the job[...]" [49], there are further attempts to introduce new approaches, like an internal magnet implanted on the sternum and an external magnet in a nonobtrusive custom-fitted anterior chest wall orthosis which produces an adjustable outward force on the sternum [49]. However, this is more in the experimental stage than being close to clinical use.

CHAPTER 3

RELATED WORK

In order to establish possible paths for development of a surgical planner for the Nuss procedure, different areas have to be investigated. The most obvious is focused on surgical planners for various procedures with similar characteristics to the Nuss procedure, i.e. changing position of a bone which results in alteration of the external appearance.

Since surgical planners have to incorporate not only information about the geometry of a human part but also its biomechanical properties, methods for developing a model governing behavior of tissue and its implementation have to be investigated.

Insight into studies involving simulation of the Nuss procedure or studying the biomechanical stability of the ribcage may be beneficial in terms of developing the Nuss procedure planner.

Evaluation of results and parameterization of body parts and organs may require finding which parameters or factors, like height, width or curvature, contribute more than others. Knowing the directions in which the largest variability occurs allows focusing only on modeling what matters, thus reducing variables without losing important information.

3.1 Surgical Planners

In recent years, computer assisted surgery (CAS) systems, surgical trainers and surgical planners have been a rapidly growing area of research due to increasing computer power, development of modeling software and visualization techniques.

Focusing on systems supporting surgeon's decisions – surgical planners – we can observe a variety of solutions typically based on applications and needs. The more complex a surgical procedure is, the more sophisticated and accurate surgical planner is required. Unlike in medical simulators for teaching purposes, surgical planners utilize specific patient's data as input, which leads to completely new challenges and problems that have to be solved.

Special focus has to be placed on maxillo-craniofacial surgical planners, since, similar to the Nuss procedure, a positive aesthetic outcome is crucial to evaluate a surgery as successful. Based on a review of the literature, it is noticeable that maxillo-craniofacial surgical planners are one of the most active research areas.

Kavanagh *et al.* [50] utilized finite element analysis (FEA) in the pre-surgical planning of mandibular fractures treatment. Their goal was to reconstruct a working 3D model of a mandible that can be used in further engineering analysis and to evaluate the relevance of using commercially available software – Mimics and Abaqus, for this purpose.

This study resulted in the comparison of tensile, compressive stresses and respective displacements in healthy, fractured and mini-plated mandibles proving the obvious usefulness of numerical validation of medical procedures.

San Vincente *et al.* [51] developed a maxillofacial surgery simulator software that is capable of predicting a patient's facial appearance after surgery. The proposed approach consisted of four modules responsible for: reading and segmenting CT scans, 3D reconstruction, surgical planning using 3D models and various reference planes, and a

surgery simulator utilizing a MSM. The first three modules being already developed were out of the scope of their research presented in [51].

The approach proposed in [51] uses CT to obtain a 3D model, which is built from voxels; hence, hexahedra elements are used in their simulation. In order to populate the MSM with parameters, its linearization was proposed, based on [52], to match the stiffness matrix to the corresponding matrix in a linear elastic FEM.

Hexahedral elements need additional diagonal springs to represent Poisson's ratio. Therefore, the model includes 28 springs: 12 edge springs, 12 face diagonal springs and 4 internal diagonal springs. In the method proposed by Lloyd et al. [52], the difference between stiffness matrices of the FEM and the MSM is subject to minimization using the Frobenius norm:

$$\min\|D\|_F = \min\sqrt{\sum_{i=1}^{24}\sum_{j=1}^{24}\left|d_{ij}\right|^2}, \tag{4}$$

where $D = K^{FEM} - K^{MSM}$.

For surgical simulation purposes, San Vincente et al. [51] focused on the boundary conditions of the soft tissue in contact with the bone and studied two methods that make geometrical changes when the bone is cut and setback: scaled displacement and the removing method. Scaled displacement consists of relocating soft tissue in reference to the bone, whereas, the removing method consists of removing the tissue in contact with the removed bone and restructuring the affected elements, removing, in this case, some elements in contact with the bone. Applying both methods to the mandibular sample showed that the scaled displacement method better reflects the behavior of soft tissues. Additionally, in opposition to the removing method, the scaled displacement

method does not require re-meshing or removing of elements making it computationally more efficient.

In order to evaluate the surgical planner, the most common osteotomies: asymmetric mandibular setback, maxillary advancement and implication, and maxillary arch widening were simulated (fig. 8).
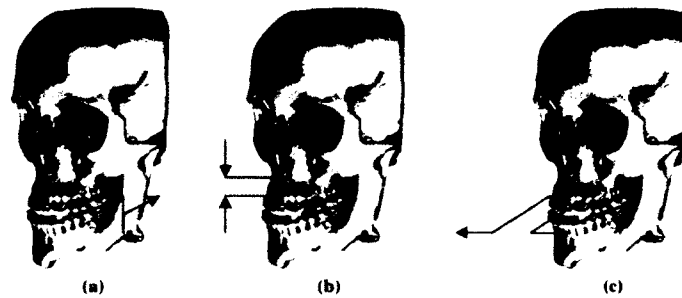
Figure 8. Surgical bone movements performed: a) mandibular setback, b) maxillary advancement and impaction, and c) maxillary arch widening [51]

Simulation of the surgery took approximately 4.5 minutes on an Intel® 2.4 GHz with 3.25 GB of RAM. Only stiffness matrix precomputation was performed, as stated before. Validation consisted of comparing outcome of the simulation with actual results of the surgery. An average error and standard deviation of five triangles for seven out of eight landmarks showed good results because it was smaller than the internal diagonal length of a cube. One of the landmarks, located in the midpoint of the vermilion border of the upper lip, was characterized by a larger error which was explained by complex curvature of the surface on that position.

The proposed solution, being a valid alternative to FEM, does not provide real time application so far. Simulation time has a chance to be improved by utilizing parallel computing and calculations performed in a GPU.

In contrast to the approach of San Vicente *et al.* [51], Obaidellah *et al.* proposed in [12] a human facial model that is able to predict the facial look after orthognathic surgery based on FEM rather than MSM.

Their method starts with generating surface models of facial skin surface and skull from CT scans. A 3D model of the facial tissue is generated using triangular mesh. The prediction of the postoperative facial appearance is done by means of movement of the lower jaw bone which directly changes the underlying facial skin surface when contact occurs between the two distinct tissue materials, which is called contact analysis of FEA. Computations in this method require tissue models utilizing quadrilateral meshes. Therefore, the quad elements are generated based on the existing triangular meshes [12].

In [12], osteotomy is simulated including mandibular bone cuts and repositioning of the sliced bone to a forward position aligned to the upper jaw. All tissues are assumed to be isotropic, homogeneous and linear elastic, while their mechanical properties were obtained from the literature.

Upon the definition of discrete elements, the system is described by:

$$-Ku = f. \tag{5}$$

After setting boundary conditions and solving the given set of equations, the authors came up with the post-operative appearance of the patient and for validation compared it with the actual postsurgical skin surface using the color map in order to represent the distance between them (fig. 9).
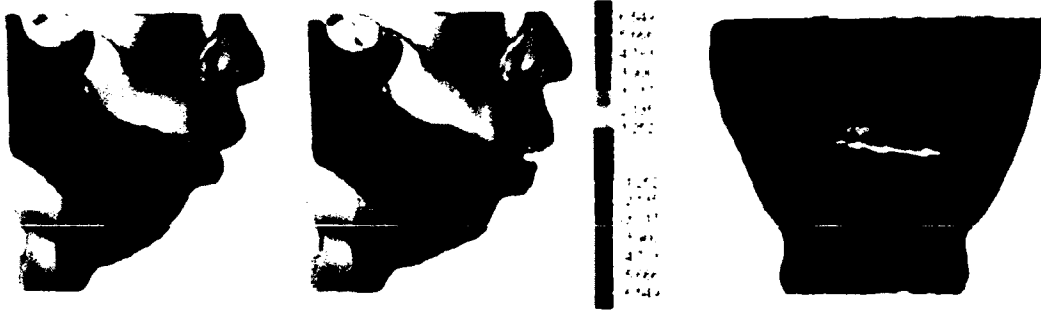
Figure 9. Simulated pre-operative appearance (a), simulated post-operative appearance (b), error measurement of the simulated result (c) [12]

Unfortunately, Obaidellah *et al.* [12] did not provide any details concerning implementation and execution time. It can be inferred that it was not a real-time simulation.

A real-time solution has been proposed by Berkley *et al.* in [13]. Typically, a contact between tissue and a tool has to occur at the nodes. Otherwise, "jumps" of the tool to the nearest node may be visible if the resolution of the FEM is not sufficient. Increasing the resolution increases the time needed for calculations. The constraints approach allows contact to happen anywhere on the model through a shape function.

The contact point divides a triangular face into three areas – A_1, A_2, A_3, whose ratios to the overall area of the face A are shape functions unique for each triangular element (fig. 10). Therefore, displacements can be interpolated by state functions incorporated into matrix C:

$$Cd = d_{\text{contact}},\tag{6}$$

where d is a vector containing displacements of each node. The same thing has to be done with the contact force in order to distribute it over the element face contact. The whole system can be described by:

$$\begin{bmatrix} K & C^T \\ C & 0 \end{bmatrix} \begin{Bmatrix} d \\ f_{contact} \end{Bmatrix} = \begin{Bmatrix} f \\ d_{contact} \end{Bmatrix}, \tag{7}$$

where f is applied force, $f_{contact}$ is a point force, and K is the stiffness matrix. Unknown are $f_{contact}$ and d, whereas f and $d_{contact}$ are known upon contact. Since lots of C^T elements are equal to zero, dense C^T, K^{-1} and f can be utilized to obtain a solution instead of using sparse matrices. According to the authors, it drastically reduces the computation needed. However, the overall performance depends significantly on a number of contact points since each of them adds three rows and nine nonzero values to C.
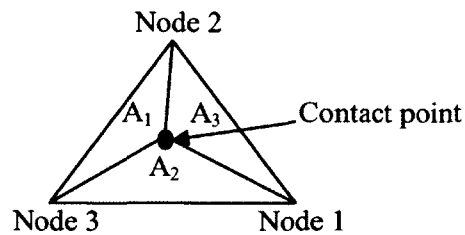
Figure 10. A tetrahedral element face divided into three triangles by the contact point
[13]

The method described above was implemented by Berkley *et al.* [13] into a suturing simulator. The FEM of a hand containing 863 nodes with a rendering frequency 30 Hz was simulated. Condensation of the stiffness matrix and taking its inverse took 4.15 minutes on Athelon 1 GHz processor. If a model is used to simulate cutting or other procedures requiring mesh alteration, this methodology is not suitable. In addition, the number of nodes present in this study was much below a typical number of nodes.

An interesting trend in a virtual object animation was started in 1990 triggered by the rapid development of computer graphics. Especially in the modeling and simulation

domain, there is a need for generating interactions between "actors" or "agents" in a real time virtual environment. It was pointed out [53] that when animating a human body, only simple behavior could be encoded into simulation in order to maintain real-time performance. This is mainly due to the highly non-linear reaction of the neuromuscular system of animals to external forces. Therefore, it has been proposed to shift from task-level animation to a connectionist approach assuming that analytic methods would not be sufficient in the future; hence, they employed a neural network to "observe" and "learn" new skills in the same way humans obtain new skills, like playing basketball or football.

A neural network supplemented rule-based simulation where a simulated character was playing handball. By learning what force and torque leads to successful realization of a particular task in a handball court, the authors were able prove that it is possible to "learn" or "train" a character to perform tasks that were not described by rules.

The idea presented in [53] was brought up in [54] where the authors raised a question of whether or not it is necessary to map exactly future state variable values of an animated system based on the current inputs or is it sufficient to approximate it only to a degree of precision needed to preserve authenticity of the resulting animation to the simulated dynamics of the physical model. The NuroAnimator, as the authors called the system, employs neural network to imitate physics-based behavior. The system learns an approximation to the dynamic inputs that causes transitions of the system. However, the training process includes only presenting isolated examples of state transitions rather than complete motion trajectories.

The authors tested the NeuroAnimator with different types of models, such as a pendulum, a lunar lander spacecraft, a truck and a dolphin. A number of state inputs, force inputs, control inputs, hidden neurons, state outputs and training samples varied depending on the model. However, it was not the authors' intention to optimize weights or the network's structure. As part of their work, they incorporated previously developed methodology for computationally efficient controller synthesis [55]. To increase effectiveness of this technique, the authors exploit the neural network approximation in the NuroAnimator to compute partial derivatives of output states with respect to control inputs. As a result, a gradient is calculated allowing the use of fast gradient based optimization for controller synthesis.

A comparison of a number of operations needed to emulate a dynamical system with the state vector N never uses more than $O(N)$ hidden units which leads to $O(N^2)$ operations. A typical single timestep using an implicit time integration scheme requires $O(N^3)$ operations. Increase in complexity is even more visible if we assume that one pass through the neural network is very often equal to 50 physical simulation steps [55].

Results obtained by this research showed that artificial neural networks can be a valuable tool to approximate the behavior of physical systems and can lead to computationally efficient yet accurate visualization of various model types.

An interesting proposed solution to a virtual object deformation problem was introduced by Cheng and Yang in [56]. The method utilizes an attributed boundary model (ABM) in which every boundary node is associated with a set of attribute matrices that take the vector of the external force as input and produces a displacement vector. The attribute matrices are the result of training an artificial neural network using the

backpropagation method (BPANN). The process of training is performed off-line and utilizes data generated by a FEM.
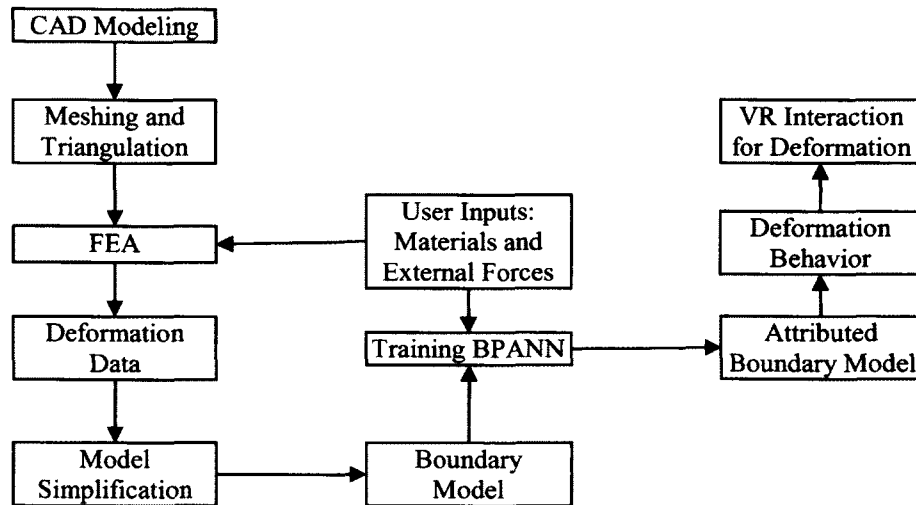
Figure 11. Workflow of the virtual object deformations using attributed boundary model
[56]

The process starts with 3D modeling of an object (fig. 11), which does not need to represent a human organ or tissue. In the FEA, material properties are set and all potential forces are obtained individually to generate deformation data which vary with the external forces.

Although only surface nodes are considered in the boundary model, FEM is performed over the whole domain to properly represent its solid nature. However, internal nodes are removed from corresponding displacement vectors.

Results from the FEA are utilized for training the BPANN where the position vector and the external acting force of every boundary node is input and the displacement vector is output. In general, output of BPANN can be obtained by employing the following relationship:

$$[T] = \left([P \mid F] \left[\frac{W}{V} \right] + [B] \right)[U] + [A], \qquad (8)$$

where T is the output matrix with position of nodes after deformation, [P|F] is the input matrix with the initial position of the nodes and acting forces, whereas [W], [V], [B], [U] and [A] are the weights and bias of the ANN and are considered to be the attributed matrices.

An important question arises when it comes to choice of ANN architecture regarding the number of neurons in the hidden layer. Cheng and Yang in [56] start with one and if the training does not converge, it is increased by one and the training is repeated until it does.

In order to visualize the results from deformation equation 8, it was encoded into a building block module of Virtools (Dassault Systèmes, France). The module reads attribute matrices of the corresponding virtual objects and scans for real time interactions to perform deformations.

The authors performed real time interactions for two generic parts, achieving a satisfying animation speed at 30 fps and errors less than 1%. It shows that employing ANNs can be a useful tool to overcome difficulties in implementing deformable objects based on their mechanical properties in real time. A very similar approach with a parametric deformation mechanism has been presented by Cheng and Han in [57], obtaining real time performance of 30 fps and more.

A real-time nonlinear FEM with an ANN has been also employed by Marooka *et al.* in [58] in order to simulate soft organ model deformation. The idea is based on the fact that a deformed model can be estimated from the superposition of basic deformation modes.

In this case, the training set consists of an external force and its corresponding deformation mode, which is the model deformation caused by force. More accurately, there are seven input neurons: three for the position of a contact point, three for the directional unit vector and one remaining for the magnitude of a force. The number of neurons in the output layer is equal to the number of a model vertices times three. However, reducing the dimension of the output has been performed by applying PCA which should result in an improvement in computation time.

Similarly to [56] and [57], given the force direction and its magnitude, an ANN outputs the vector containing the shape of the object with reduced dimensionality, which can be back-projected into the original model space.

The authors implemented their approach on an Intel® 2.8 GHz with 1 GB of RAM with the volume model of a liver. The model consisted of 729 vertices and 512 cubic elements, and the time needed to obtain the final model was 0.28 ms after the input data was given. This result shows that it is possible to emulate the real time deformation using an ANN.

As can be seen, real time simulation with utilization of FEMs can be achieved only for small objects with a limited number of nodes. However, interpolation of results by ANNs seems to be a reasonable trade-off between accuracy and speed which should be pursued in this work.

3.2 Simulation of the Nuss Procedure

Advances in development of surgical planners in different areas did not translate to a simulation of PE treatment. To date, neither a surgical trainer nor a surgical planner of the Nuss procedure has been introduced. However, there have been studies that

simulate the procedure in order to study behavior, biomechanical stability, and stress distribution of the ribcage [11, 59-62].

Nagasao *et al.* in [11] tried to confirm the existence of a difference between children and adults who underwent the Nuss procedure with regards to stress distributions which may lead to pain.

Firstly, the authors used CT scans collected from 18 subjects with PE, divided into two groups of 10 children and 8 adults, to extract information about the geometry of each thorax. However, typically segmented thoraces did not include enough information for direct use in analysis. On that basis, Computer Assisted Design (CAD) models were produced where the 12 vertebrae, sternum, 12 ribs and 12 costal cartilages were modeled as beam elements with their number adjusted to morphologic complexity.

Simulation of the Nuss procedure was performed using the FEA software ANSYS 10 with an assumption that the Lorentz bar was located at the fourth intercostal space. Using the same method, the authors simulated corrected shapes of the thoraces.

Performance of a structural FEA requires specifying the mechanical properties of the studied object. For PE, little research has been done in order to assess the material properties of the intercostal cartilage. Therefore, there have been different approaches used in a number of studies requiring specification of mechanical properties of the PE cartilage, which includes mainly literature reviews [59-61]. In this study, the authors decided to assess the mechanical properties of the thorax using the linear model developed by Kopperdahl *et al.* [63] which relates Young's modulus to the quantitative CT in the vertebra in the form of a linear equation obtained by linear regression.

Comparison was performed by localization of 6 landmarks on respective thoraces. Calculation of correlation coefficients for each thorax resulted in values almost equal to 1, which, according to the authors, proved validity of the simulation.

Results of the FEA showed that the intensity of stresses on all 12 ribs was greater among adults than children and that in the adult group, stresses of similar magnitude as on the bar supported ribs were present on few a consecutive ribs (fig. 12).
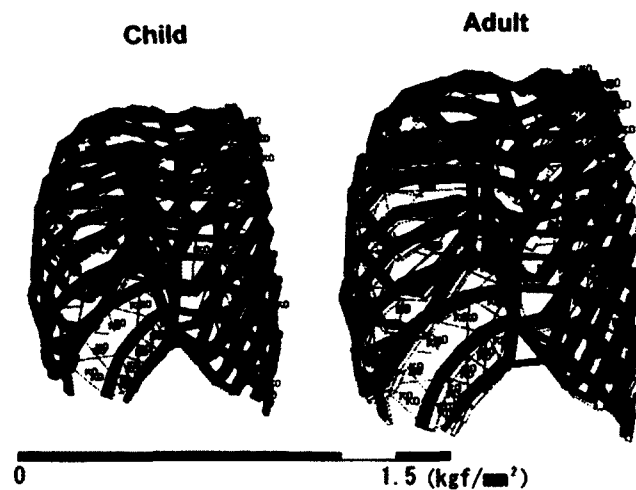
Figure 12. Examples of stress distribution patterns for the child and adult groups [11]

Chang *et al.* [59] performed a similar study on three patients approximately 7 years of age, observing stress and strain patterns in FE models. The simulation results showed that the greatest strain occurred at the third through seventh cartilages, especially where they join the sternum and ribs. A high bilateral stress distribution was also found over the backs of the third to the seventh ribs near the vertebral column. Those findings showed a wider stress area when compared to those obtained in [11]. However, in [59], the Young's modulus of the ribs and sternum was assumed to be as in [60] and [61] – 11500 MPa, whereas the elasticity modulus of the costal cartilage was 12.25 MPa, as suggested by Feng *et al.* [64].

Wei *et al.*[62] simulated the Nuss procedure to identify the most optimal location for the titanium pectus bar and questioned the general practice of placing the bar at the end of the depressed sternum. To verify their statements, the authors created a FEM based on 227 CT images of a boy's ribcage. Mimics 10.1 was utilized to segment the ribcage and spine, whereas Abaqus 6.5 served as a preprocessor and solver. The model of the bone was assumed to be isotropic for simplification like in many other studies. However, every part of the bone had a different specific parameter based on bone density or CT gray value. Ribs, sternum, the dorsal vertebrae were modeled as isotropic linear elastic materials whereas costal cartilage was modeled as isotropic viscoelastic materials. Bone material was subdivided into four types from cortical bone to marrow. Costal cartilage was divided into two materials. Despite increased accuracy of the model, this approach cannot be implemented in an automated system as part of a simulator. However, the utilized parameter values can be hard coded within a model used for simulation.

The majority of studies point to several problems when simulating the Nuss procedure. The first is from generating a patient specific model of a ribcage including costal cartilage. Extracting the complete ribcage is difficult since cartilage has similar grayscale values to the background, causing the presence of artifacts.

Wang *et al.* [65] were able to extract information about the PE cartilage from 227 slices belonging to a boy, probably the same that was used as a subject in [62]; thus, the ribcage used in that study did not suffer from the previously described issue.

The authors applied a linear grayscale conversion to enhance contrast and improve visualization of CT slices which led to better diversified bone and internal

organs. In Mimics 10.1, two thresholds were applied to separate rigid skeleton from costal cartilage. However, the threshold of the costal cartilage was still close to that of internal organs so various algorithms were utilized, such as regional growth, mask edition, and smoothing. Although the rigid skeleton was much easier to separate from internal organs, it required noise filtering using the same algorithms that were used for the costal cartilage. Finally, the authors obtained the whole model of the PE ribcage (fig. 13).

Despite being successful, this technique is fully manual and each FEA model needs to be generated individually in order to ensure its correctness. Therefore, employing synthetic models of the ribcage taking into account characteristics of patients' deformation obtained from CT slices or partially segmented models seems to be the best direction to pursue.

Another difficulty is a definition of the mechanical properties of the PE ribcage with costal cartilages. Ideally, properties obtained *in-vivo* should be used. However, since they are not available yet, the most suitable approach is employment of the atlas based values multiplied by a certain factor in order to mimic the properties of the PE ribcage.
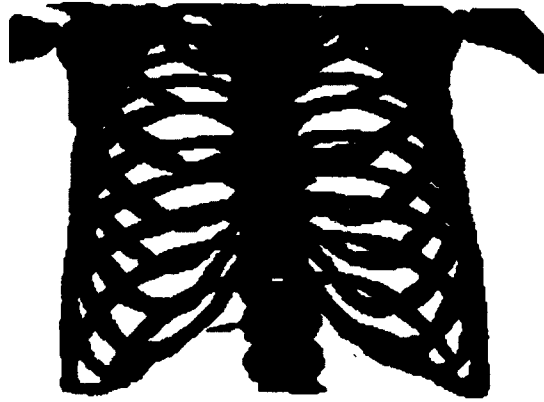
Figure 13. Ribcage with segmented cartilage [65]

3.3 Shape Analysis of the Human Body

Very important information regarding an organ being investigated can come from studying variability of shape. Various publications propose statistical analysis over a large sample of object instances in order to extract an average shape chest and directions in which the largest variability occurs.

The development of three-dimensional scanning made collecting data concerning shapes belonging to the human body, faster, easier and more accurate. This type of scanning allows building vast 3D shape databases and analyzing them. Nevertheless, acquiring data is just the beginning. There are a number of issues that have to be addressed to perform valid shape analysis. These can be identified by reviewing the approach and determining what obstacles can make it problematic.

The first and foremost research is presented in [66]. The major premise in this paper is that there are problems in modeling naturally looking faces, which are generally caused by difficulties in localization of corresponding features and separation of realistic faces from those that are unlikely to appear in reality.

They proposed building a morphable face model which is nothing more than a linear combination of a large number (100 male and 100 female) of 3D face scans. This requires statistical exploration of the whole dataset and establishing the main modes of shape variations, which is performed by applying PCA to a shape vector containing coordinates of all the vertices belonging to each 3D model. The distribution of face attributes serves as a constraint to avoid creating unrealistic faces by manipulating linear coefficients in the morphable model.

Once the morphable or average model has been developed, the 3D shape and texture of a new face can be reconstructed from a single image provided. However, as an initialization step, rough manual adjustment of coefficients is needed. In this case, the model tries to find a set of shape coefficients that allows matching a new image in a natural way.

Uniquely, in [66] registration between 3D models is taken for granted and is not described in detail. Because their method utilizes photographs as a source of texture and 3D face scans as a source of shapes, they used a modified gradient-based optic flow algorithm to find correspondence between a pair of 3D scans, which were represented in terms of two-dimensional cylindrical parameters. The original optical flow algorithm quantifies the frame-to-frame differences in image sequences. In [66] the algorithm takes into account color and radius simultaneously and tries to find such flow that the difference in both terms is minimized.

Strongly motivated by [66], in [67] 250 full body 3D scans representing different body types are used for better understanding and characterization of range of the human body shape variation. However, their main purpose was to find a way to bring those scans

into correspondence and then to determine the main components responsible for variations in body shape. The source of the data is the CEASAR (Civilian American and European Surface Anthropometry Resource) project during which thousands of full body scans were collected.

Firstly, the authors [67] matched an idealized and holes-free model generated by an artist to one of the male scans using a set of manually selected markers. This resulted in a template mesh, which was used to register the remaining the male scans. To obtain a set of female scans, the male template mesh was used to find the respective female template mesh.

The described approach has two advantages. It allows using data from the template mesh to fill holes in the CEASAR scans and by finding correspondence between scans, it was possible to parameterize all scans and perform PCA to identify the components with the highest variance. Utilization of variance values allows creating individuals that, although they did not exist previously in the dataset, are likely to be realistic.

In [67], PCA provided means to explore the space of possible bodies given partial and markerless data. Instead of finding a smooth set of transformations applied to each vertex, a set of principle component weights that match the data can be searched. A similar approach, called bootstrapping, was used in [66]. If a model that is not part of the training set and substantially differs from the template mesh is presented for matching using transformations, such matching will fail. However, by looking into the PCA space, the correspondence may be found.

Using the same method, it is possible to perform the opposite matching. If only the sparse data is present, in this case only 74 markers, the approximate shape of the subject could be estimated. This approach may be used if the data is collected without using expensive equipment, like 3D scanners.

A lesson learnt from this particular research is that small variations in pose may influence PCA. By identifying and excluding those components, PCA may give better answers concerning the analyzed shapes.

Utilization of CEASAR data can be also found in [68]. The authors were also interested in extracting the main PCA modes, but in contrast to [67], a markerless approach is used.

As in [67], before PCA could be applied, methods for filling holes, scan alignment and segmentation had to be developed. Each 3D scan is sliced using horizontal planes, which results in a set of profiles. If all profiles on an individual slice are closed, it means that there are no holes. However, if holes are present, at least one profile is open. Such identification aides in closing those profiles and, after rebuilding each body, voxelization is performed to obtain volumetric representation. However, because hands are represented by very corrupted data in the CEASAR database, in [68], they are removed from the models.

In [68], in order to perform PCA, a shape vector is created where each element of that vector is the signed distance from a voxel to the surface. PCA was applied to 300 volumetric models of male subjects, and it was found that the first 64 eigenvectors represent 95% of the total variance.

The experiments are divided into three groups where PCA is applied to the original models, normalized models and models without arms. Normalized models do not take into account information about height which effectively separates information about the shape from that variable. Arms were removed because of significant misalignment among models, which introduces artificial variability that has no contribution to the body shape.

When the height is filtered out the main mode becomes weight – over 1/3 of the global variability. The rest of the main modes are: posture, mass distribution and muscularity, spacing between the torso and the arms, and head position. Removing arms changed the values of contribution to the global variability in favor of the weight from almost 34% to over 36%.

In [68], all models were normalized to the same height before applying PCA in order to isolate the shape variation from the height differences and improve the correspondences between the models because if the models are at the same height, their anatomical features tend to align better with each other.

In [10], the focus of the research is a female breast modeler. In the preprocessing phase, as in [67] and [69], a generic template mesh of the breast is fitted to each scan surface making the finding of corresponding features among scans easier. To deal with sagged breasts, two scans were taken – when the breast is sagged and when it is lifted, and then both results are merged according to an earlier developed procedure.

The template mesh is deformed to match identifiable markers on the 3D scan (fig. 14). Because it contains only a few triangles, they are subdivided into smaller ones to

allow for finer matching and obtaining more realistic results. Since only one breast is modeled, it is mirrored to acquire a symmetric mesh.
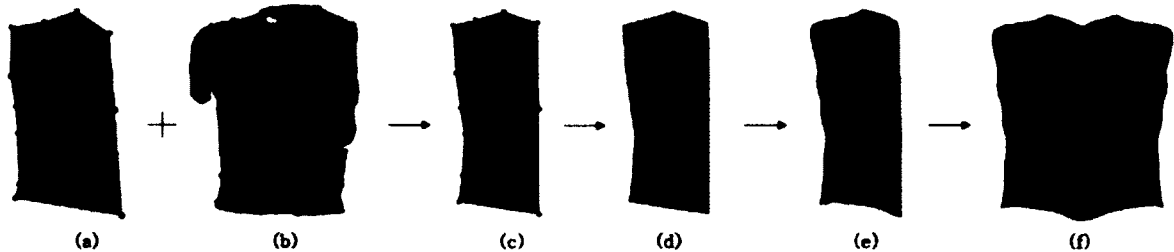
Figure 14. Deformation a template mesh: (a) Template mesh prior to pre-processing, (b) target scanned mesh, (c) deformation of the lower level template mesh by relocating feature points, (d) higher level mesh is obtained by subdividing each patch in the mesh, (e) deformation of the higher level mesh and (f) mirroring to acquire a symmetric mesh [10]

Once data is parameterized, it is possible to perform PCA on a set of 28 shape vectors corresponding to each subject. Due to strict preprocessing, it is assumed that each mesh has the same number of vertices and triangles.

Results show that all modes have been "contaminated" by a common factor – the underbust girth combined with the sagginess, which are represented by the first mode as well.

Obtaining the average model allows building a breast modeler in the same fashion as it was done for faces in [66]. In addition, new data can be introduced to the modeler as long as markers are present and they fit the template mesh. Then by changing attributes identified by PCA, new data can be matched and characteristics can be obtained.

Kim *et al.* [70] questioned the common practice of using 3D scans to build a body modeler stating that a 3D scanner is too expensive for use in a general clinic. Therefore,

they suggested using the patient's photographs to deform a template model via identifiable markers in their 3D virtual simulator for breast plastic surgery. For the deformation they applied procrustes analysis and RBF.

Two side-view and one front-view photographs and 28 markers are needed in the author's torso modeler. Some of the markers have to be placed manually and some of them are detected automatically based on contrast between the skin and the background. Global deformation utilizes the procrustes analysis which is an initial step for local deformations executed with RBF. The simulator was trained with eight cases, including both before and after surgery photographs. According to the authors, it takes from one to two minutes from the time the photographs were taken to simulate the expected outcome of the surgery.

Improvement of the method for parameterization of the input data presented in [67] is introduced in [71]. Again, a generic model is used for aligning each scan, which comes from the CEASAR database. A two-step procedure is proposed utilizing an RBF network for rough deformation and then performing error minimizing for fine alignment.

The RBF network is built on landmarks. Therefore, it is reasonable to use it because both the generic and CEASAR models contain the same number of markers. After an RBF transformation, the generic model is deformed to be closer to the target model in shape, pose and height (fig. 15). Because RBF ensures a good registration of landmarks, in the second step, the fine mapping, marker information can be discarded and only data and smoothness errors are taken into account.

In contrast to [67], in [71] the fine alignment is focused on the difference between the source surface and target surface, referred to as the data error, and the difference between transformations on neighboring vertices – the smoothness error.

In [71], to achieve similar accuracy as in [67], only half the time is needed, and the steady-state final error can be obtained after 200 iterations instead of 800. This was made possible by using the RBF network for the rough alignment.
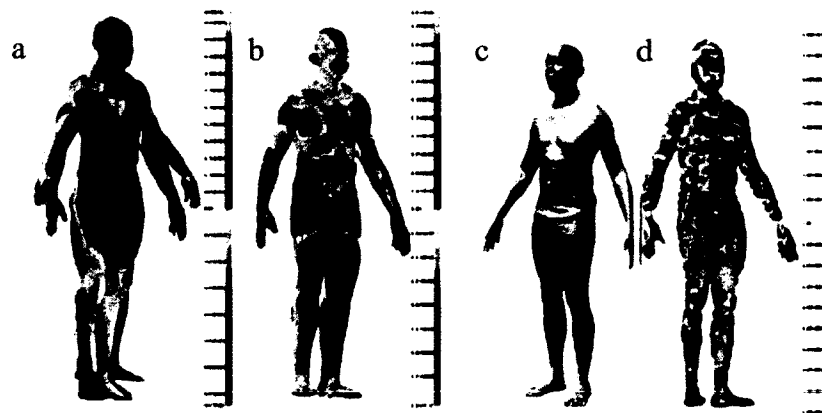
Figure 15. The generic model with the target surface – a), RBF-deformed generic model and the target – b), input model for the fine mapping – c), comparison between fine mapping result and the target – d). Colormaps represent magnitude and sign of the mapping error [71]

As soon as the alignment was finished, PCA was performed on a shape vector containing all vertices representing the whole dataset. Results are similar to the ones obtained in [68] for non-standardized models. Therefore, in [71], segmented PCA is performed on the same set of models, where the whole body has been divided into six parts: head, left and right arm, torso, left and right leg.

Focusing on the human torso, it was shown that the first mode is height, the second lies in weight and the third in a volume-preserving ratio. The next few modes are related to pose and shape. However, it is possible that after normalizing, when the height is filtered out, the main modes could be different and more representative.

On the basis of this literature review, a number of observations can be made. First of all, 3D scanning positively influences the development of the shape analysis, because it enables acquiring a lot of data and digitalizes them instantly. In the presented papers, two sources of data are used: one dataset collected specially for a certain study [10, 66] and a common database [67, 68, 71]. To facilitate collecting data by researchers, marker placement, scanning technique and scanning area may be adjusted to make future analysis easier. Usually, 3D scanning includes fewer subjects, but each data collection can be made more carefully.

The 2D analysis approach provides more subjects, but such data usually needs a lot of preprocessing, like hole filling, smoothing, extraction of interesting body parts, etc.

Another observation is related to model alignment by bringing all models into correspondence. The most obvious approach is placing markers. In addition, the same vertex across all models should represent the same feature on the body, and a shape vector has to contain the same amount of information from each model. Having markers, a template mesh or model can be created and utilized for registration [10,67,71]. However, the most suitable method should be chosen on the basis of data characteristics. All presented approaches do not address what to do in cases that are markerless, not water tight, and are without any distinctive physiological features that can be used for registration models.

Concerning PCA, in all studies it was done straightforwardly. A shape vector was typically filled with coordinates of vertices [10,66,67,71] or any other representative descriptor common for all models [68].

As far as a model of the human torso is concerned, it was obtained by [67, 68] and in the most optimal way by [71] utilizing the CEASAR database. The approach presented in [10] may not be sufficient for a male chest because the template mesh would need more markers and, initially, more triangles to be adjusted to many nondescript uniform surfaces.

CHAPTER 4

METHODOLOGY

Although this procedure is routinely performed, the outcome depends mostly on the correct placement of the bar. It would be beneficial if a surgeon had a chance to practice and review possible strategies for placement of the corrective bar and the associated appearance of the chest. A strategy for the development of a Nuss procedure surgical trainer and planner, taking into account the biomechanical properties of the PE ribcage, emerging trends in surgical planners, deformable models, and visualization techniques was previously proposed [72]. In this chapter, methods to achieve goals related to the development of this system are presented, including the development of a generic model with capabilities to be deformed according to patient specific data, the design of a black box approach to approximate the force-deflection model of the PE ribcage for planning and training of the Nuss procedure. Additionally presented is a comparison of before and after surgery surface scans as a means to validate results, comparison of an average chest shape with post-operative results to quantify the outcome of the surgery, and the hardware setup of the simulator.

4.1 Nuss Procedure Core System Design

The proposed Nuss procedure surgical planner [72] is based on a finite element model (FEM) of the PE ribcage (fig. 16). However, since FE modeling is not conducive to real-time performance, it cannot be directly implemented into the system [12, 51]. Therefore, approximation of the FEM using a black box approach was proposed.
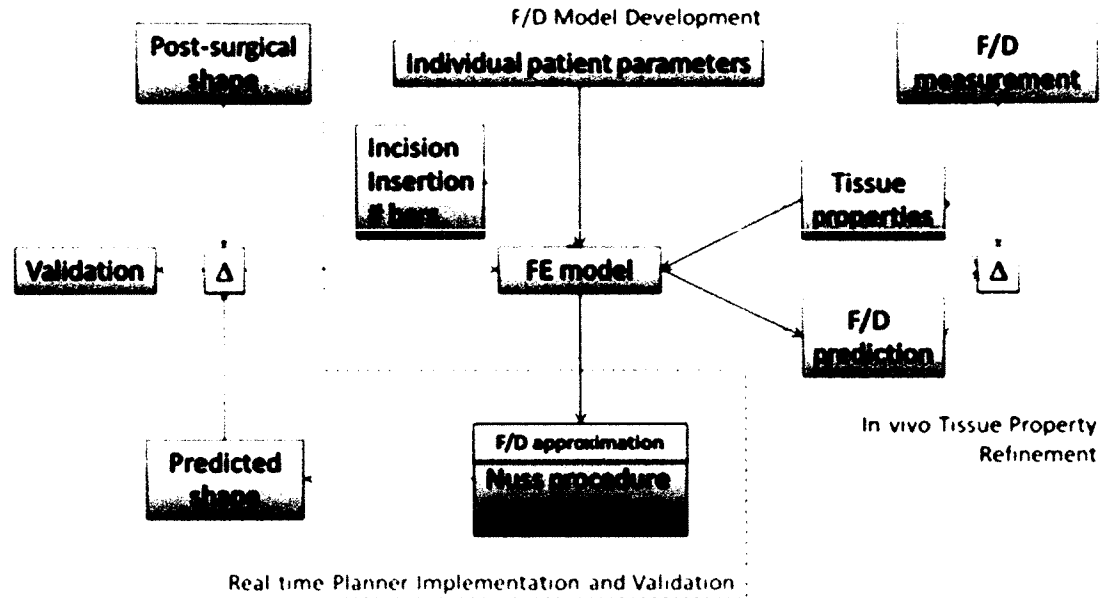
Figure 16. Development process of the Nuss procedure planner

The individual parameters collected from the CT data belonging to actual patients with PE are used to create a set of patient specific FEMs as shown in the upper middle section of Figure 16. Force-deflection data is used to create the approximation model avoiding usage of FEA engines. Figure 16 also shows a comparison between the predicted shape, and the actual post-surgical shape will serve as a means for validation.

The right side of Figure 16 shows refinement of the tissue properties since there is no agreement as far as the mechanical properties of cartilage are concerned. Based on those findings the FEM of the ribcage may be updated.

4.1.1 Development of a Generic Ribcage Model

As stated before, PE ribcages are difficult to segment because of missing elements corresponding to the cartilage. Therefore, attention was focused on a parametric model of

the ribcage that can be deformed based upon individual patient parameters obtained from CT slices to fit the PE ribcage.

To start the process of development of a generic ribcage model, 62 CT data sets documenting PE cases prior to surgery were collected [EVMS IRB# 11-10-WC-0236, ODU IRB# 12-02]. Since there are multiple types of PE deformations, only CT data belonging to patients with the broad symmetric "saucer" type of PE was used. This type is less common than the more localized "cup" type [73].

A geometric model of the ribcage was created in SolidWorks (Dassault Systèmes SolidWorks Corp., Vélizy, France) based on a human anatomy atlas. First, the sternum was created as the base and, subsequentially, the cartilage and ribs were extruded along curves as rectangular profiles. Keeping in mind the eventual conversion of the geometric model to the finite element model, all unnecessary features were omitted. This resulted in the simplified yet anatomically correct model (fig. 17). Sections of the ribs continuing to the spine were presented even though they are not crucial for the model since they may be useful for a future application.
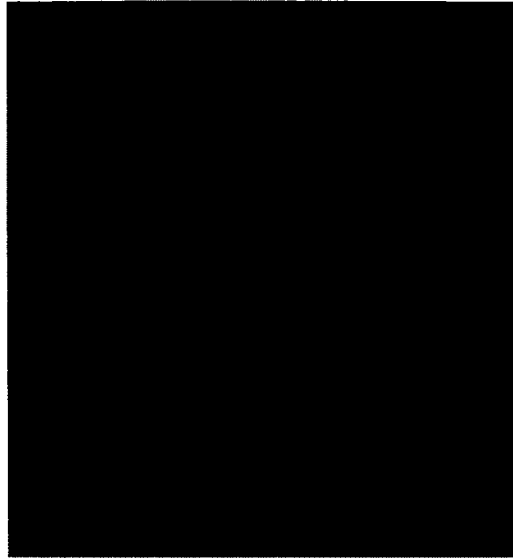
Figure 17. Generic geometrical atlas-based model of the ribcage

Once the model was created, it was converted to IGES format and exported to a FEA preprocessor – HyperMesh (Altair Engineering, Troy, MI, USA). In this preliminary step, the model was converted to a triangular mesh using the preprocessor's FE meshing algorithm. This process ensured consistency among vertices at different stages of the deformable model development. In this way, all 20708 triangular facets of the mesh (fig. 18) were concurrently two dimensional triangular finite elements which allowed the exportation of this surface FE model in STL format to Autodesk 3ds Max for further processing.
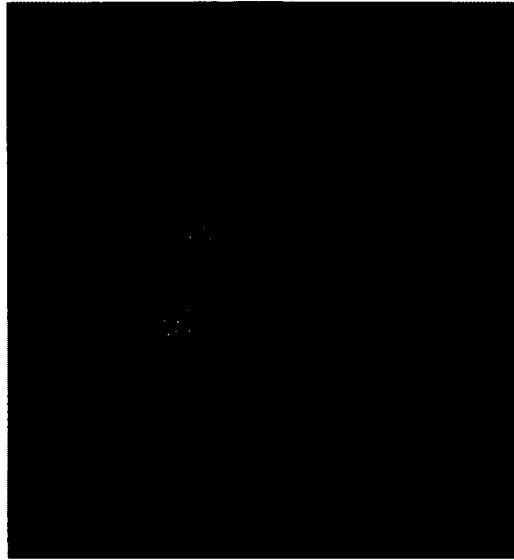
Figure 18. Generic ribcage model after meshing with 2D triangular elements in
HyperMesh

Once the model was imported into Autodesk 3ds Max, an underlying system of

bones was constructed. A bones system is a jointed set of objects called bones which is

typically used to animate various objects, especially those described by a continuous

mesh. Animation of bones is typically performed using forward and inverse kinematics.

Initially, every part of the model had an underlying bone (fig. 19). However, such

a system was too complex to be controlled and deformed. Additionally, CT data did not

provide adequate enough information to execute that model. It was observed that the

location of the sternum depends on the deformation of the cartilage which meant that

repositioning the sternum would recreate the deformity. Therefore, the bones system was

reduced to two bones incorporated in the sternum (fig. 20).
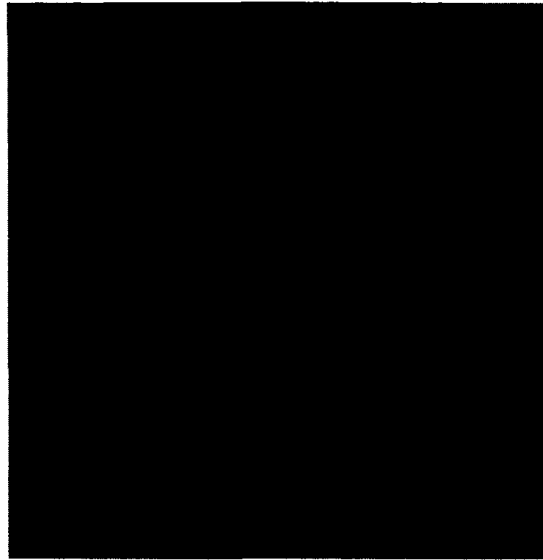
Figure 19. The initial "full" bone system

Before the model can be deformed using bones, envelopes, associated with each bone, have to be defined. The envelope is the tool for controlling deformation of the surface of a model, called in this process *skin*. An envelope defines an area of influence of a single bone. Vertices bounded by the envelopes are assigned weights to generate smooth transitions at joints. This process is very tedious but vitally important as it is responsible for the generation of realistic deformations.

Before the envelopes in the ribcage model are adjusted, characteristics of the PE deformation have to be investigated. According to Dr. Robert Kelly, a surgeon from CHKD and expert in the Nuss procedure, the first two costal cartilages are not deformed, and the lower part of the sternum is sunk the most. However, there can be, and very often is, some torsion of the sternum. Those two elements impact the child-parent relationship between the bones and how the envelopes influence vertices in the model.
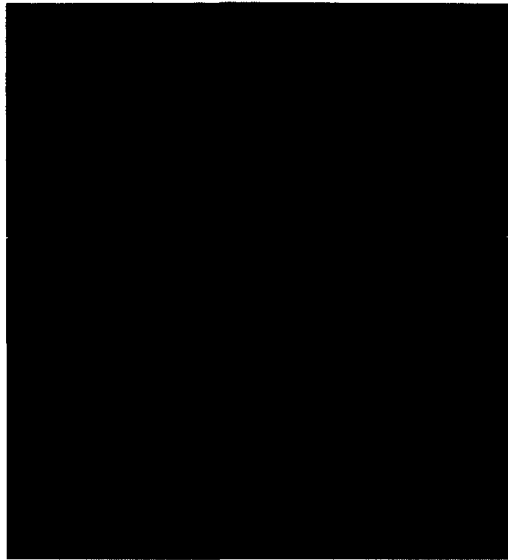
Figure 20. The final bone system with three bones

In the ribcage model, only the upper bone has envelopes influencing vertices. The last bone is needed as the end-effector in the kinematic chain. The first bone influences the sternum between the second and the third costal cartilage with weights from 0.3 to 1, and the remaining part of the sternum is affected with weights equal to 1.

As can be seen in figure 21, vertices within an outer envelope do not receive 100% weighting. A vertex can either fall inside two or more outer envelopes whose gradients sum up to 100% or greater, or the vertex must fall within an inner envelope to have 100% weight. Any vertex within an inner envelope receives 100% weighting. Weights fall off sigmoidally in the area between the inner and outer envelope boundaries. This property is very useful to visualize the deformation of the cartilage.
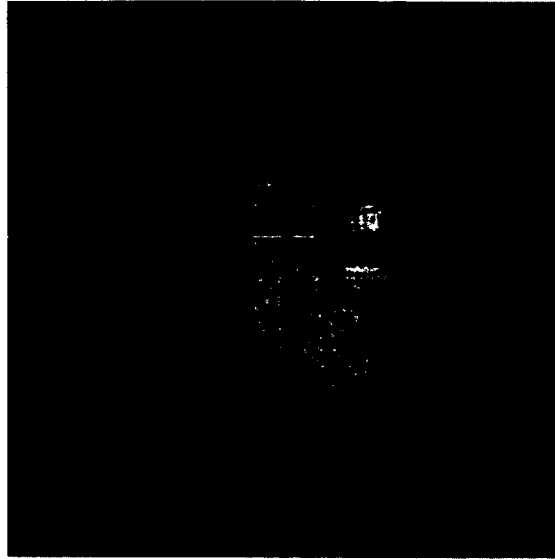
Figure 21. Envelope and weights distribution

While the bones are responsible for patient specific deformation, the shape of the ribcage is controlled by non-uniform scaling in the x, y and z-axes. Width and depth of the ribcage is measured on a CT slice approximately at the point of the highest depression, i.e. where the sternum reaches the highest distance from the normal position (fig. 22). From the same slice where the width and depth are measured, sternum displacement and torsion is obtained as shown in figure 23. Height of the ribcage is based on the length of the sternum. This is calculated by registering the CT slices where the beginning and the end of the sternum can be observed. Knowing the distance between slices, the overall length of the sternum can be then calculated.
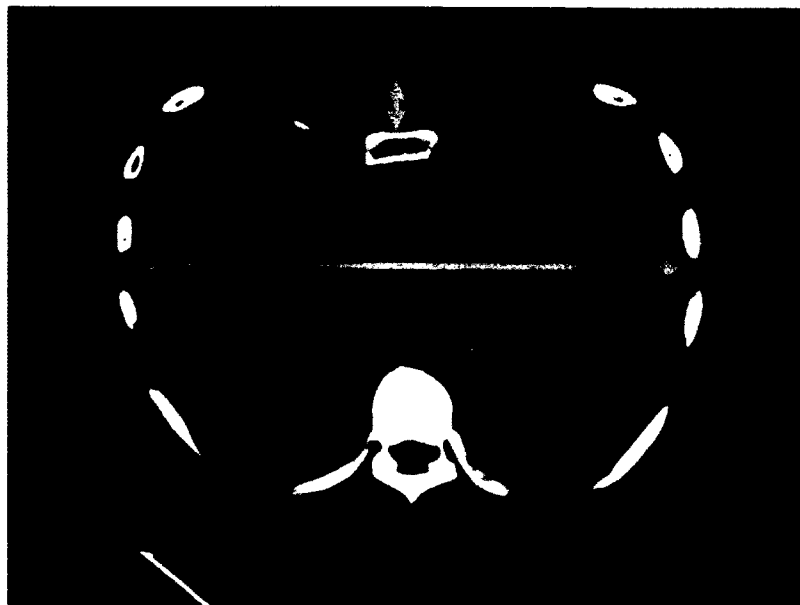
Figure 22. Scheme for measurements of width (yellow arrow), depth (blue arrow) of the ribcage and depth of the depression (grey arrow)

To make working with the model easier, a ribcage modeler was developed in MAXScript. MAXScript is the built-in scripting language of Autodesk 3ds Max. Among other capabilities, it provides users the capability to script most aspects of the program's use, such as modeling, animation, materials, rendering, and so on. This allows also the building of custom user interfaces.

Figure 23. Scheme for measurements of sternal torsion

First, a user has to provide the magnification of the CT images in order to recalculate the width and depth of the ribcage for further scaling. Magnification always has to be specified, even if it is equal to one. Otherwise, the remaining parameters remain inactive. This feature enforces the special attention of a user needed in taking measurements from the CT data. In the next step, ribcage width, height and depth are specified. The last two parameters are associated with the bones. The first is responsible for sternum depression and the second for its rotation. Parameters associated with the bones have respective limits. The sternum can be lowered up to 60 mm and rotated around its axis by 45 degrees in both directions.
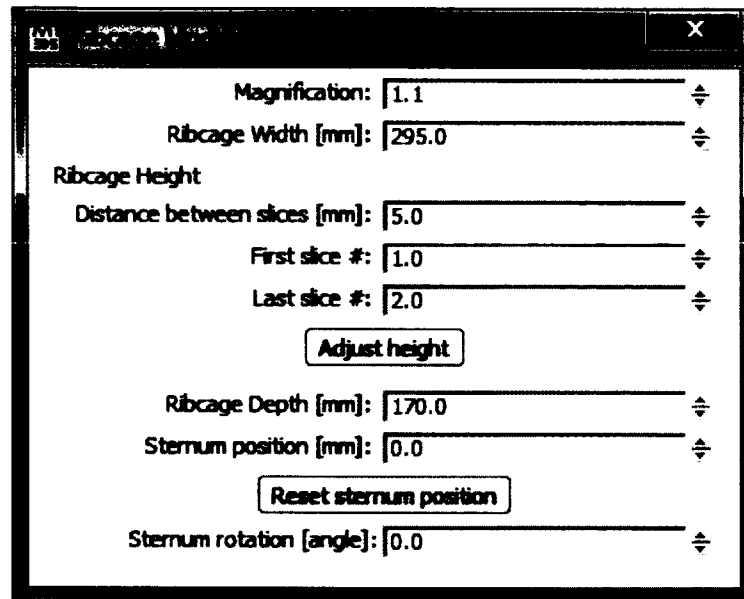
Figure 24. Ribcage modeler

Once the parameters are read, they can be applied in a convenient way through the ribcage modeler to the generic ribcage modeler (fig. 24). Although it is possible to apply sternal torsion to the model, the FEM patient specific models do not have this parameter taken into account. We can assume that sternal torsion is reduced after using the introducer and can be solved by only visually bringing the sternum to no or minimal torsion.

An example of the patient specific model is shown in figure 25. Ribcage width, sternal length, depth and depth of the deformity were 232, 175, 126 and 14 mm, respectively. All remaining 61 models were created in the same manner. All patient specific parameters are shown in table 2 in Appendix A.

Figure 25. Patient specific model of the ribcage with PE deformation

4.1.2 Finite Element Model of the Patient Specific Ribcage

The FEM used for training of the ANN was derived from the shell model of the generic ribcage described in section 4.1.1 where the geometrical model of the ribcage was initially meshed using 2D triangular elements creating a regular mesh (fig. 18). This step was meant to ensure that the number of vertices in the mesh of the geometric model in 3ds Max and FEM in HyperMesh was preserved. STL format was used to export the model to HyperMesh since it treats models saved in this format as shell FEMs. In the next step, based on 2D elements, a tetramesh was created. Pointedly, the surface mesh remained unchanged and consisted of 10348 nodes and 20708 triangular 2D elements. For training purposes, this number can be decreased by removing nodes belonging to the ribs since they do not displace significantly and they can be recreated statically in the VR environment. In this way, the number of nodes was reduced by 65%.

There are three components in the FEM of the ribcage that had to be distinguished: the ribs, cartilage and sternum. Therefore, the FEM was split into three parts based on material properties.

The mechanical properties of the components of the FEM of the ribcage are listed in table 1. There is a consensus in the field as far as the properties of the sternum and ribs are concerned. However, the mechanical properties of cartilage vary, depending on the source, and finding them *in vivo* is still one of the most important goals of biomechanical studies related to PE. Note that FE analysis requires the mechanical properties of the tissue being modeled. Since there is no agreement concerning the material properties related to PE cartilage, the most reasonable alternative is to use values suggested in [59, 60, 62, 64].
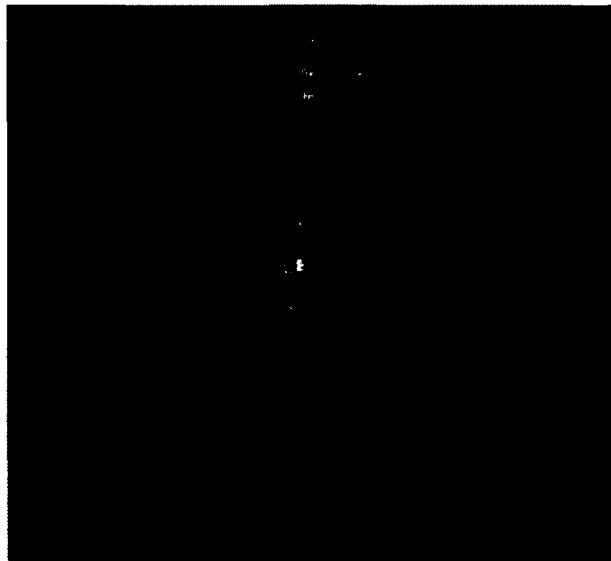
Figure 26. Generic FEM of the non-PE ribcage.

The mechanical properties of cartilage are an important aspect to get right. However, the characteristics of the Nuss procedure cause other factors to play an important role.

After the introducer is used to make a pathway for the pectus bar, the sternum is initially lifted, and the structure of the cartilage is intentionally compromised to allow easier deformations when the bar is introduced. This step causes, with high probability, material properties of the cartilage to play a lesser role.

Another important factor influencing material properties of the cartilage is the age of a patient. As a person ages, the cartilage becomes stiffer. It is one of the reasons why the Nuss procedure should be performed while the patient is a child or a teenager. It is very common to place two or sometimes even three bars when the Nuss procedure is performed on an adult. Therefore, the material properties of the cartilage are strongly patient dependent.

Table 1. Mechanical properties of the components of the ribcage

	Elastic Modulus (MPa)	Poisson ratio
Sternum	11500	0.3
Ribs	5000	0.3
Costal cartilage	20	0.4

For the purpose of this study, cartilage is assumed to be isotropic elastic with $E = 20$ MPa and $v = 0.4$. However, forces fed back to the haptic device can be scaled in the VR environment taking into account the changing stiffness of the cartilage.

The next step in preparing the template for creating realistic corrections to be used as training data for the ANN is the definition of the boundary conditions and forces. The boundary conditions – constrained movements in all axes and all three rotations – were applied at the end of all ribs. There are three variants for the location of the force. Each force takes the following values: 50, 70, 100, 200, 400, 800, 1500 and 2000 N. This results in 24 load cases and 1488 training vectors taking into account 62 subjects.

Figure 27. Location of the forces

Once the FEM of the ribcage was created, it served as a template to create the FEM for a patient specific model of the ribcage. Since the native HyperMesh file format is in binary, an ASCII Nastran input file was used to edit the data.
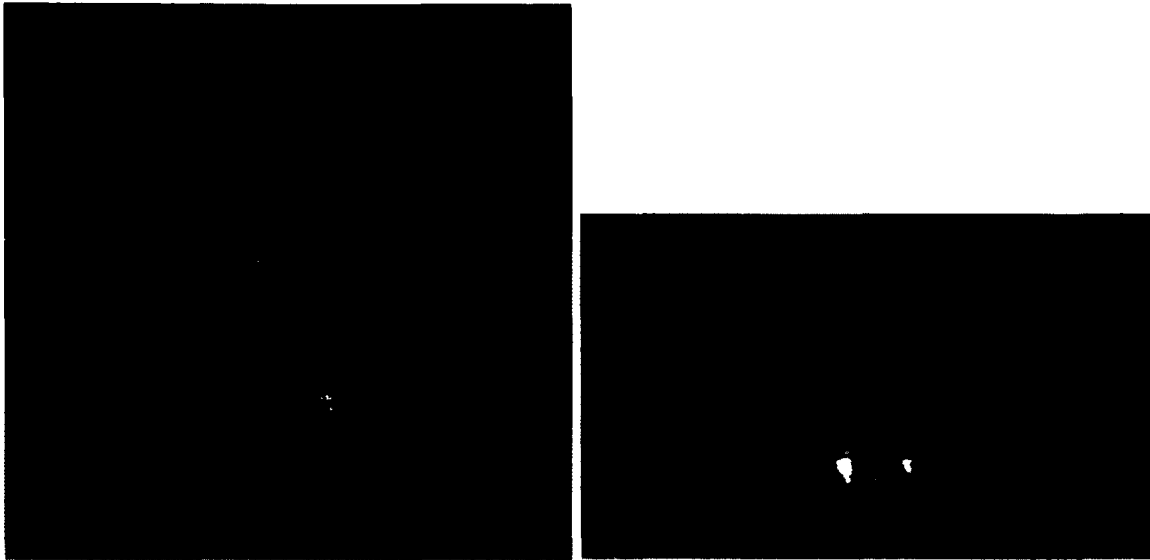
Figure 28. Patient specific FEM

Every patient specific model was imported in STL format to HyperMesh, and then exported to a Nastran input file format. The Nastran input file structure contains information about the coordinate of each node (vertex) in the model and how those nodes define elements. By substituting the position of the nodes in the template file, a new FEM was obtained and then solved using Radioss (Altair Engineering, Troy, MI, USA) – a finite element solver. FEA resulted in 1488 output files containing displacements of all nodes for each load case.

4.1.3 Creating a Model Relating Force and Displacement

Since the real-time application of FEMs is very demanding computationally, this research proposes to create a mathematical model which would memorize the displacement data from the FEM simulation. The generalization ability of an artificial neural network can be beneficial in this case. However, using them is not so straightforward, and a relatively good understanding of the underlying theory is essential.

Despite focusing on solids in the FEM simulation stage, for visualization purposes, it is only necessary to extract the surface nodes. The rest is not visible; thus, it is irrelevant.

A crucial problem when using ANNs is the appropriate preparation of training data. The most reasonable approach is to present the input vector containing x, y and z coordinates of the n surface nodes, k parameters characterizing the ribcage geometry, coordinates of the force contact point, and its magnitude. Overall, this results in $3n + k + 4$ neurons in the input layer.

Given input data, the FEM simulation results in a set of displacements, which are used as the target output of the ANN. Therefore, the number of neurons in the output layer should be equal to $3n$ – the number of the surface node coordinates.

Due to the nature of the problem, a good choice of the network type is an artificial neural network learnt with the backpropagation algorithm (BPANN). In this type of network, each layer consists of units which receive their input from nodes in a layer directly before and send their output to nodes in a layer directly after. There are no connections within a layer. Figure 29 presents a scheme of the multi-layer ANN with only one hidden layer.

A proper division of data into training, testing and validation sets is important. In the ideal situation, those three datasets would be sampled from the population in an independent-sample testing. However, in this case, there is a single dataset from which the population has already been sampled. Therefore, the existing sample will have to be randomly divided into three sets in a split-sample testing process.
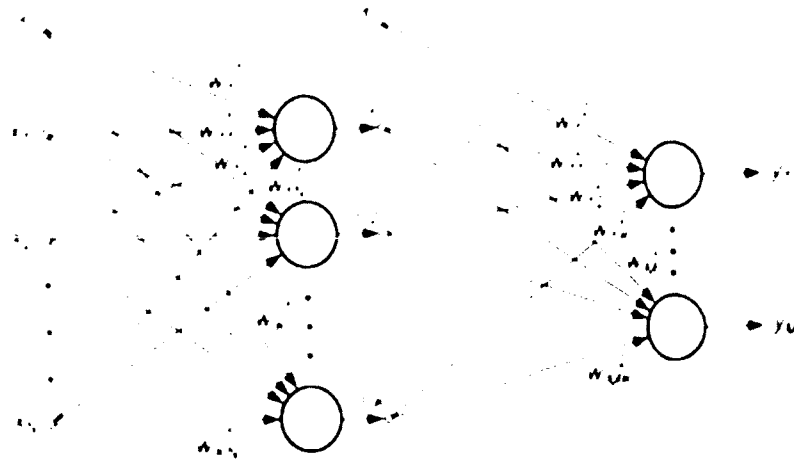
Figure 29. Scheme of the multi-layer artificial neural network with one hidden layer [74]

The training set is used to adjust or train the weights in the ANN in order to produce the desired outcome. The validation set is a set of examples used to find the best ANN configuration and to determine the optimal number of hidden neurons. The validation set is used to choose between multiple trained networks. The validation set can be used for stopping the training process, ensuring that the ANN is optimistically biased, having been exposed to the data.

The testing set is a set of samples used only to evaluate the fully trained ANN. It should be collected separately from the training and validation sets to ensure independence. The ANN is biased on both the training and validation sets, so the independent testing set must be used to determine generalization error. The testing set should never be used to choose between neural networks so that it remains an unbiased estimate of the ANN's generalization error.

The validation error will be used for choosing when to stop training. During that process the network's output error will be monotonically decreasing. The same will

happen with the validation error. However, at some point it is possible that it will start to increase after the initial stage of learning due to overfitting. If the validation error starts to rise for a significant number of iterations, training should be stopped and the weights that were generated at the minimum validation should be used in the network for operation.

A special emphasis has to be placed on the determination of an appropriate number of hidden layers and neurons in those layers. According to the Kolomogorov's theorem, if there are N neurons in the input layer, one hidden layer with ($2N + 1$) neurons should be sufficient to provide good generalization of the ANN. To provide good mapping, in this study, the objective will be to maintain one hidden layer. Additionally, the number of neurons in the hidden layer will be empirically established by retraining the BPANN with a varying number of nodes. The network characterized by the lowest validation error will be used.

Summarizing, the model relating displacements to the force applied will be based on the parameters of the fully trained BPANN. The overall workflow in this stage is presented in figure 30. All considerations in this step can be implemented using the Matlab Neural Network Toolbox.

```
┌─────────────────┐   ┌──────────┐   ┌──────────┐   ┌─────────────┐
│ Division of data│──▶│ Choosing │──▶│ Training │──▶│ Evaluating  │
│                 │   │  BPANN   │   │  BPANN   │   │validation   │
│                 │   │          │   │          │   │   error     │
└─────────────────┘   └──────────┘   └──────────┘   └─────────────┘
            Repeat for different configurations

┌─────────────┐   ┌─────────────┐   ┌─────────────┐
│Assessing the│◀──│Training the │◀──│Selecting the│
│best network │   │best network │   │best network │
└─────────────┘   └─────────────┘   └─────────────┘
```
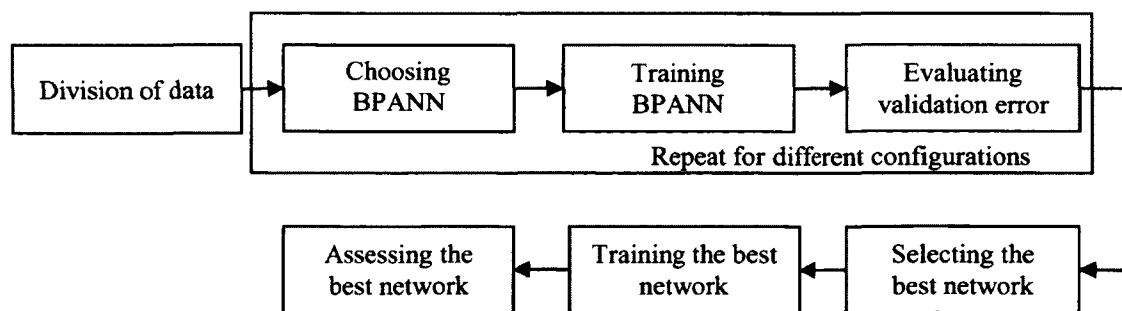
Figure 30. Workflow for developing the mathematical model for relating the displacement to the force applied

4.2 Verification and Validation

Evaluation will be performed once finished by experienced surgeons from the pectus clinic at the Children's Hospital of the King's Daughters, who have been practicing the Nuss procedure on a daily basis. They will be consulted intermittently in order to ensure an optimal solution.

Validation of the system may be performed by testing the planner with previously operated cases. A user would recreate a scenario, i.e. the ribcage geometry and location of the bar, and compare a simulated outcome with the actual result. In such a way, different cases can be studied in order to prove that the solution accomplishes its intended requirements.

We collected 3D surface scans of the chest from subjects with uncorrected PE prior to the Nuss procedure scheduled to be performed at CHKD and again after the surgery.

A comparison between each pair of scans was performed using the displacement map projected on the surface scan obtained prior to a surgery (fig. 31). A scaling factor was applied to compensate for the growth of the patients between scans. Point-to-point comparison was chosen due to its computational efficiency. For every point in the pre-surgery scan the displacement was calculated as the distance to the nearest point in the post-surgery scan. However, even perfectly registered surfaces will give a non-zero displacement because the surface is actually a mesh of discrete points and, in general, they do not coincide even if the surface does. However, the surfaces were characterized by similar resolutions, which should have prevented the introduction of inaccuracies.
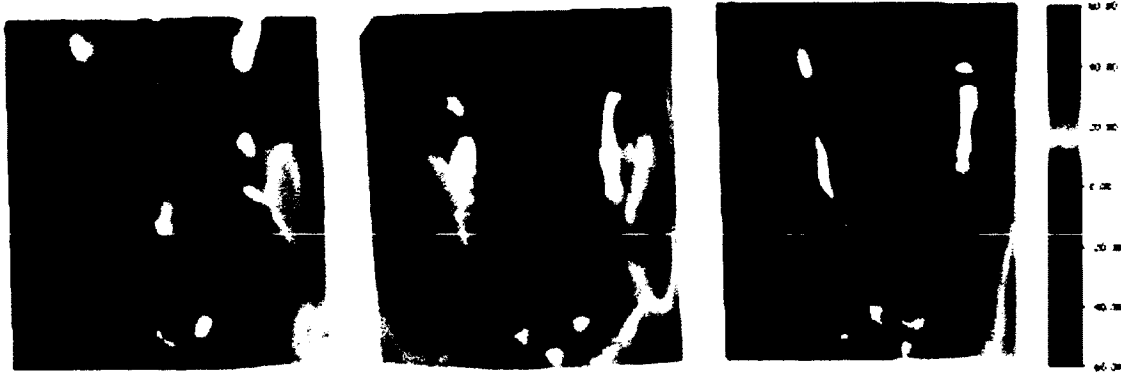
Figure 31. Comparison of the pre- and post-operative surface scans

4.3 Surgical Planner

Even though the Nuss procedure is a relatively simple method, various nuances can lead to suboptimal aesthetic results as reported by some patients. In a planning mode (fig. 32), first, the surgeon provides the patient specific parameters which allow generating the appropriate model of the ribcage. Then, the surgeon iteratively alters the position of the bar underneath the sternum. Changes in geometry of the ribcage, based on the force-deflection model presented in section 4.1.3, affect the external shape of the chest, which is one of the main goals of the Nuss procedure. Therefore, the planning process requires a reference shape of the chest which in this case is an average shape chest [75] discussed in section 4.2.1 (fig. 32). It is not expected that a surgeon would achieve such a shape, but by comparing different scenarios he could choose the most optimal location for the bar resulting in the smallest difference between the obtained shape of the chest and the average shape chest. Such a comparison could be performed between the actual outcome of the surgery and the average shape chest. This would result in an objective evaluation of performance. Similarly, a comparison between chest shapes

before and after surgery, as shown in figure 31, could serve as an objective improvement measure.
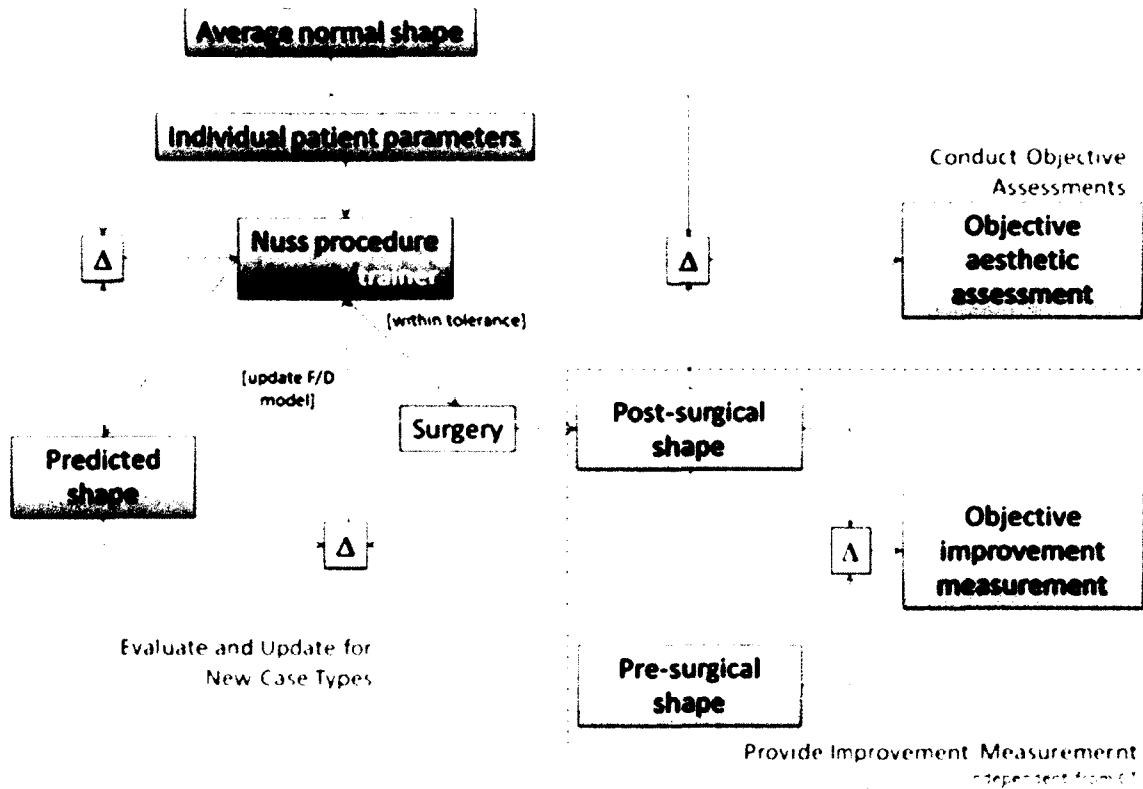
Figure 32. Use of the Nuss procedure planner

Additionally, figure 32 illustrates that a difference between the predicted shape and the actual post-surgical shape can be used to update the force-displacement model increasing the size of the training sample.

Eventually, the actual post-surgical shape can be compared with an average shape chest providing the objective aesthetic evaluation (figure 46 right).

4.3.1 Development of an Average Chest Shape

Eleven 3D surface scans of the chest without PE were obtained for the purpose of another study [76] using a FastScan laser scanner (Polhemus, VT, USA). Each scan (Figure 33) consists of eleven markers related to features on the cartilage and sternum out of which only three can be considered as useful in this study. Those landmarks are located on the sternal notch, center of the manubrium and xiphoid process.

The nature of 3D scanning using a handheld device assumes the existence of small errors in the scanner measurements caused by metal objects interfering with the magnetic locater, the movement of the object being scanned or movement of the reference. Therefore, a rigid body transformation is applied to scan sweep to minimize those errors (fig. 34 left).
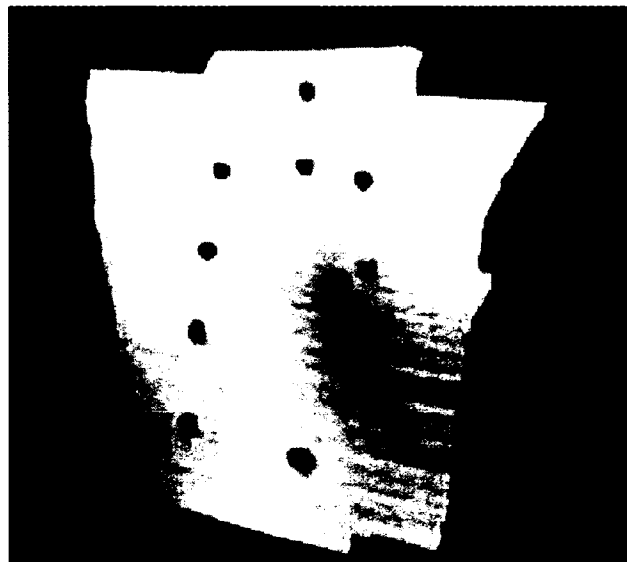
Figure 33. A single surface scan with landmarks

The surface model of skin can be built directly from a point cloud. In order to achieve that, all sweeps have to be merged (fig. 34 middle). If they do not overlap exactly, the surface will be irregular since jumping between points belonging to different seeps will occur. Therefore, smoothing has to be employed with a parameter controlling how much smoothing is used when merging sweeps. This value is chosen by trial and error. It should be small enough to preserve details and sufficiently large to merge sweeps correctly, even when they are not aligned perfectly.
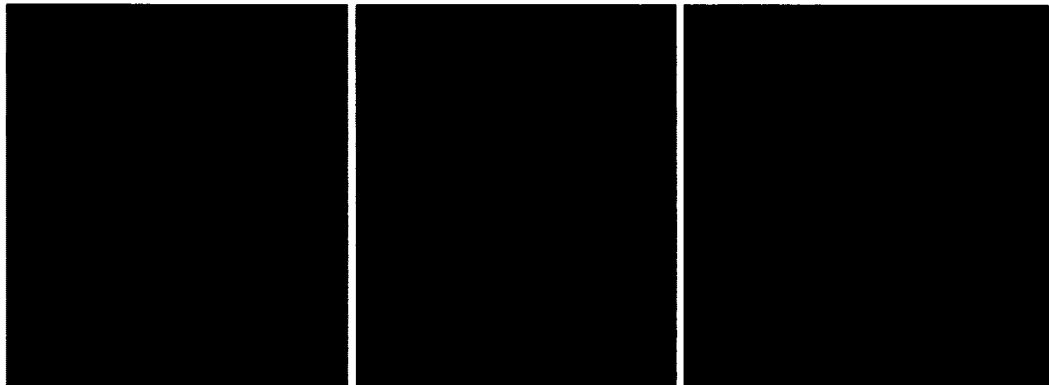
Figure 34. A point cloud consisted of registered sweeps (left), surface built from merged sweeps (middle), surface RBF interpolation (right)

Also, creating a surface is usually performed with specified decimation in order to reduce the number of points and triangles, since the scanning resolution is typically higher than is actually needed. Decimation is also used to control blistering where less decimation introduces more blistering, and large values may be completely free of it.

A surface created by simply joining points belonging to a cloud may still contain holes and defects which would require a significant amount of work. Therefore, a hole filling and extrapolation method that would not compromise scan accuracy and geometry,

such as RBF interpolation, has to be applied (fig. 34 right). In addition, it must allow for controlling a number of vertices, triangles or accuracy of the surface.

No other technique can model irregular, non-uniformly sampled data as effectively as RBF interpolation. It involves approximation of a real valued function $f(x)$ by the RBF interpolant $s(x)$ given in the form of:

$$s(x) = p(x) + \sum_{i=1}^{N} \lambda_i \phi(|x - x_i|), \qquad x \in \mathbb{R}^3, \qquad (9)$$

where N is a number of approximation points, p is a polynomial of degree at most k, λ_i is a real-valued weight, $|\cdot|$ denotes the Euclidean norm, Φ is a basis function, and $|x - x_i|$ is simply a distance - how far x is from the point x_i.

By setting $c = (c_1,...,c_l)$ as the coefficients that give $p = (p_1,...,p_l)$ in terms of the basis, the interpolant can be found by solving the following set of equations for c and λ:

$$\begin{bmatrix} A & P \\ P^T & 0 \end{bmatrix} \begin{bmatrix} \lambda \\ c \end{bmatrix} = \begin{bmatrix} f \\ 0 \end{bmatrix}, \qquad (10)$$

where $A_{i,j} = \Phi(|x_i - x_j|)$ for $i,j = 1,...,N$ and $P_{i,j} = p_j(x_i)$ for $i = 1,...,N, j = 1,...,l$.

A direct solution of Eq. (10) requires $O(N^3)$ operations and $O(N^2)$ storage. Moreover, naïve evaluation of equation (9) at M points requires $O(MN)$ operations. It is computationally demanding for larger datasets exceeding a few thousand data points. Therefore, fast approximation methods to fit RBFs and to evaluate RBFs are required. This means that true equality at the interpolation nodes is never achieved. The maximum difference between the fitted RBF value and the given values is called the fitting accuracy:

$$\max|s(x_i) - f_i|, \quad i = 1,...,N. \qquad (11)$$

Similarly, given a point x, calculating the value of the interpolant is called evaluating the RBF.

Eventually, an RBF surface is created in the process of isosurfacing. It consists of extracting an isosurface of a function, either as a set of points or as a mesh of polygons. Given a density function s, an isosurface at value a is defined as the set of all points x where $s(x) = a$. In the context of surface reconstruction, where s represents a signed-distance function, the reconstructed surface corresponds to the isosurface where $s = 0$.

This solution is implemented in the FastRBF™ library (FarField Technology Ltd, New Zealand) that is fully accessible from the FastScan™ software and offers the creation of a hole-free, smooth surface. That RBF surface can be exported to widely used engineering formats, like STL, IGES, OBJ. Such files can be further used in other software.

All scans have to be brought into correspondence in terms of orientation. A two-step registration process is employed using Delta (ARANZ, New Zealand). First, landmarks are used (figure 35) to produce a coarse registration; then, the surface data itself is used to complete a fine registration. The surface registration uses circular surface patches around each landmark on the reference and subject scans to closer align the objects.

Statistical shape analysis cannot be performed unless consistency among scans is ensured. In other words, the same point across the whole dataset has to represent the same feature. In order to achieve this, an interpolant that fits a surface to achieve better alignment among objects was created.

In the next step, an equally spaced 2D mesh for each scan is built, where a user decides its resolution. In our case, the mesh has 50 units in width by 100 units in height. However, this parameter can be adjusted to one's needs.

Because all scans must cover the same area of the chest, the "red" landmark

(sternal notch) and "blue" landmark (xiphoid process) limits a scan horizontally, whereas

the "yellow" landmark (the first left cartilage) and its projection in the x direction around

the "red" limits a scan vertically (fig. 35).

Figure 35. Surface scan with landmarks for registration [75]

Using the "yellow" landmark is required because of a lack of any distinctive

anatomical features that could be used for that purpose. A future dataset will have a larger

area covered and, for the vertical limitation, more reliable landmarks. Then, for each

vertex of the mesh, an interpolant is evaluated that results in the third coordinate (fig. 36)

being a linear interpolation of the value at that location.

A linear interpolator has the capability to fill holes within a convex hull defined

by the dataset. However, if a hole is too big, that approximation is not very accurate. In

the case of missing data outside the convex hull and inside the area defined by the re-

meshing process, a linear interpolant cannot be used and the nearest neighbor method is not correct.

Therefore, we propose multiple parallel cross-sections through the surface that results in a set of profiles. Points belonging to those profiles are used to fit curves that are later used for sampling. Based on those data points, a new interpolant is created. The cross-sections method can not only extrapolate points outside the convex hull but also interpolate data points that are missing within it.
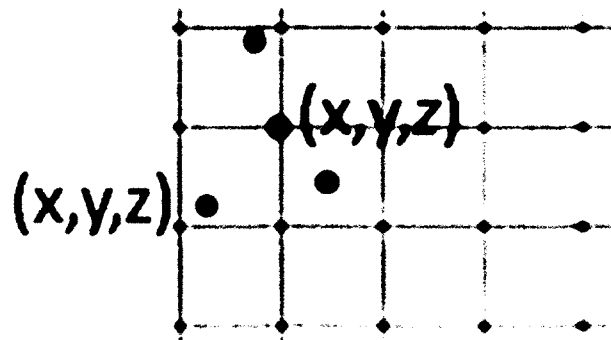
Figure 36. Mesh with the original vertex coordinates (blue), original data points (red), and interpolated coordinates (green) [75]

Consistency among scans allows the creation of a shape vector, which describes each geometry. Typically, it contains all coordinates of vertices that belong to a shape. In our study, for each mesh, we have a shape vector denoted by

$$s_n = \left(c_x^1, c_y^1, c_z^1, \dots, c_x^m, c_y^m, c_z^m\right) \qquad (12)$$

where c_x^j, c_y^j, c_z^j are respectively the coordinates of vertex j in the x, y, and z directions, m is the number of vertices of a mesh, and n is the index of scanned data. Since spacing of the 2D mesh was 50 by 100 units, each shape vector contains 15453 elements ($m = 5151$).

Once the creation of a shape vector is complete, we are ready to apply mean and multivariate analysis. An average shape is a set of averaged coordinates of each vertex. In addition, we have applied the PCA on a set of shape vectors. PCA decomposes the initial dataset into principal components along the largest variation among multiple shapes. It involves spectral decomposition of the covariance matrix denoted by

$$\Sigma = \Gamma \Lambda \Gamma'$$ (13)

where Λ is the diagonal matrix whose diagonal elements are eigenvalues of Σ and Γ is the orthogonal matrix whose columns are eigenvectors of Σ.

Besides studying variation in shape, PCA is used to reduce the amount of information stored. Each shape can be presented as a weighted sum of eigenvectors and the average shape denoted by

$$s_n = a_{sh} + \sum e_c (z_n)_c$$ (14)

where a_{sh} is the average shape, e_c is the cth eigenvector and $(z_n)_c$ is the cth eigen weight of the nth shape. Initially, the number of components is equal to the number of data points ($c = 15453$). However, by studying the variance explained by each component, we want to reduce that number drastically.

4.4 Surgical Trainer

As stated by the surgeons from CHKD, the highest risk and concern during the procedure is related to making a pathway for the bar using a surgical tool called an introducer because the heart can be punctured. Therefore, an emphasis is placed on mastering this skill during training. Additionally, the location of an entrance into the chest cavity is crucial and an incorrect choice can lead to displacement of the bar over

time or suboptimal results. We leverage the core model design of the surgical planner to create a Nuss procedure surgical trainer (fig. 37).

As shown in figure 37, a patient specific model is created from the database of previously operated cases (case data bank). The surgeon makes a pathway by manipulating a haptic device which transfers those movements to the virtual model of the introducer. At the same time, force feedback is provided to increase realism of the simulation. Additionally, the surgeon manipulates the thoracoscope which provides a view into the chest cavity. After the pathway is created, the surgeon iteratively alters the position of the bar underneath the sternum. Real-time changes in geometry of the ribcage affect the external shape of the chest, which is one of the main goals of the Nuss procedure. The predicted shape is compared with an average shape chest in order to objectively assess aesthetic outcome and overall improvement (fig. 37 left).

An average shape is being used for evaluation of the plan developed by the surgeon during training. This average has been developed based on a sample of normal subjects' surface scans [75].

For calculating and visualizating the difference between the chest shape and an average chest shape, a variation of the mesh deformation algorithm is used. Vertices are not displaced, but only distances are calculated. By applying different colors to vertices, the differences can be visualized.

Performance Evaluation

Average normal shape /
Post-surgical shapes

↓

Predicted
shape

Cases Recreation

Case data bank

Nuss procedure

Instructions
Performance feedback
Outcome feedback

Feedback

Haptic device

Mechanical Force Generation and
Intelligent Tutoring Instruction
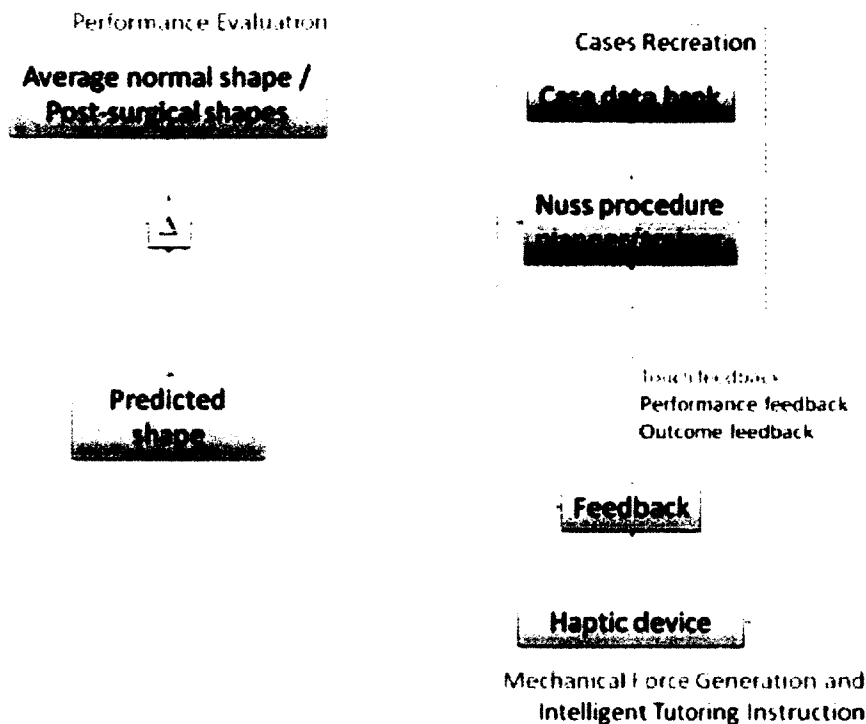
Figure 37. Use of the Nuss procedure trainer

Devices provided by Sensable (currently part of Geomagic) were the best choice for this application. They come in different types allowing a variety of workspaces and maximal forces. Some of them offer 6 DOF capabilities.

Although in our setup we incorporated the Phantom Premium 1.5/6DOF device (fig. 38), any compatible Phantom device can be used. Phantom 1.5/6DOF is characterized by a 381 W x 267 H x 191 D mm workspace, nominal translational position resolution 0.03 mm and maximum exertable force at nominal position equal to 8.5 N.

Figure 38. Phantom Premium 1.5/6DOF

Since the Phantom is expected to work in the Virtools environment, a driver had to be developed using the Virtools SDK and the Phantom API. The Virtools SDK was used to provide structure for the input data to the haptic device and output information from the device to Virtools. To communicate with the device itself, the HDAPI was used. The HDAPI is a low-level foundational layer for haptics developers who are familiar with haptic paradigms and sending forces directly to the device.

Since the refresh rate in Virtools does not have to be higher than 60 Hz to provide realistic animation and the haptic device update frequency is 1000 Hz, the device is working in the asynchronous mode, i.e. it runs as a separate thread and provides information to Virtools upon request.

```
┌─────────────────────────────┐
│   Initialize haptic device  │
│      Define obstacles       │
│       Start scheduler       │
└─────────────────────────────┘
              │
              ▼
┌─────────────────────────────┐
│         Servo loop          │
│       Get device info       │
│    Output proxy position    │
│     Collision detection     │
│      Force calculation      │
│      Commanding force       │
└─────────────────────────────┘
              │
              ▼
┌─────────────────────────────┐
│        Stop scheduler       │
│       Clean up device       │
└─────────────────────────────┘
```
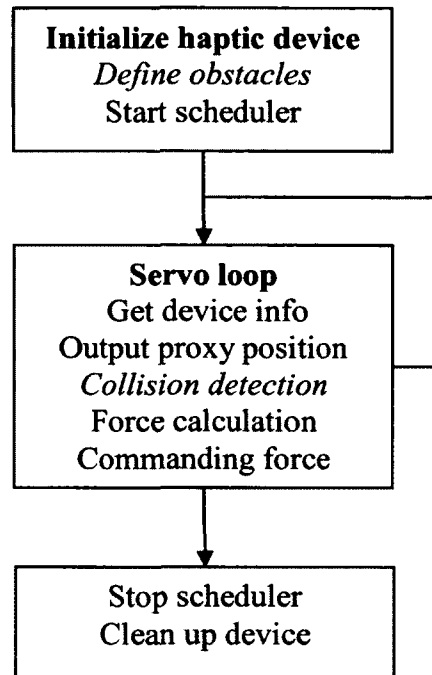
Figure 39. Design of the Phantom driver using HDAPI and Virtools SDK

Figure 39 shows the design of the Phantom driver using HDAPI and Virtools SDK. Initialization of the haptic device includes creation of the Virtools collision manager, definition of obstacles and starting the scheduler.

Once the device is initialized, the servo loop constantly updates the state of the device. Every time a Virtools frame is refreshed, haptic position and quaternion are queried. They are used to update the position of tools on the screen. At the same time, the collision manager is checking whether any intersection between the tool and obstacles has occurred. If collision occurs, then the end effector of the haptic device can "penetrate" the object, but the proxy has to remain on the surface of the virtual object (fig. 40). The difference, x, between the end effector position and proxy is used to calculate the force that is fed back to the device, according to:

$$F = -kx, \tag{15}$$

where k is the stiffness coefficient.

Surface contact point

Inside of the object

Haptic device end effector
virtual position
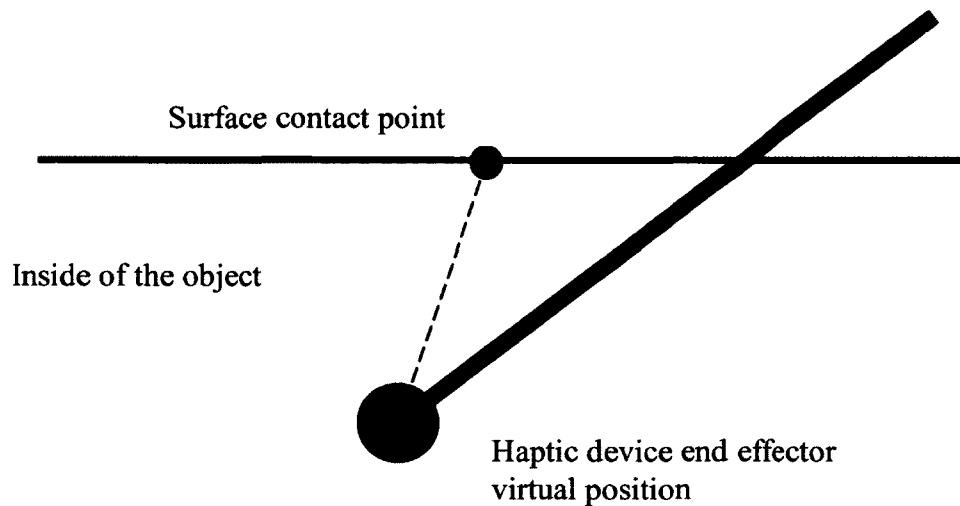
Figure 40. Collision realization by the haptic device

Once the driver is compiled, it can be utilized in Virtools (fig. 41). Position, quaternion, collision point, normal vector to the surface where the collision occurred and indication of the collision occurrence can be obtained through the driver.

Making a pathway includes operating an endoscopic camera in the vicinity of the heart. This is simulated by tracking an object with a similar shape to the endoscope. The most promising techniques of tracking are visual and inertial tracking. Currently, ARToolkit and Freespace inertial tracker are implemented through the Virtools SDK. Another inertial tracking device is the Wii remote controller. As opposed to the first two, it can be incorporated in Virtools using VRPN.
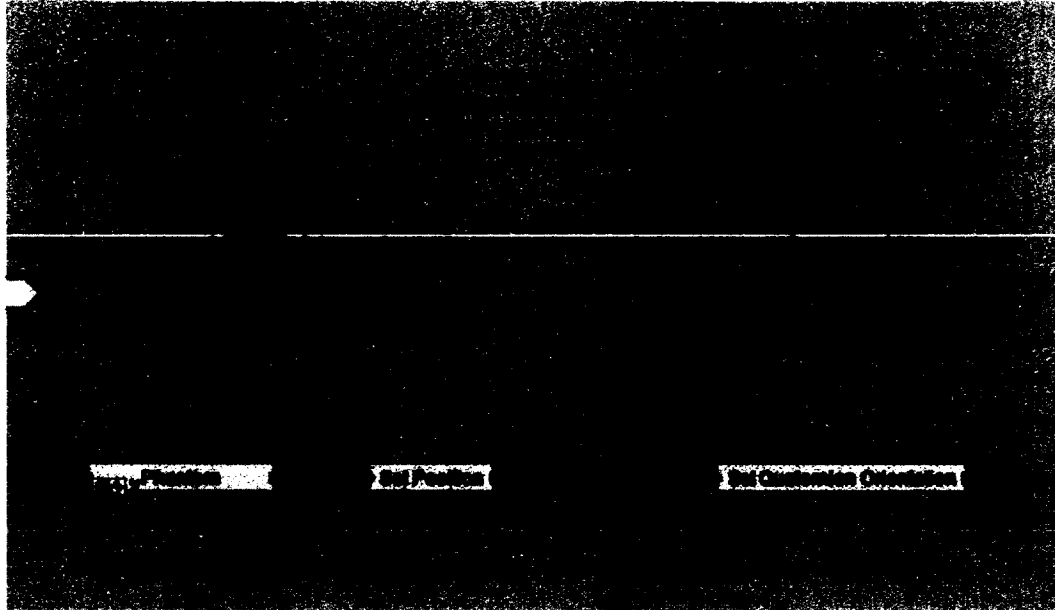
Figure 41. Phantom driver in Virtools environment

The main disadvantage of ARToolkit is its instability when there is insufficient light or the markers are too far away from the camera. Also, the Wii remote controller has only 5 DOF, and it needs to be combined with the bar containing a set of diodes. Based on the position of the diodes in a sensor, the missing degree of freedom can be compensated. The Freespace tracker has 6 DOF, but similarly to the Wii remote controller, translation of the tracker cannot be directly obtained. The simplest solution is integration of acceleration and application of the kinematic equation:

$$x(t) = x_0 + \dot{x}(t)t + \frac{1}{2}\ddot{x}(t)t^2 \tag{16}$$

where $x(t)$ is the position at the time t, x_0 is the initial position at $t = 0$, $\dot{x}(t)$ and $\ddot{x}(t)$ are velocity and acceleration at time t, respectively.

However, this method accumulates error and is not efficient in the long term. Other techniques for the approximation of solutions of ordinary differential equations, like the Runge-Kutta method, can be utilized instead.

With respect to mesh deformation for simulating skin, Virtools cannot deform meshes directly based on another object without the physics engine. An implementation using Virtools schematics, while valid, does not provide real time performance due to the iterative nature of the process. If the shape of the ribcage changes between iterations, the behavior of the skin will be incorrect.

To overcome this issue, a mesh deformation algorithm that is a variation of Virtools schematics was implemented in the Virtools Scripting Language which provides script level access to the Virtools SDK.

Because the bar will be interacting with the ribcage, eventually the interacting forces will be constantly scanned in order to calculate deformations and rebuild the surface model. The same forces can be fed back to the user through the haptic interface.

This system is meant to provide intelligent performance feedback based on predicted shape outcomes and comparisons to an averaged normal shape and to known successful post-surgical results for a specific case. The user would utilize this system to pick up a virtual scalpel, make incisions on a virtual PE chest, choose and insert a pectus bar into the PE chest, then receive a performance score. All is to be performed while receiving visual and tactile feedback.

An average shape chest is being used for evaluation of the plan developed by the surgeon during training. This average has been developed based on a sample of normal subjects' surface scans [75].

For calculating and visualizating the difference between the chest shape and an average chest shape, a variation of the mesh deformation algorithm is used. Vertices are not displaced, but only distances are calculated. By applying different colors to vertices, the differences can be visualized.

An example of a patient specific implementation in Virtools is shown in figure 42. It shows the thoracoscope in the form of an elongated cylinder, transparent skin, heart and lungs. A camera which shows the internal view of the model is located at the end of the thoracoscope. Three sizes of the introducers have been modeled based on the actual tools.

Figure 42. An example of a patient specific implementation in the VR environment

A custom made aluminum frame (figure 43) serves as the base for the remaining hardware which includes a Phantom 6 DOF, a 3D TV/monitor, a webcam (optional if visual tracking is used), and a semitransparent mirror. If a 3D monitor with NVIDA 3D

Active glasses is used, there is 90° change in polarization, and the projected image is significantly dimmed. A thin layer of another transparent film had to be placed on the monitor to apply an additional 90° rotation to polarization which resulted in the correct image. This problem does not occur when a 3D TV is used.

Figure 43. Hardware setup of the Nuss procedure simulator

CHAPTER 5

RESULTS

In this chapter an average shape of the chest is developed based on 3D surface scans; approximation of the force-deflection model is established based on FE analysis and is used to simulate sternum lifting similarly to the Nuss procedure characteristics. An average shape chest is used to evaluate different scenarios of bar placement. Real time performance of the model is evaluated in order to establish capabilities of the model to be used in the training mode.

5.1 Average Shape of the Chest

Before the average shape can be developed, the adequacy of the algorithm must be evaluated. As explained in the previous chapter, the scanning process can result in missing regions. The cross-section method was used to recreate the area of interest when data points at edges and inside a scan were removed. Figure 44 shows on the left the original scan with holes and on the right the original scan without holes.

The difference between the scan and the re-created surface is projected on the former in the form of a color map showing good approximation of the area of interest, especially where data points were removed. Dark red and dark blue color represent areas that were not approximated in this process. The maximal difference does not exceed 1 mm.
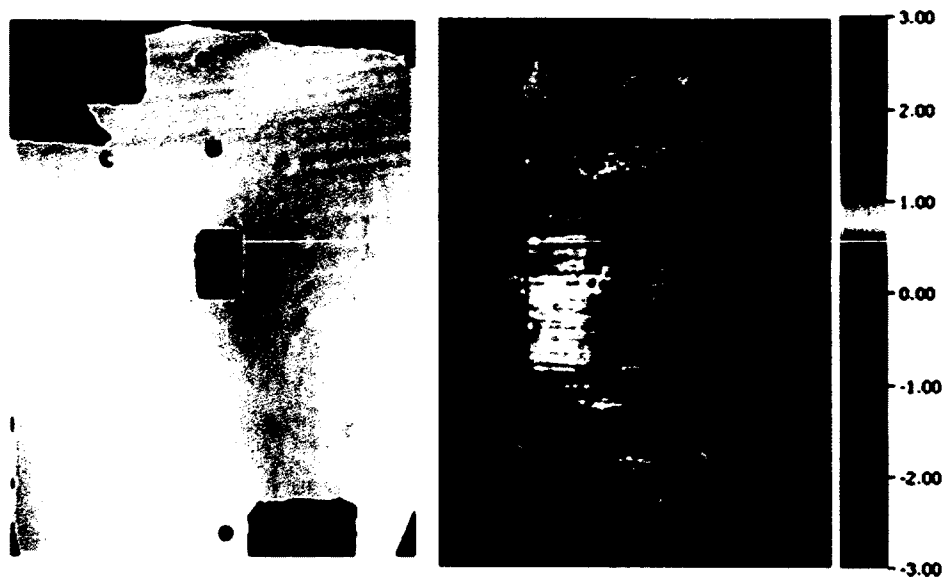
Figure 44. Original scan with artificially removed data points (left), original scan
compared with the recreated area interested (right), scale in mm [75]

Figure 45 shows the average shape created from calculating a mean over the

sample of 11 surface scans. It can be seen that it follows a normal shape of the chest with

a shallow depression in the middle.
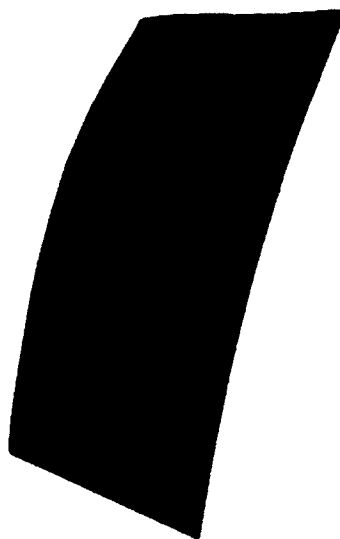
Figure 45. Average shape of the central chest

Since the landmarks undergo the same procedure, they can be used for evaluation of the surgical planning outcome. Because the Nuss procedure planning tool utilizes a deformable model of the ribcage, the landmarks for matching an average and predicted shape will be projections of internal features like, for instance, the sternal notch, center of the manubrium, and xiphoid process. It justifies the set of landmarks chosen for this study.

Figure 46 shows two cases where the actual outcome of the surgery has been evaluated using an average shape chest. Based on differences between the two shapes (presented as the colormap), it is possible to quantify results. The same approach is used for the evaluation of the outcome of the planning process.
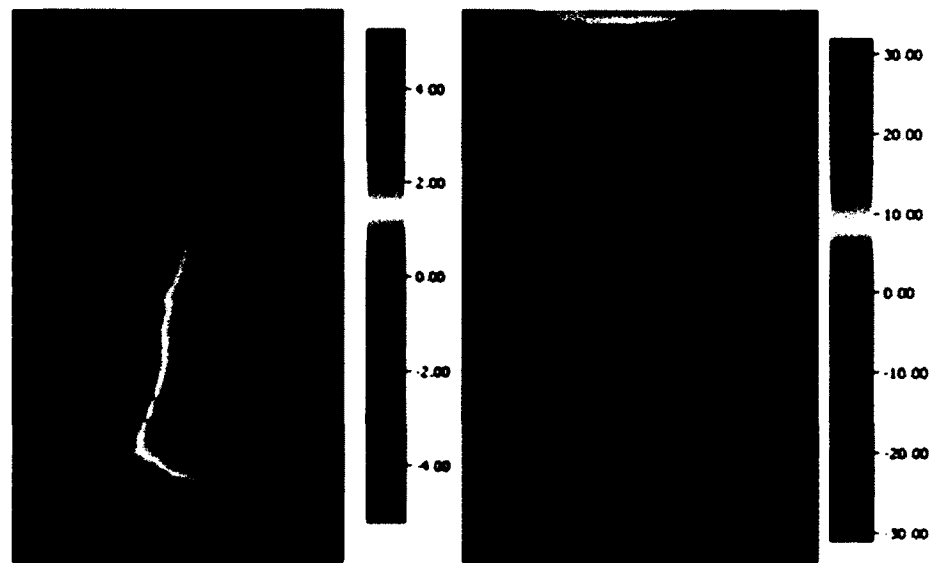
Figure 46. Comparison of an average chest shape with a normal chest without PE (left), and with the actual outcome of the surgery - suboptimal aesthetic results (right)

Performing the PCA allows studying variations in the shape of the chest. Results show that the first four components explain almost 100% of variability in the dataset, whereas the first two explain almost 90% (fig. 47). It means that each shape can be expressed as the sum of the average shape and a weighted sum of two to four components, which is a significant decrease of the amount of data that needs to be stored.
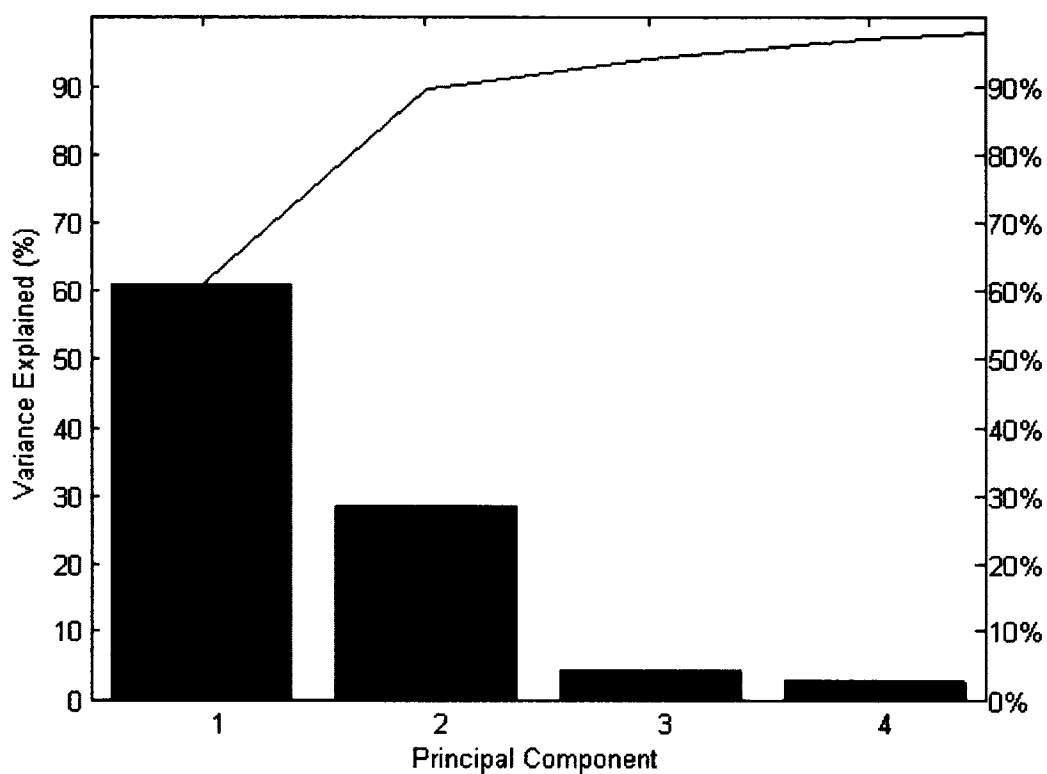
Figure 47. Variance explanation by the first four components

Figure 48 presents the first two principle components in the chest shape space. By varying weights, we can see extreme shapes for each component. The first component explains the overall change in size of the chest, whereas the second component explains

the width with curvature. It is likely that when the scans are normalized, the first component would represent the height alone.
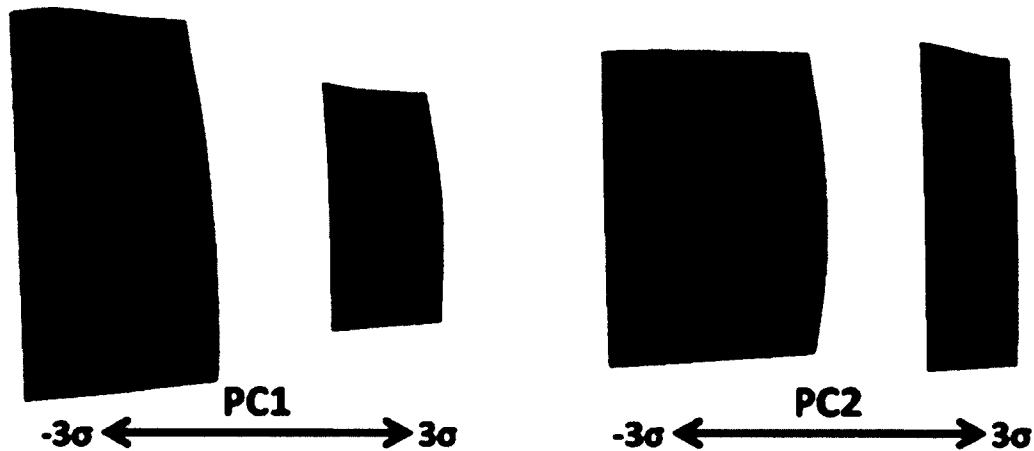
Figure 48. The first two principle components in the chest shape space

5.2 Finite Element Model of the Ribcage

The average Haller index for all 62 subjects was 4.1 with standard deviation equal to almost 0.9. The minimum was almost 2.7 which was slightly greater than 2.5 typically recognized as the normal value. The highest value of 6.5 indicates severe PE. Looking at the depression itself, the average value was over 18 mm with the maximum value of 40 mm and the minimum value of 0 mm.

Table 2. Summary of the patient specific parameters and Haller index

	Haller Index	Width [mm]	Sternal length [mm]	Depth [mm]	Depression [mm]
Average	4.1	252.24	152.93	142.45	18.18
Median	3.9	253	155	142	17
Standard deviation	0.84	22.12	21.33	13.25	8.21
Maximum	6.5	304	185	169	40
Minimum	2.69	203	93	113	0

Since the depression is measured as the distance between the highest point of the ribcage and the sternum, no depression means that the chest is flat and from studying the CT data for such cases it is apparent that the depression on the surface is caused by the muscle structure.
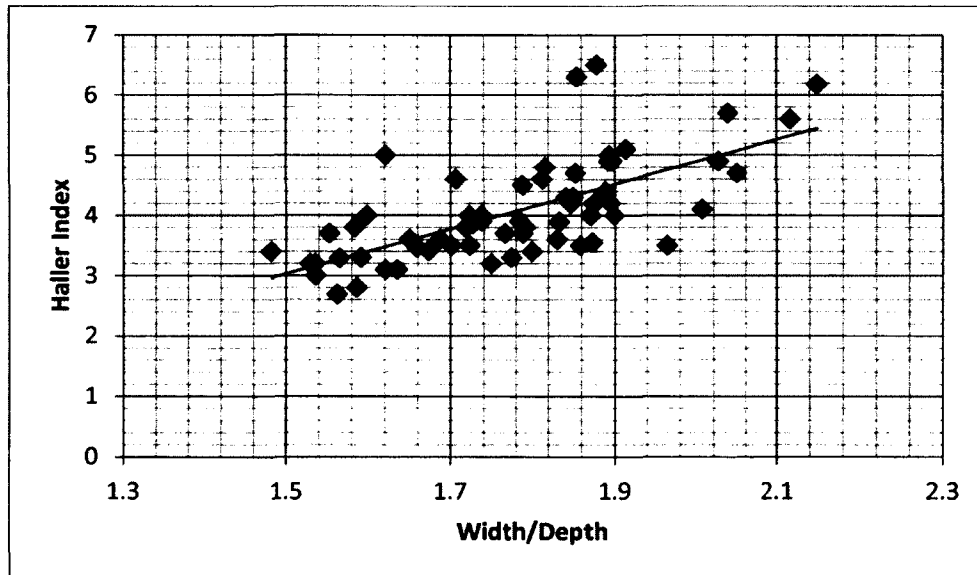
Figure 49. Relationship between the ratio of width and depth of the ribcage and the Haller index

While the parameters to deform the generic mode of the ribcage were being taken, it was noticed that a high Haller index did not guarantee a severe depression. For the minimal depression of 0 mm the respective Haller index (HI) was equal to 5.7. The correlation coefficient between the Haller index and depression was 0.35 demonstrating that there is minimal relationship between those two parameters. The correlation coefficient decreases to 0.25 when the HI is compared to the ratio between width and depth of the ribcage, and depression. However, a positive trend can be visible (Figure 49) when the ratio between the width and depth of the ribcage is compared with the Haller index. The correlation coefficient is equal to 0.67 in that case.
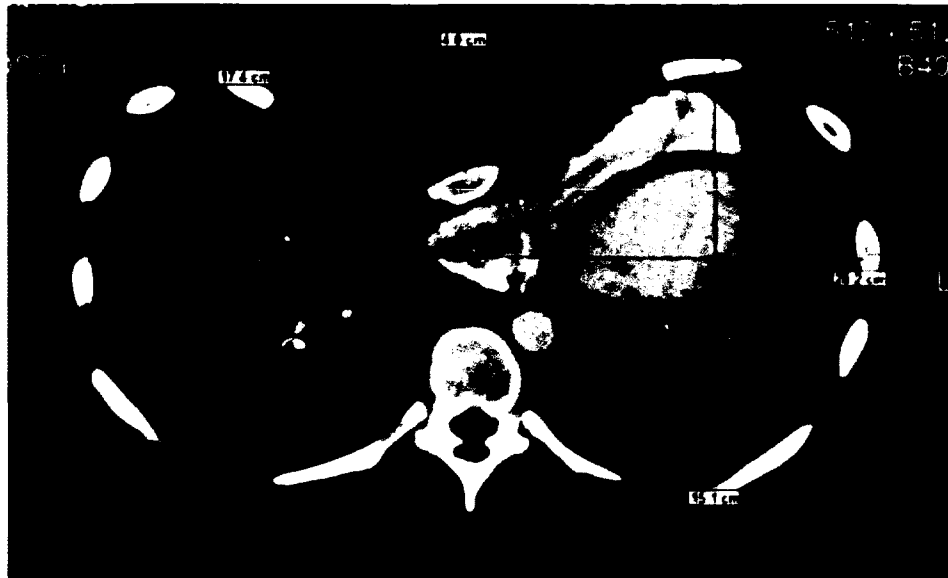
Figure 50. Measurements for the patient with the highest depression 40 mm (#3)

For each of the 62 patients, FEA took 3 minutes on an Intel Core2 Quad 2.5 GHz computer with 8 GB of RAM. Two patients characterized by deep depressions of 33 (patient #3) and 40 mm (patient #31) were chosen to present deformation results of the

FEM. In addition, patient #31 was characterized by the "oval" cross-section of the

ribcage. The oval ribcages are characterized by a high width to depth ratio. This shape

type is opposite to the "barrel" shape, matching more closely the ribcage of patient #3

and characterized by a smaller width to depth ratio. As reported by surgeons from

CHKD, the strategy for the bar placement changes based on the type of ribcage.
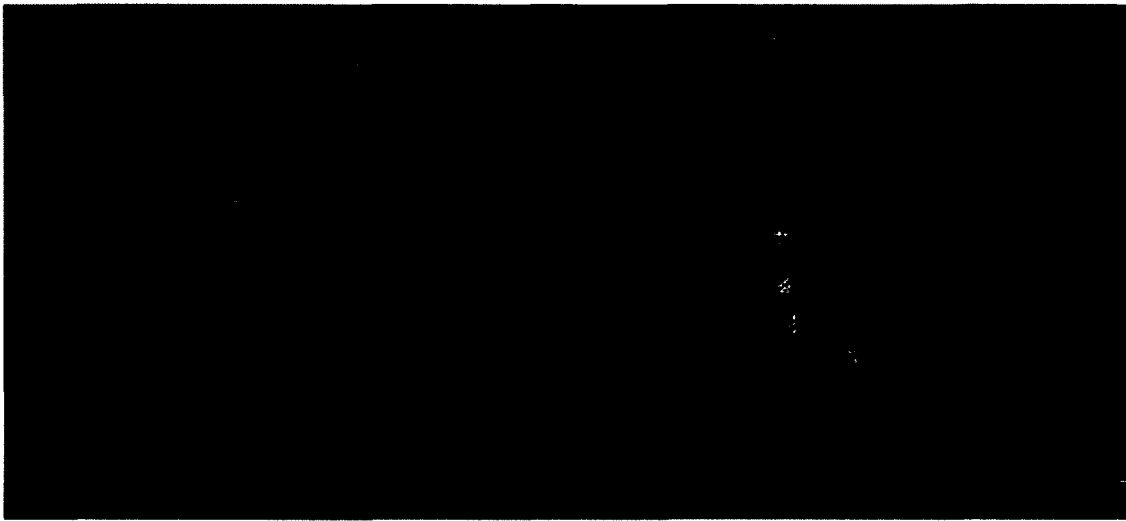
Figure 51. Geometric (left) and FE model (right) for the patient #3 with the highest
depression 40 mm

For patient #3, measurements taken from CT slices (fig. 50) were applied to the

generic model of the ribcage. Then, it was converted to a FE model and finite element

analysis was performed using load cases as defined in section 4.1.2.
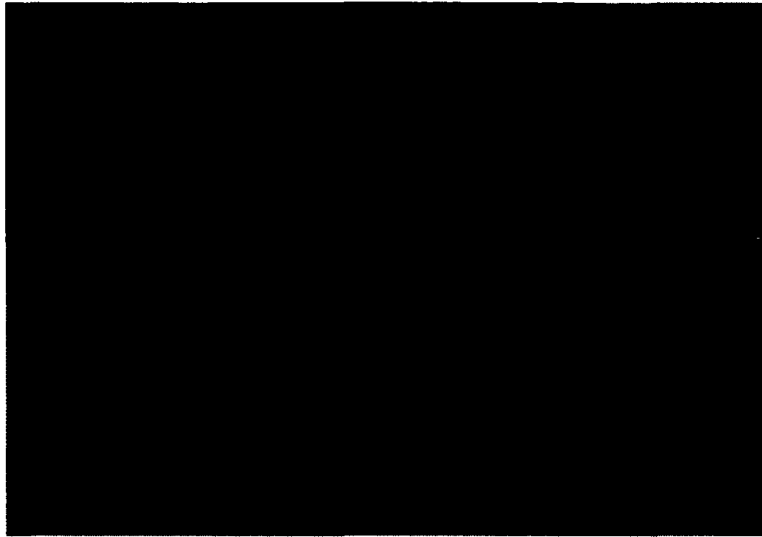
Figure 52. Displacement for F=50 N (patient #3)

Forces smaller than 100 N do not ensure high displacement in the cases of deep depression (fig. 52). Significant deformations start being observed when higher forces of 400-800 N are applied (fig. 53). The sternum reaches the correct position when forces of 1500-2000 N are applied.
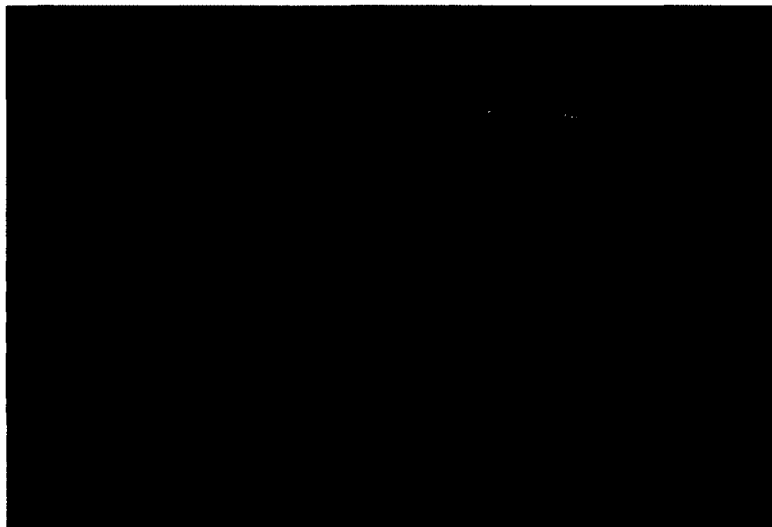
Figure 53. Displacement for F=400 N (patient #3)

It should be mentioned that 2000 N is the highest force needed to bring the sternum back to the right position since the maximal depth of depressions in the dataset is 40 mm. Since the model is linear, to lift the sternum by 20 mm, approximately 1000 N needs to be applied.

Furthermore, it can be seen that the ribs are also affected by lifting the sternum. This is in agreement with the previous studies [11] reporting transfer of stresses to the spine area. The magnitude of this phenomenon changes according to the stiffness of the cartilage.

Figure 54. Displacement for F=2000 N (patient #3)

From the presented results, we can learn that if a node is located further from the sternum, its displacement will be smaller. A significant set of nodes, mainly belonging to the ribs, will not be affected by forces applied to the sternum, and the displacement will be equal to 0.

Figure 55. Measurements for the patient with depression 33 mm and "oval" ribcage
(patient #31)

The oval shape type behaves similarly to the previous ribcage type when the

forces are applied. Due to smaller depressions, correct positioning of the sternum is

achieved by applying 1500 N (fig. 59).
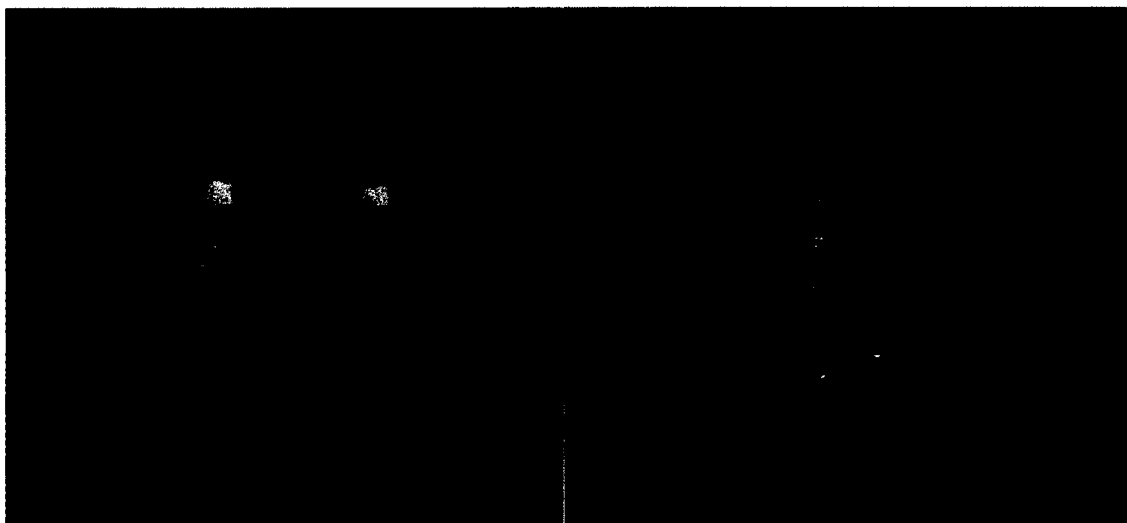
Figure 56. Geometric (left) and FE model (right) for the patient #31 with the "oval"
ribcage

At the level of forces smaller than 100 N (fig. 57), displacements are not significant. There is a very small difference between the deformed model and the original model. However, it starts to be visible when forces reach 400 N (fig. 58). Exertion of those forces do not have to be within the capabilities of an average person; however, a patient can be lifted using the introducer, and her/his weight can be leveraged to achieve appropriate loads.
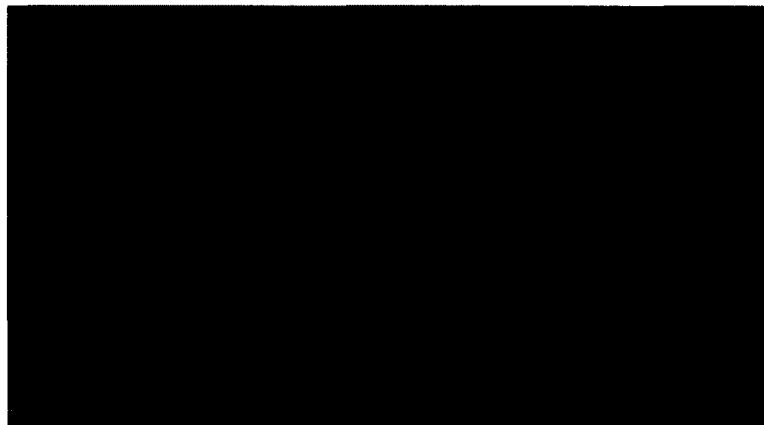
Figure 57. Displacement for F=50 N (patient #31)

Forces that need to be applied to the sternum are material properties dependent. As discussed in section 4.1.2, mechanical properties of the costal cartilage are not fully known and reported values differ at least by two orders of magnitude. However, resulted forces from this simulation can be scaled to match patient specific properties once known.

Figure 58. Displacement for F=400 N (patient #31)

Figure 59. Displacement for F=1500 N (patient #31)

5.3 Force-Displacement Model Approximation

An ANN was trained using the backpropagation method. In order to choose the appropriate structure, i.e. the number of neurons in the hidden layer, multiple ANNs were trained and the number of neurons in the hidden layer was iteratively changed. For each iteration, the measure of performance – MSE, was evaluated. The ANN with 20 neurons in the hidden layer was chosen and retrained.

Training stopped after 63 iterations with the best validation performance of about

0.01 (fig. 60). The error reaches steady state after the 23 epochs and steadily decreased.

The majority of errors were around 0.00324 (fig. 61). There were as well high

values of R close to 1. Such good fitting was probably because the patients overall did

not differ significantly and there was not a lot of variability in the parameters set. This

would not be the case if the torsion values were utilized.
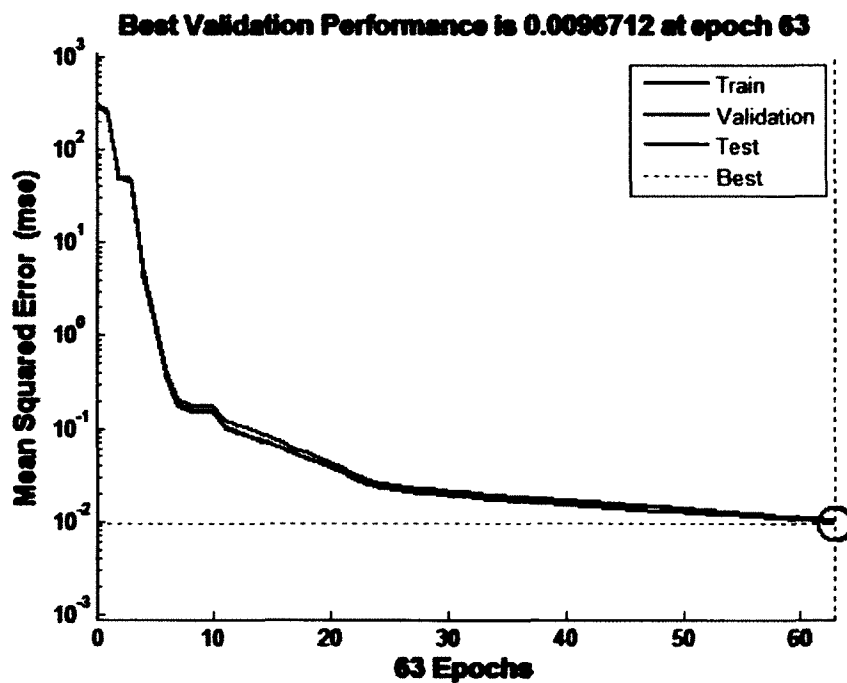
Figure 60. Performance of the ANN
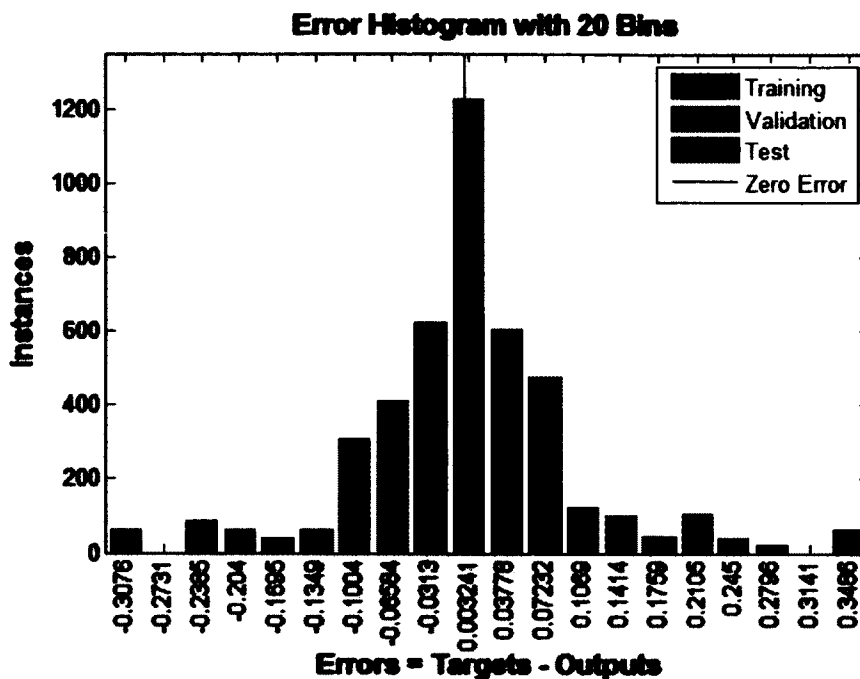
Figure 61. Error histogram for the chosen ANN

For further consideration, patient #57 data was used. This patient is characterized by width, sternal length and depth of the ribcage equal to 231, 168, and 123 mm. Although his depression is not the deepest among the dataset (21 mm), his HI is the highest and equal to 6.5. The choice of this patient was also motivated by the fact that pre- and post-surgical surface scans have been collected.
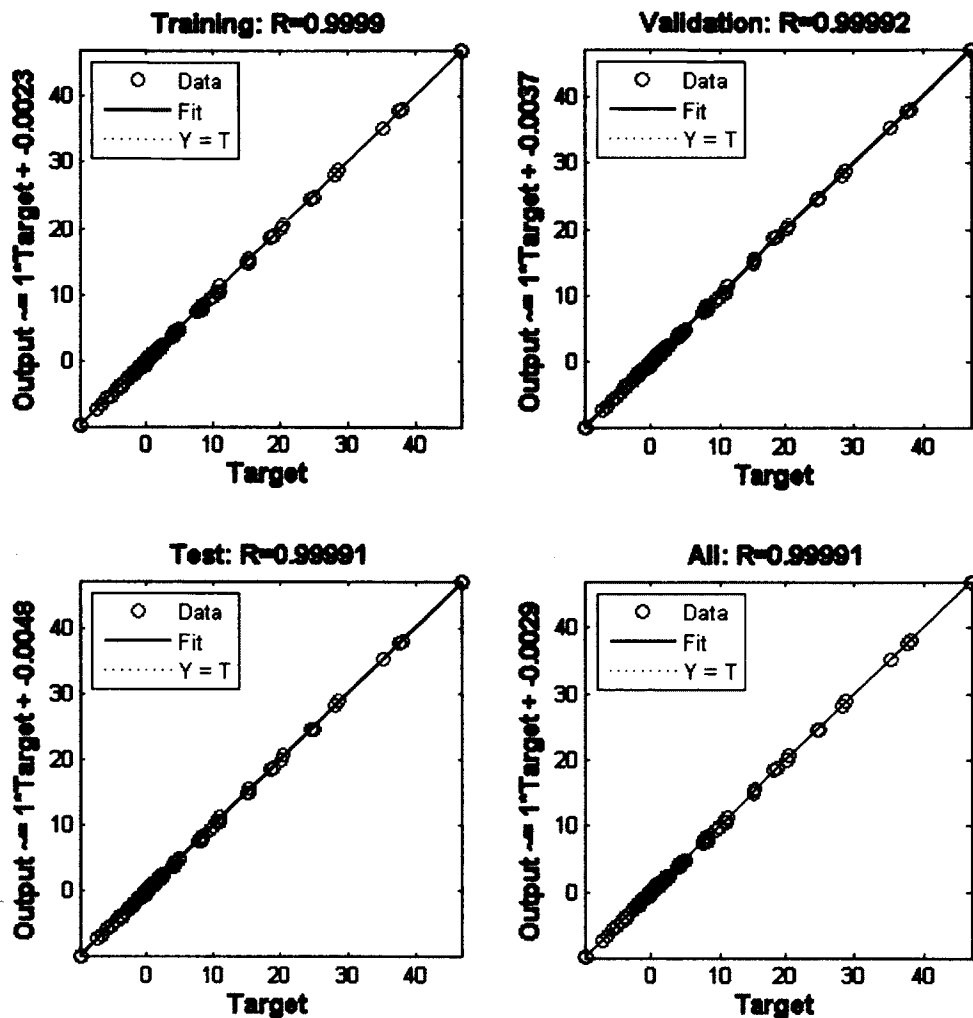
Figure 62. Regression plots

In order to assess patient specificity, the model deformation was compared with the patient's deformation. Out of 62 symmetric saucer shapes for which CT data was collected, two pre-operative surface scans were present as a result of another study. The more extreme case of the two was used for comparison.

Figure 64 shows the actual surface of the chest for patient #57 merged with the patient specific ribcage. When the relative skin model derived from the average chest shape is compared to the surface scan it shows a maximal difference of 5 mm (fig. 65).

This difference is located typically at the border of the shape and comes from the biased averaged model of the chest. Typically, normal subjects have better developed muscle structure than subjects with PE. Therefore, there is a natural mild depression that does not result from cartilage deformation.

Figure 63. Patient specific (patient #57) geometric model of the ribcage

Additionally, with regards to the average shape chest, the small sample of normal subjects allowed subject specific features to prevail in the averaging process. An additional source of errors was the post-processing of the surface scans. The registration process and creation of the surface will introduce errors that can influence the final results. Despite the differences, the error is not greater than ±2 mm in the middle of the chest. For future work, CT surface extraction will be utilized to generate the average error over all 62 patient cases.
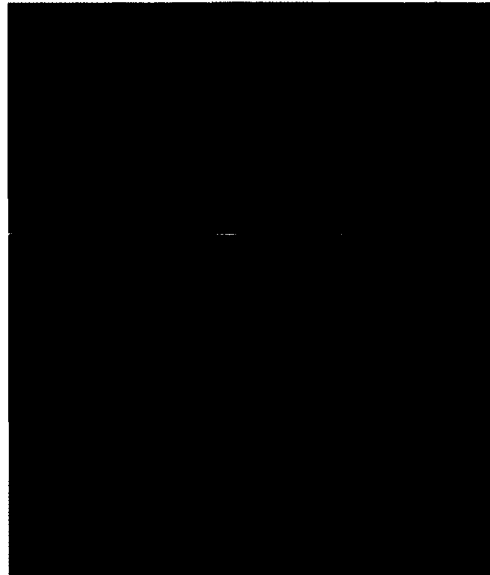
Figure 64. Surface model of the chest with the ribcage (patient #57)

To test the performance of the model, a force was applied to the sternum of the model representing the ribcage of patient #57 at different locations and with varying magnitude. Values for those variables were not presented to the ANN during training.

Figure 65. Comparison between the actual and simulated pre-surgical shape of the chest (scale in mm)

In the next step, the patient specific FE displacement and ANN approximation were compared. Since they are two different types of models in different formats, they needed to be reformatted and collocated. This is a slow manual process; therefore, the same data belonging to the extreme patient #57 was utilized.

In the first case, the force was applied to node 5217 which is located on the midline of the sternum between the first and second force position used for training. The magnitude of the load was varied from 300, 1000 and 1700 N.
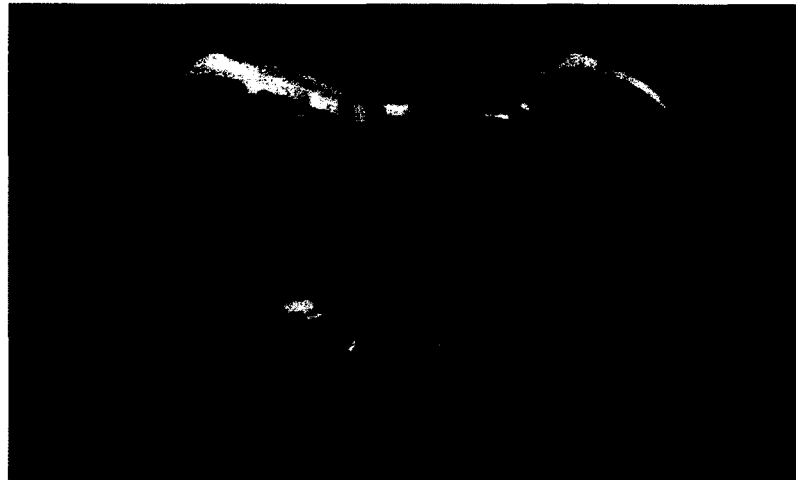
Figure 66. Comparison between the actual results of FEA (purple) and force-displacement model approximation (yellow) for F = 300 N applied to node 5217

It can be seen that for F=300 N the sternum has been lifted more than the actual result of the FEA (fig. 66). Around the location of the xyphoid process the difference is 3 mm and this decreases as the sternal notch is approached.

Figure 67. Comparison between the actual results of FEA (purple) and force-displacement model approximation (yellow) for F = 1000 N applied to node 5217

For F=1000 N, the results are quite the opposite. The approximation shows the sternum lifted less by 2 mm than was suggested by the FEA (fig. 67). This discrepancy may come from the fact that during the training process F=1000 N was within the widest interval (800, 1500).

Figure 68. Comparison between the actual results of FEA (purple) and force-displacement model approximation (yellow) for F = 1700 N applied to node 5217

A similar difference can be observed in the case of F=1700 N (fig. 68). That force lifted the sternum the most, almost to the undeformed level. The second location for the force applied to the sternum is off the midline approximately at the height of the third force used for training, located at the midline of the sternum being the farthest from the xyphoid process. Its magnitude varied and was equal to 300, 1000 and 1700 N.
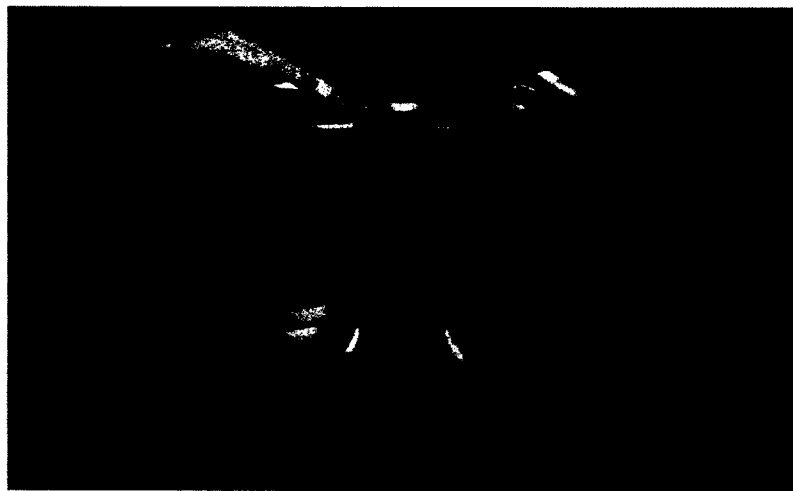
Figure 69. Comparison between the actual results of FEA (purple) and force-displacement model approximation (yellow) for F = 300 N applied to node 5125

Similar to the scenario where the force is applied to node 5217, there are some differences between the actual results of the FEA and the approximated force-deflection model.

Figure 70. Comparison between the actual results of FEA (purple) and force-displacement model approximation (yellow) for F = 1000 N applied to node 5125

For F=300 N, the sternum was lifted by approximately 2 mm higher than in the FE model (fig. 69). Despite the off midline force application, sternal torsion is not observed.

Figure 71. Comparison between the actual results of FEA (purple) and force-displacement model approximation (yellow) for F = 1700 N applied to node 5125

Similarly, the sternum was lifted minimally more than during FEA when F=1000 N (fig. 70) and F=1700 N (fig. 71). Despite a much higher force, sternal torsion was not observed. It can be also seen that despite the same magnitude, the sternum was lifted less in the case of the second force location.

5.4 Validation

Validation is performed by comparing the simulated shape of the chest and the corresponding post-surgical surface scan (fig. 72). Based on the post-surgical x-ray for patient #57 (fig. 73), the bar is in contact with the sternum almost at its end. Although the sternum cannot be clearly seen in this modality, it was possible to establish the bar position using the back ribs. This information was applied to the model in order to simulate that actual Nuss procedure. However, information about the force magnitude was not known. From previous results, it is known that the force needed to bring the sternum back to the correct position is between 1500 and 2000 N. Since the force magnitude needed to bring the sternum back to the correct position decreases as it approaches the end of the sternum, the force applied was equal to 1500 N.

When the post-surgical surface scan was compared with the simulated skin shape, the maximal difference between two shapes was 13 mm (fig. 74). However, in the middle of the chest the difference was 7 mm. This value can result from the concavity in the middle of the patient's chest, probably created by the muscle structure.

Figure 72. Post-surgical surface scan for patient #57

Accuracy of the validation process can be also influenced by the fact that there is discrepancy between the time when the CT data, x-ray and surface scans were taken. In extreme cases, 2-3 years can pass from taking CT and surface scans. Patients, especially those younger, can grow significantly during that time.
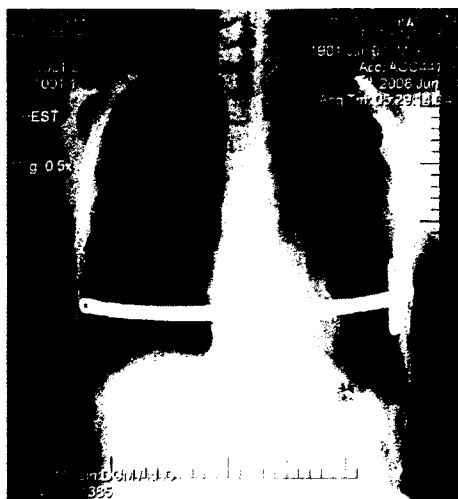
Figure 73. Post-surgical x-ray for patient #57

A long term study relating position of the bar to the shape of the chest is needed to fully validate the performance of the planner. This will include pre-operative surface scans, post-operative x-rays to obtain bar position, post-operative surface scans and predicted shapes from the simulator.
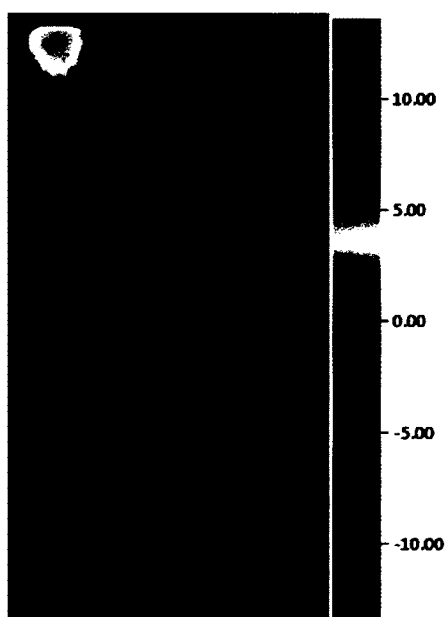
Figure 74. Comparison between the simulated skin shape and post-surgical surface scan (scale in mm)

5.5 Evaluation of the Outcome

An average shape is used to evaluate the outcome of the surgery based on two scenarios. In the first scenario, the pectus bar comes in contact with the sternum of patient #57 at node 5217, and 1700 N is applied to the sternum.

From figure 75, it can be seen that the difference between the obtained chest shape and an average shape is at most 2.3 mm. This suggests that this location could obtain good aesthetic results.
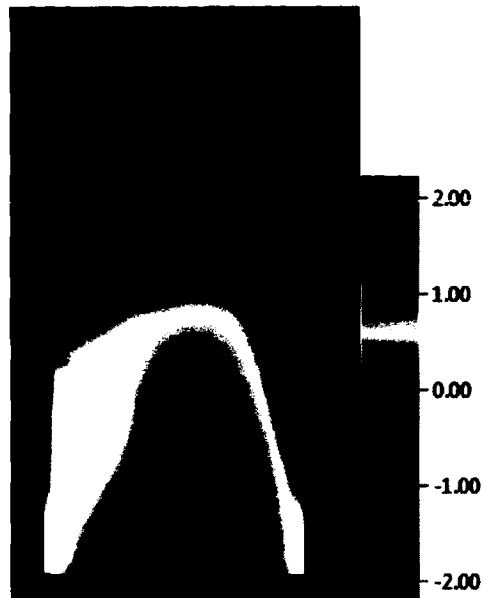
Figure 75. Comparison between the simulated shape of the chest with an average chest shape for F=1700 N and node 5217 (scale in mm)

The second scenario assumes that the bar is located 20 mm further from the first location toward the beginning of the sternum. The same force of F=1700 N is applied to the back of the sternum.

Figure 76 shows that in the case of this scenario differences are higher and reach almost 16 mm. The pattern of differences is almost identical to the first scenario. In this case, in order to achieve better aesthetic results, a surgeon would have to apply a higher force, which could negatively influence the patient's comfort after surgery.
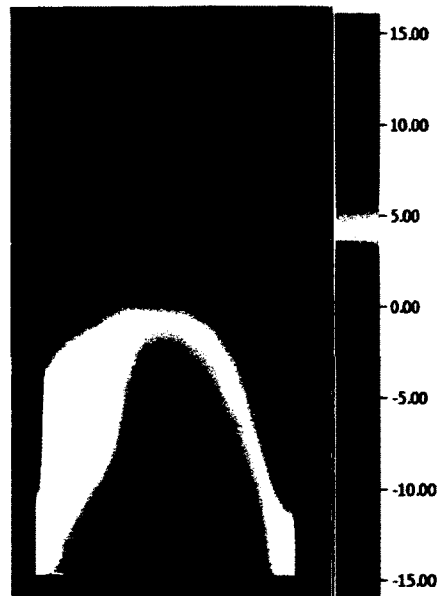
Figure 76. Comparison between the simulated shape of the chest with an average chest shape for F=1700 N and node 5217

When both results are presented in the same scale derived from the worst case scenario (fig. 77), it can be seen that the first scenario results in significantly better results, which suggests the choice of the best plan for the surgery.

Figure 77. Outcome of both scenarios presented in the same scale (scale in mm)

5.6 Real-time Deformations Based on the Force-Deflection Model

The force-deflection model was implemented in Virtools. The force remained unchanged. There are two locations – node 5217 and 5125 – and three options for the magnitude: 300, 1000, and 1700 N. In addition to the ribcage, the skin model is deformed. To test the real-time performance, location and magnitude change iteratively with each simulation time step.

Figure 78 shows the deformation for the force location at node 5217 which is closer to the end of the sternum. During simulation the refresh rate was varying and in some cases was decreasing to approximately 20 Hz occasionally rising to approximately 30 Hz.

Similarly, for the second location, node 5125, the refresh rate was varying between 20 and 30 Hz (fig. 79). Eventually, the simulation will contain other models and other processes, like collision detection, haptics and tracking, that will negatively influence the refresh rate.
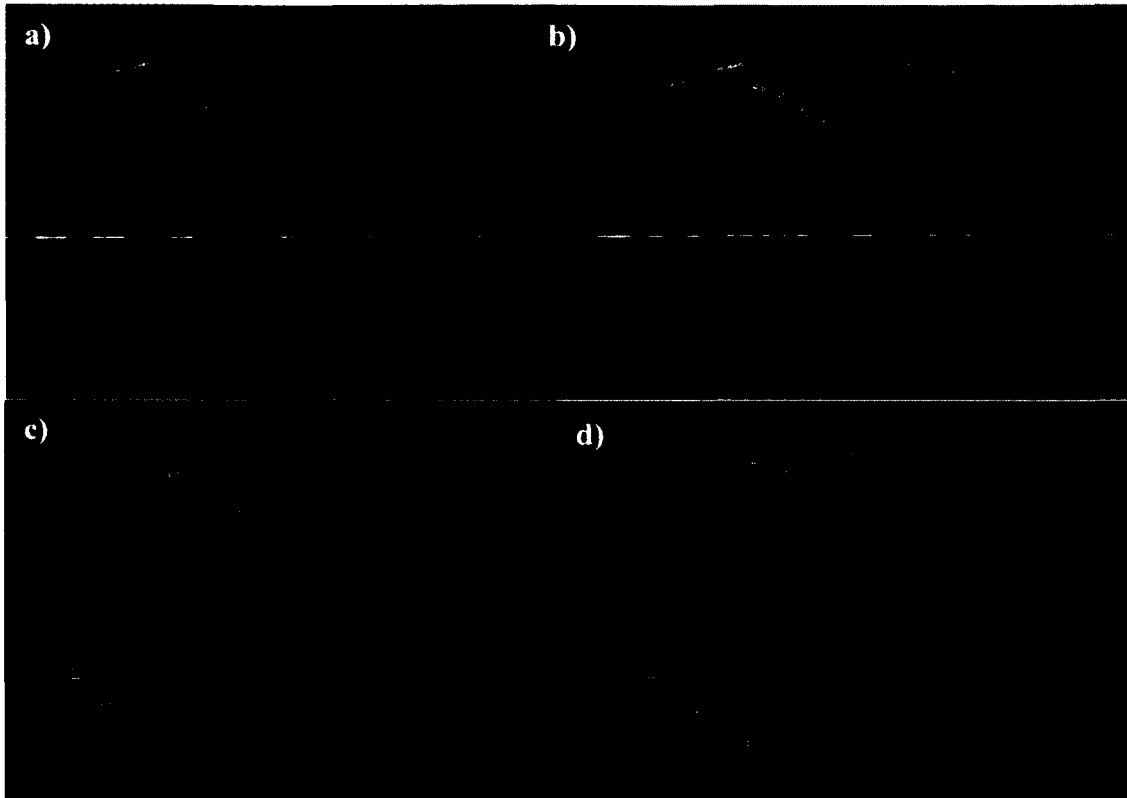
Figure 78. VR implementation of the force-deflection model the force applied to node 5217: a) F=0 N, b) F=300 N, c) F=1000 N, d) F=1700 N

Another parameter negatively influencing the refresh rate is the number of vertices in the ribcage and skin models. Even though the majority of vertices do not change their location due to the forces applied, they need to be redrawn each time step. Additionally, in order to provide a smooth model of the skin, it has to be tessellated with high resolution further affecting the performance.
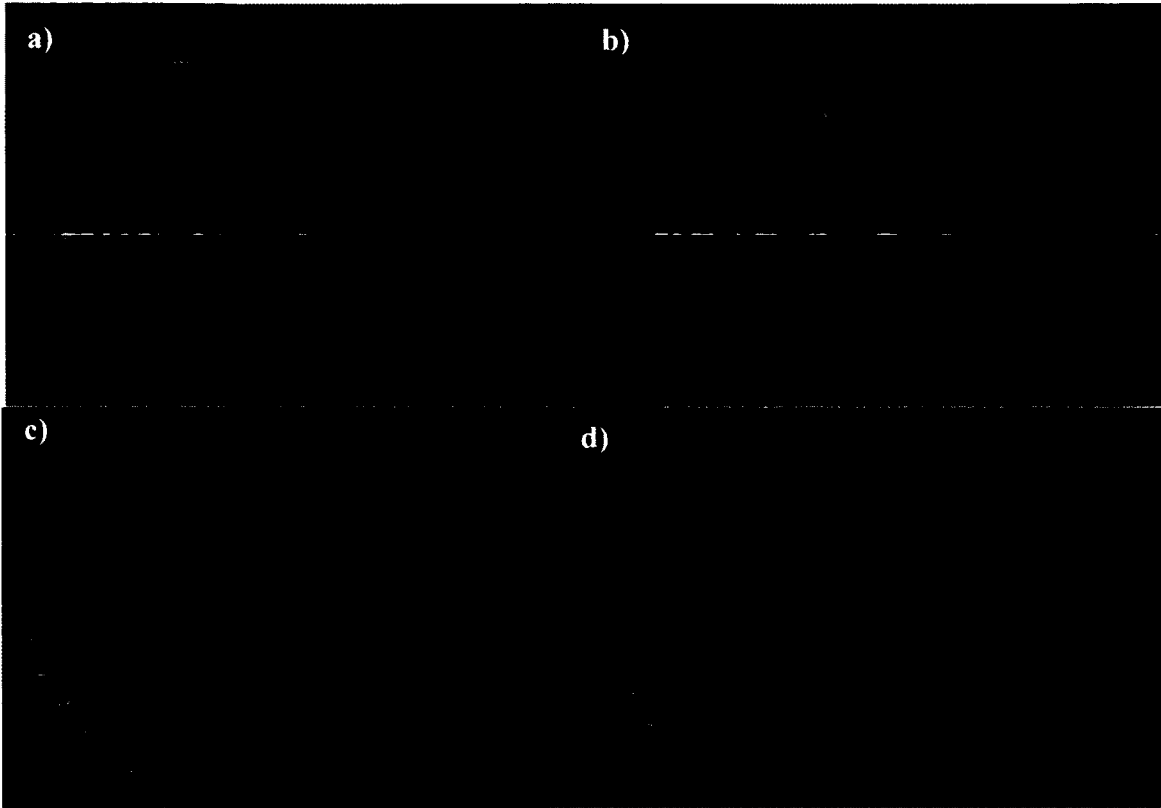
Figure 79. VR implementation of the force-deflection model the force applied to node 5125: a) F=0 N, b) F=300 N, c) F=1000 N, d) F=1700 N

These results show that it is possible to obtain real-time performance based on the approximation of the force-displacement model. However, the number of vertices in the model plays a crucial role affecting the performance. Incorporation of the skin model provides a natural surface to compare with the average model of the chest. Two scenarios, where the same force at different locations was applied, were compared one showing a near optimal result and one showing a suboptimal result. These results illustrate the range and flexibility of the simulator to serve both a planner and a trainer for the Nuss procedure.

CHAPTER 6

CONCLUSIONS AND RECOMMENDATIONS

The development and validation of a Nuss procedure planner is investigated in this dissertation, including the implementation and performance assessment of the key components of such a system. The main parts of this system is a force-deflection model for the sternum position prediction based on the location of a force which simulates the placement of the pectus bar, an average shape of the chest acting as the performance measure for both the real and virtual surgical outcome, and capabilities of real-time performance of the model for training purposes. Additionally, hardware setup components and ports to implement external devices, like haptic devices and trackers, into the system were presented.

The obtained average shape of the chest proved that the presented implementation of the common framework for processing surface scans is sufficient. Alternative methods for hole-filling and ensuring consistency among scans, which are the biggest challenges when surface scans are processed, were developed. The first problem was solved using a cross-section of scans with parallel planes and then sampling points from fitted polynomials. The solution to the second problem includes the creation of a surface interpolant for each dataset that allows controlling consistency among scans and their resolution.

The development of the force-deflection model was initiated with the creation of a generic model of the ribcage that is deformed based upon patient specific parameters. This method was used in order to overcome the issue of difficult to segment cartilage tissue. This generic model results in an approximation of the patient's ribcage.

Each patient specific model was converted to a FEM, and FEA was performed according to the Nuss procedure characteristics. Force-deflection data was used to train an artificial neural network. Results showed that the network can be generalized and given new locations and magnitudes of the pectus bar forces. However, these good results may be coming from the small variability in the dataset. Patient specific deformations were simplified by neglecting sternal torsion. In this way, the problem was reduced to the application of an appropriate scaling to the ribcage and the amount of depression. If more parameters are taken into account, the generic model cannot be easily deformed.

Comparison of the patient specific FE displacement and ANN approximation was performed by reformatting and collocating two types of models which is a slow and manual process. Automatic error calculation is needed in the future.

Another drawback of this method is the time needed to train an ANN. As the number of nodes increases so does the training time making the application of any changes to the network structure virtually impossible. Therefore, a hybrid model may be more appropriate. Force-deflection data from the FEA stage could be used to create an approximation of the relationship between load and displacement only for a small set of control points governing deformation of a geometric model similar to how deformations are currently applied to the generic model. Another solution to this problem would lay in segmentation of at least the ribcage and sternum and in the case of the missing cartilage it could be filled to create a more accurate patient specific model.

The validation methodology showed that it is possible to compare the simulated skin shape with the actual surface scan. However, due to patient growth between taking pre-surgical CT and the post-surgical surface scan, a scaling factor has to be applied.

Comparison of the simulated chest shape with an average shape chest showed that this method could be used to evaluate scenarios for the pectus bar placement. Although, it may never be possible to obtain results exactly matching an average shape chest, two or more scenarios can be reviewed and compared, not only in terms of the location of the bar but as well as forces that need to be applied to obtain the desired shape.

The application of the approximation of the force-deflection model to obtain real time deformation showed that a 20-30 Hz refresh rate can be obtained. However, when more models like internal organs and external devices, such as collision detection, a haptic device and a tracker, are added a decrease in the refresh rate should be expected. Improvement in the performance could be achieved by utilizing less detailed models, i.e. described by a smaller amount of vertices.

Additionally, hardware setup components have been presented. The custom made aluminum frame serves as the base for the hardware. The system allows connecting compatible Phantom haptic devices, and several inertial and visual trackers. A 3D TV ensures that the simulation can be viewed in 3D.

The author believes that with this dissertation he made the following contributions:

- A methodology to develop a Nuss procedure planner:
  - o A generic model of the ribcage which allows fast creation of the patient specific model. The model is deformed based on parameters obtained from CT data.

o An approximation of the force-displacement model using a black box approach. An ANN is trained using the force-displacement data obtained by applying FEA.

- A methodology to develop a Nuss procedure trainer:

  o Real-time deformations of the patient specific ribcage model based on the approximated force-displacement model was achieved.

  o A haptic and tracking device was incorporated into the Nuss procedure simulator. The haptic device controls surgical tools in the VR environment, whereas a tracking device provides control over the virtual thoracoscope.

- A methodology to evaluate results of the planning process and validate the Nuss procedure planner:

  o Development of an average shape chest was developed that allows objective evaluation of the results of the planning process. The difference between an average and simulated chest shape is presented in the form of a colormap.

  o A methodology to fill holes, recreate missing data, and assure consistency among surface scans was developed. The novelty lies in converting each shape in a sample to a set of polylines and using points which define their segments to fit a polynomial which is later used to sample points that result in consistent shape vectors representing each scan.

CHAPTER 7

FUTURE WORK

Further studies are needed to improve the performance of the presented solutions. A larger dataset of normal subject chest scans needs to be collected to provide a more accurate average shape chest.

In terms of the patient specific ribcage model, the attention should be put toward more direct methods like segmentation or hybrid geometrical-FE models. This step cannot be emphasized enough because an incorrect patient specific ribcage model can influence all other results.

In order to assess patient specificity, CT surface extraction to generate the average error between pre-surgical actual and simulated skin shape will need to be utilized. Additionally, automatic error calculation for comparison between the patient specific FEM deformed model and ANN approximated model will need to be implemented.

A long term study relating position of the bar to the shape of the chest is needed to fully validate the performance of the planner. This will include pre-operative surface scans, post-operative x-rays to obtain bar positions, post-operative surface scans and predicted shapes from the simulator. A scaling factor due to a patient's growth will also need to be applied.

Another very important region of further studies is the mechanical properties of the cartilage measured *in vivo*. Currently, the properties vary significantly within the literature making quantification of results difficult.

The main extension of this research will be the final prototype of the Nuss procedure planner and trainer, including the integrated hardware and software. It may be

beneficial to make the system independent from any commercially available VR development software providing more flexibility in incorporating various modules like haptics and tracking.

REFERENCES

[1] S. E. Pretorius, A. J. Haller, and E. K. Fishman, "Spiral CT with 3D Reconstruction in Children Requiring Reoperation for Failure of Chest Wall Growth after Pectus Excavatum Surgery," *Clinical Imaging,* vol. 22, pp. 108-116, 1998.

[2] A. D. Protopapas and T. Athanasiou, "Peri-operative data on the Nuss procedure in children with pectus excavatum: independent survey of the first 20 years' data," *Journal of Cardiothoracic Surgery,* vol. 40, 2008.

[3] D. Nuss, R. E. Kelly Jr, D. P. Croitoru, and M. E. Katz, "A 10-year review of a minimally invasive technique for the correction of pectus excavatum," *J Ped Surg,* vol. 33, pp. 545-52, 1998.

[4] D. L. Sigalet, M. Montgomery, and J. Harder, "Cardiopulmonary effects of closed repair of pectus excavatum," *J Ped Surg,* vol. 38, pp. 380-85, 2003.

[5] O. A. Bawazir, M. Montgomery, J. Harder, and ˙D. L. Sigalet, "Midterm evaluation of cardiopulmonary effects of closed repair for pectus excavatum," *J Ped Surg,* vol. 40, pp. 863-7, 2005.

[6] G. Krasopoulos, M. Dusmet, G. Ladas, and P. Goldstraw, "Nuss procedure improved the quality of life in young male adults with pectus excavatum deformity," *Eur J Cardio-thoracic Surg,* vol. 29, pp. 1-5, 2006.

[7] M. L. Lawson, T. F. Cash, R. Akers, E. Vasser, B. Burke, M. Tabangin, C. Welch, D. P. Croitoru, M. J. Goretsky, D. Nuss, and R. E. K. Jr., "A pilot study of the impact of surgical repair on disease-specific quality of life among patients with pectus excavatum," *J Ped Surg,* vol. 38, pp. 916-8, 2003.

[8] E. Einsiedel and A. Clausner, "Funnel chest. Psychological and psychosomatic aspects in children, youngsters, and young adults," *J Cardiovasc Surg,* vol. 40, pp. 733-736, 1999.

[9] *Pectus Deformities Support Group.* Available: http://www.pectusinfo.com

[10] H. Seo, F. Cordier, and K. Hong, "A breast modeler based on analysis of breast scans," *Computer Animation and Virtual Worlds,* vol. 18, pp. 141-151, 2007.

[11] T. Nagasao, J. Miyamoto, T. Tamaki, K. Ichihara, H. Jiang, T. Taguchi, R. Yozu, and T. Nakajima, "Stress distribution on the thorax after the Nuss procedure for pectus excavatum results in different patterns between adult and child patients," *J Thorac Cardiovasc Surg,* vol. 134, pp. 1502-1507, 2007.

[12] U. Obaidellah, Z. Radzi, N. A. Yahya, N. A. A. Osman, and A. F. Merican, "The Facial Soft Tissue Simulation of Orthognathic Surgery Using Biomechanical

Model " presented at the 4th Kuala Lumpur International Conference on Biomedical Engineering 2008, Kuala Lumpur, Malaysia, 2008.

[13]   J. Berkley, G. Turkiyyah, D. Berg, M. Ganter, and S. Weghorst, "Real-Time Finite Element Modeling for Surgery Simulation: An Application to Virtual Suturing," *IEEE Transactions on Visualization and Computer Graphics,* vol. 10, pp. 314-325, 2004.

[14]   D. R. Flum and T. Koepsell, "The Clinical and Economic Correlates of Misdiagnosed Appendicitis," *Arch Surg,* vol. 137, pp. 799-804, 2002.

[15]   L. Zamorano, F. C. Vinas, Z. Jiang, and F. G. Diaz, "Use of surgical wands in neurosurgery," in *Advances and Technical Standards in Neurosurgery.* vol. 24, F. Cohadon, V. V. Dolenc, J. L. Antunes, H. Nornes, J. D. Pickard, H. J. Reulen, A. J. Strong, N. D. Pribolet, and C. A. F. Tulleken, Eds., 1 ed: Springer, 1998, pp. 77-128.

[16]   R. B. Grant, "Outpatient surgery: helping to contain health care costs," *Monthly labor review / U.S. Department of Labor, Bureau of Labor Statistics,* vol. 115, pp. 33-6, Nov 1992.

[17]   V. V. Patel, M. W. Vannier, J. L. Marsh, and L. Lun-Jou, "Assessing craniofacial surgical simulation," *IEEE Computer Graphics and Applications,* vol. 16, pp. 46-54, 1996.

[18]   R. Sodian, S. Weber, M. Markert, D. Rassoulian, I. Kaczmarek, T. C. Lueth, B. Reichart, and S. Daebritz, "Stereolithographic Models for Surgical Planning in Congenital Heart Surgery," *Ann Thorac Surg,* vol. 83, pp. 1854-1857, 2007.

[19]   S. Weber, R. Sodian, M. Markert, B. Reichart, S. Daebritz, and T. C. Lueth, "3D printing of anatomical heart models for surgical planning in cardiac surgery," *Int J CARS,* vol. 2, pp. 171-173, 2007.

[20]   J. Poukens, J. Haex, and D. Riediger, "The use of rapid prototyping in the preoperative planning of distraction osteogenesis of the cranio-maxillofacial skeleton," *Comput Aided Surg,* vol. 8, pp. 146–154, 2003.

[21]   L. J. Lo, J. L. Marsh, V. V. Patel, and M. W. Vannier, "Craniofacial Surgical Simulation and Outcome Validation," in *2nd Congress of ISCAS (CAS'95),* Berlin, Germany, 1995.

[22]   U. Meier, O. López, C. Monserrat, M. C. Juan, and M. Alcañiz, "Real-time deformable models for surgery simulation: a survey," *Computer Methods and Programs in Biomedicine,* vol. 77, pp. 183-197, 2005.

[23]   K. Keeve, S. Girod, and B. Girod, "Craniofacial Surgery Simulation," *Proceedings of the 4th International Conference on Visualization in Biomedical Computing, Lecture Notes In Computer Science,* vol. 1131, pp. 541-546, 1996.

[24]   W. Lin and R. A. Robb, "Dynamic volume texture mapping and model deformation for visually realistic surgical simulation," *Stud Health Technol Inform*, vol. 62, pp. 198-204, 1999.

[25]   S. Misra, K. J. Macura, K. T. Ramesha, and A. M. Okamura, "The importance of organ geometry and boundary constrains for planning of medical interventions," *Medical Engineering & Physics*, vol. 31, pp. 195–206, 2009.

[26]   M. Bro-Nielsen, "Finite element modeling in surgery simulation," *Proc IEEE 1998*, vol. 86, pp. 490–503, 1998.

[27]   M. Cartoski, D. Nuss, M. Goretsky, V. Proud, D. Croitoru, T. Gustin, K. Mitchell, E. Vasser, and J. R. Kelly, "Classification of the dysmorphology of pectus excavatum," *J Ped Surg*, vol. 41, pp. 1573-81, 2006.

[28]   M. H. Malek, D. E. Berger, W. D. Marelich, J. W. Coburn, T. W. Beck, and T. J. Housh, "Pulmonary function following surgical repair of pectus excavatum: a metaanalysis," *Eur J Cardio-thoracic Surg*, vol. 30, pp. 637-643, 2006.

[29]   P. M. Quigley, J. A. H. Jr, K. L. Jelus, G. M. Loughlin, and C. L. Marcus, "Cardiorespiratory function before and after corrective surgery in pectus excavatum," *J Ped Surg*, vol. 128, pp. 638-43, 1996.

[30]   J. A. Haller and G. M. Loughlin, "Cardiorespiratory function is significantly improved following corrective surgery for severe pectus excavatum. Proposed treatment guidelines," *J Cardiovasc Surg*, vol. 41, pp. 125-30, 2000.

[31]   D. L. Sigalet, M. Montgomery, J. Harder, V. Wong, D. Kravarusic, and A. Alassiri, "Long term cardiopulmonary effects of closed repair of pectus excavatum," *Ped Surg Intl*, vol. 23, pp. 493-7, 2007.

[32]   *Aetna Inc. Clinical Policy Bulletin on Pectus Excavatum and Poland's Syndrome: Surgical   Correction.*   Available: http://www.aetna.com/cpb/medical/data/200_299/0272.html

[33]   J. A. Haller, L. R. Scherer, C.S.Turner, and P. M. Columbani, "Evolving management of pectus excavatum based on a single institutional experience of 664 patients," presented at the the 100th Annual Meeting of The Southern Surgical Association, Boca Raton, Florida, 1988.

[34]   J. Wada, K. Ikeda, T. Ishida, and T. Hasegawa, "Results of 271 funnel chest operations," *Ann Thor Surg*, vol. 10, pp. 526-532, 1970.

[35]   J. F. Murray, "Correction of pectus excavatum by synthetic subcutaneous implant," presented at the Annual Meeting of the American Society of Plastic and Reconstructive Surgeons, Philadelphia, 1965.

[36]   A. Margulis, M. Sela, R. Neuman, and A.Buller-Sharon, "Reconstruction of pectus excavatum with silicone implants," *J Plas Recon Aest Surg,* vol. 59, pp. 1082-6, 2006.

[37]   M. W. Marks and J. Iacobucci, "Reconstruction of congenital chest wall deformity using solid silicone onlay prostheses," *Chest Surg Clin N.A,* vol. 10, pp. 341- 355, 2000.

[38]   D. J. Hodgkinson, "Chest wall implants: Their use for pectus excavatum, pectoralis muscle tears, Poland's syndrome, and muscular insufficiency," *Aest Plas Surg,* vol. 21, pp. 7-15, 1997.

[39]   G. Wechselberger, M. Ohlbauer, J. Haslinger, T. Schoeller, T. Bauer, and H. Piza-Katzer, "Silicone implant correction pectus excavatum," *Ann Plas Surg,* vol. 47, pp. 489-93, 2001.

[40]   F. Schier, M.Bahr, and E. Klobe, "The vacuum chest wall lifter: An innovative, nonsurgical addition to the management of pectus excavatum," *J Ped Surg,* vol. 40, pp. 496-500, 2005.

[41]   F. M. Haecker and J. Mayr, "The vacuum bell for treatment of pectus excavatum: an alternative to surgical correction?," *Eur J Cardio-thoracic Surg,* vol. 29, pp. 557-61, 2006.

[42]   J. Bohosiewicz, G. Kudela, and U. Izwaryn, "The Nuss Procedure for the Correction of Pectus Excavatum," *Polish Journal of Surgery,* vol. 81, pp. 103-112, 2009.

[43]   M. L. Metzelder, J. F. Kuebler, J. Leonhardt, B. M. Ure, and C. Petersen, "Self and Parental Assessment After Minimally Invasive Repair of Pectus Excavatum: Lasting Satisfaction After Bar Removal," *Ann Thorac Surg,* vol. 83, pp. 1844-1849, 2007.

[44]   E. B. Rebeis, J. R. M. d. Campos, Â. Fernandez, L. F. P. Moreira, and F. B. Jatene, "Anthropometric index for Pectus excavatum," *Clinics,* vol. 62, pp. 599-606, 2007.

[45]   E. W. Fonkalsrud, "Current Management of Pectus Excavatum," *World J Surg,* vol. 27, pp. 502-08, 2003.

[46]   J. T. Davis and S. Weinstein, "Repair of the Pectus Deformity: Results of the Ravitch Approach in the Current Era," *Ann Thorac Surg,* vol. 78, pp. 421-26, 2004.

[47]   H. J. Park, S. Y. Lee, C. S. Lee *et al,* "The Nuss Procedure for Pectus Excavatum: Evolution of Techniques and Early Results on 322 Patients," *Ann Thorac Surg,* vol. 77, pp. 289-95, 2004.

[48] E. S. Boia, R. Susan-Resiga, P. C. Raicov, C. M. Popoiu, and R. E. I. RE, "Determination of the Mechanical Requirements for a Progressive Correction System of Pectus Excavatum in Children," *J Laparoendosc Adv Surg Tech A*, vol. 15, pp. 478-81, 2005.

[49] M. R. Harrison, D. Estefan-Ventura, R. Fechter, A. M. M. Jr, and D. Christensen, "Magnetic Mini-Mover Procedure for pectus excavatum I. Development, design, and simulations for feasibility and safety," *J Ped Surg*, vol. 42, pp. 81-86, 2007.

[50] E. P. Kavanagh, C. Frawley, G. Kearns, F. Wallis, T. McGloughlin, and J. Jarvis, "Use of finite element analysis in presurgical planning: treatment of mandibular fractures," *Ir J Med Sci*, vol. 177, pp. 325-31, 2008.

[51] G. S. Vicente, C. Buchart, D. Borro, and J. T. Celigüeta, "Maxillofacial surgery simulation using a mass-spring model derived from continuum and the scaled displacement method," *Int J CARS*, vol. 4, pp. 89-98, 2009.

[52] B. Lloyd, G. Székely, and M. Harders, "Identification of Spring Parameters for Deformable Object Simulation," *IEEE Transactions on Visualization and Computer Graphics*, vol. 13, pp. 1081-1094, 2007.

[53] G. Ridsdale, "Connectionist modelling of skill dynamics," *The Journal of Visualization and Computer Animation*, vol. 1, pp. 66-72, 1990.

[54] R. Grzeszczuk, D. Terzopoulos, and G. Hinton, "NeuroAnimator: fast neural network emulation and control of physics-based models," presented at the Proceedings of the 25th annual conference on Computer Graphics and Interactive Techniques, 1998.

[55] R. Grzeszczuk and D. Terzopoulos, "Automated learning of muscle-actuated locomotion through control abstraction," presented at the Proceedings of the 22nd annual conference on Computer graphics and interactive techniques, 1995.

[56] T. M. Cheng and C. C. Yang, "Virtual object deformations using attributed boundary model," presented at the IEEE International Conference on Automation Science and Engineering, Edmonton, Canada, 2005.

[57] T. M. Cheng and T. Tsung-Han, "A fast parametric deformation mechanism for virtual reality applications," *Computers & Industrial Engineering*, vol. 57, pp. 520-538, 2009.

[58] K. Morooka, X. Chen, R. Kurazume, S. Uchida, K. Hara, Y. Iwashita, and M. Hashizume, "Real-Time Nonlinear FEM with Neural Network for Simulating Soft Organ Model Deformation," *MICCAI 2008, Part II, Lecture Notes in Computer Science*, vol. 5242, pp. 742-749, 2008.

[59] P. Chang, Z. Hsu, D. Chen, J. Lai, and C. Wang, "Preliminary analysis of the forces on the thoracic cage of patients with pectus excavatum after the Nuss procedure," *Clinic Biomech,* vol. 23, pp. 881-885, 2008.

[60] B. Gzik-Zroska, D. Tejszerska, and W. Wolański, "Stress Analysis in Funnel Chest Stabilization with a Plate," *Modelowanie Inżynierskie,* vol. 34, pp. 37-42, 2007.

[61] J. Awrejcewicz and B. Łuczak, "The Finite Element Model of the Human Rib Cage," *J Theor Appl Mech,* vol. 45, pp. 25-32, 2007.

[62] Y. Wei, Y. Shi, H. Wang, and Y. Gao, "Simulation of Nuss Orthopedic for Pectus Excavatum," in *Biomedical Engineering and Informatics, 2009. BMEI '09. 2nd International Conference on,* 2009, pp. 1-4.

[63] D. Kopperdahl, E. Morgan, and T. Keaveny, "Quantitative computed tomography estimates of the mechanical properties of human vertebral trabecular bone," *Orthop Res,* vol. 20, pp. 801-805, 2002.

[64] J. Feng, T. Hu, W. Liu, S. Zhang, Y. Tang, R. Chen, X. Jiang, and F. Wei, "The biomechanical, morphologic, and histochemical properties of the costal cartilages in children with pectus excavatum," *J Ped Surg,* vol. 36, pp. 1770-1776, 2001.

[65] W. Wang, Y. Shi, H. Wang, and L. Yin, "Research on Biomechanical Model of Children with Pectus Excavatum," in *Biomedical Engineering and Informatics, 2009. BMEI '09. 2nd International Conference on,* 2009, pp. 1-4.

[66] V. Blanz and T. Vetter, "A Morphable Model for the Synthesis of 3D Faces," in *Proceedings of the 26th Annual Conference on Computer Graphics SIGGRAPH '99,* Los Angeles, California, USA, 1999, pp. 187-194.

[67] B. Allen, B. Curless, and Z. Popovic, "The space of human bodyshapes: reconstruction and parametrization from range scans," in *Proceedings of ACM SIGGRAPH,* San Diego, California, 2003, pp. 587-594.

[68] Z. B. Azouz, M. Rioux, C. Shu, and R. Lepage, "Characterizing Human Shape Variation Using 3-D Anthropometric Data," *The Visual Computer International Journal of Computer Graphics,* vol. 22, pp. 302-314, 2005.

[69] H. Seo and N. Magnenat-Thalmann, "An Automatic modeling of human bodies from sizing parameters," in *Proceedings of the 2003 symposium on Interactive 3D graphics,* Monterey, California, 2003, pp. 19-26.

[70] Y. Kim, K. Lee, and W. Kim, "3D virtual simulator for breast plastic surgery," *Computer Animation and Virtual Worlds,* vol. 19, pp. 515-526, 2008.

[71] P. Xi, W.S. Lee, and C. Shu, "Analysis of Segmented Human Body Scans," in *Graphics Interface Conference 2007,* Montréal, Canada, 2007, pp. 19-26.

[72]   K. J. Rechowicz, R. Kelly, M. Goretsky, F. W. Frantz, S. B. Knisley, D. Nuss, and F. D. McKenzie, "A Design for Simulating and Validating the Nuss Procedure for the Minimally Invasive Correction of Pectus Excavatum," in *Proceedings of Medicine Meets Virtual Reality 18*, Newport Beach, 2011.

[73]   R. E. Redlinger, Jr., D. Nuss, A. Quinn, E. McGuire, and R. Kelly, "Frequency distribution of dysmorphology of pectus excavatum," presented at the BAPS 2011 International Congress, Belfast, 2011.

[74]   S. Osowski, *Sieci neuronowe do przetwarzania informacji*, 1 ed. Warsaw: Oficyna Wydawnicza PW, 2000.

[75]   K. J. Rechowicz, R. Kelly, M. Goretsky, F. Frantz, S. Knisley, D. Nuss, and F. D. McKenzie, "Development of an average chest shape for objective evaluation of the aesthetic outcome in the Nuss procedure planning process," in *Proceedings of Southern Biomedical Engineering Conference*, College Park, MD, USA, 2010.

[76]   K. Rechowicz, F. McKenzie, Z. Yan, S. Bawab, and S. Ringleb, "Investigating an approach to identifying the biomechanical differences between intercostal cartilage in subjects with pectus excavatum and normals in vivo: preliminary assessment of normal subjects," in *Proceedings of SPIE Medical Imaging 2009 Conference*, Orlando, Florida, USA, 2009.

APPENDICES

APPENDIX A: PATIENTS' PARAMETERS

Table 3. Patient specific parameters.

No.	Haller Index	Width [mm]	Length [mm]	Depth [mm]	Depression [mm]
1	4.3	232	180	126	14
2	4.3	283	145	153	25
3	6.3	280	165	151	40
4	2.69	225	120	144	13
5	4.2	225	144	120	34
6	3.89	253	136	138	5
7	4.6	239	165	140	33
8	3.7	265	170	150	15
9	4.9	265	176	140	20
10	4	245	140	141	34
11	4	227	144	142	18
12	3.55	236	155	126	14
13	3.4	252	168	140	27
14	3.86	247	184	143	26
15	3.47	229	112	138	10
16	4.7	291	168	142	20
17	3.5	245	160	144	22
18	3.41	236	152	141	30
19	3.6	238	160	130	15
20	4.9	304	180	150	30
21	3.3	269	155	169	16
22	5	248	176	131	20
23	4.8	247	141	136	24
24	4.7	265	152	143	22
25	3.9	252	142	145	15
26	3.2	203	111	116	15
27	4	224	100	130	17
28	4.2	271	185	143	15
29	3.2	254	152	166	18
30	3.8	275	184	160	22
31	6.18	273	170	127	33
32	3.7	261	147	168	24
33	3.6	241	136	146	25
34	5.1	247	144	129	13
35	5.6	271	160	128	18

36	3.5	290	165	156	22
37	4.2	253	176	137	22
38	3.9	232	125	130	8
39	3.6	216	115	128	17
40	3.8	258	140	144	5
41	3.2	255	152	166	18
42	3.8	217	144.4	137	16
43	3.4	203	93	137	15
44	3	229	136	149	16
45	4.9	260	175	137	21
46	3.7	254	155	142	10
47	5	266	150	164	30
48	5.7	269	140	132	0
49	4	290	184	155	15
50	3.1	265	168	162	15
51	4.4	255	168	135	12
52	3.29	263	168	168	14
53	3.5	222	128	113	5
54	3.3	252	162	142	9
55	4	266	168	140	7
56	4.6	261	152	144	13
57	6.5	231	168	123	21
58	2.8	238	168	150	15
59	3.1	274	152	169	2
60	4.1	295	168	147	15
61	3.5	262	162	152	18
62	4.5	245	120	137	24

APPENDIX B: PERMISSIONS TO REUSE FIGURES

New Text Document.txt

Thesis / Dissertaion Reuse

The IEEE does not require individuals working on a thesis to obtain a formal reuse license, however, you may print out this statement to be used as a permission grant:

Requirements to be followed when using any portion (e.g., figure, graph, table, or textual material) of an IEEE copyrighted paper in a thesis:

1) In the case of textual material (e.g., using short quotes or referring to the work within these papers) users must give full credit to the original source (author, paper, publication) followed by the IEEE copyright line © 2011 IEEE.
2) In the case of illustrations or tabular material, we require that the copyright line © [Year of original publication] IEEE appear prominently with each reprinted figure and/or table.
3) If a substantial portion of the original paper is to be used, and if you are not the senior author, also obtain the senior author's approval.

Requirements to be followed when using an entire IEEE copyrighted paper in a thesis:

1) The following IEEE copyright/ credit notice should be placed prominently in the references: © [year of original publication] IEEE. Reprinted, with permission, from [author names, paper title, IEEE publication title, and month/year of publication]
2) Only the accepted version of an IEEE copyrighted paper can be used when posting the paper or your thesis on-line.
3) In placing the thesis on the author's university website, please display the following message in a prominent place on the website: In reference to IEEE copyrighted material which is used with permission in this thesis, the IEEE does not endorse any of [university/educational entity's name goes here]'s products or services. Internal or personal use of this material is permitted. If interested in reprinting/republishing IEEE copyrighted material for advertising or promotional purposes or for creating new collective works for resale or redistribution, please go to http://www.ieee.org/publications_standards/publications/rights/rights_link.html to learn how to obtain a License from RightsLink.

If applicable, University Microfilms and/or ProQuest Library, or the Archives of Canada may supply single copies of the dissertation.

Gmail

Permission to reuse a figure in a dissertation

Xi, Pengcheng <Pengcheng.Xi@nrc-cnrc.gc.ca>   **Wed, Feb 15, 2012 at 10:17 AM**
To "Krzysztof J. Rechowicz" <krech001@odu edu>

Good morning

Please go ahead to use the image you need for your dissertation and make sure you put the right reference for it.

Cheers

Pengcheng Xi

From: k.rechowicz@gmail.com [mailto:k.rechowicz@gmail.com] **On Behalf Of** Krzysztof J. Rechowicz
Sent: Monday, February 13, 2012 5 20 PM
To: Xi, Pengcheng
Subject: Permission to reuse a figure in a dissertation

Dear Sir

I have contacted ACM to ask for permission to reuse an image in my dissertation from the following paper
P Xi W-S Lee and C Shu, "Analysis of Segmented Human Body Scans," in *Graphics Interface Conference*
2007, Montreal Canada 2007 pp 19-26

However I was informed that ACM does not posses any copyrights to that material as shown below I was
advised to contact one of the authors Therefore I would like to kindly ask for a permission to use a figure
from that particular paper in my dissertation

Thank you in advance for your support

Krzysztof Rechowicz
Old Dominion University

　　　　Forwarded message
From **ACM Permissions** <permissions@hq acm org>
Date Mon Feb 13, 2012 at 4 18 PM
Subject RE Permission to reuse a figure in a dissertation
To "Krzysztof J Rechowicz" <krech001@odu edu>

Hello

Thank you for your inquiry. According to our records, ACM published the 2007 Graphics Interface Conference proceedings by agreement with the sponsor, but the authors retained copyright to their contributions, outside of ACM's normal procedure.

You should try contacting the authors directly for permission. Unfortunately, I can only provide their last known email addresses according to the published paper. Good luck.

Pengcheng Xi

National Research Council of Canada

Ottawa, Ontario, Canada

pengcheng.xi@nrc-cnrc.gc.ca

Won-Sook Lee

University of Ottawa

Ottawa, Ontario, Canada

wslee@uottawa.ca

Chang Shu

National Research Council of Canada

Ottawa, Ontario, Canada

chang.shu@nrc-cnrc.gc.ca

Regards

Deborah Cotton

Copyright & Permissions

ACM Publications

212 626 0652

cotton@hq.acm.org

From: k.rechowicz@gmail.com [mailto:k.rechowicz@gmail.com] **On Behalf Of** Krzysztof J. Rechowicz
Sent: Monday, February 13, 2012 3:55 PM
To: permissions@acm.org
Subject: Permission to reuse a figure in a dissertation

Dear Sir or Madam

I have been trying to find a link in ACM digital library to request a permission to reuse in my dissertation a figure from the following paper

P. X. W.-S. Lee and C. Shu "Analysis of Segmented Human Body Scans," in *Graphics Interface Conference* 2007 Montreal Canada 2007, pp. 19-26

I saw that these particular conference proceedings are listed by http://www.copyright.com but still it is impossible to request a permission to reuse that particular figure

I would like to ask for the assistance in obtaining that permission

Thank you

Krzysztof Rechowicz
Old Dominion University

Spam
Not spam
Forget previous vote

Spam
Not spam
Forget previous vote

TERMS AND CONDITIONS

Feb 13, 2012

This is a License Agreement between Krzysztof J Rechowicz ("You") and John Wiley and Sons ("John Wiley and Sons") provided by Copyright Clearance Center ("CCC"). The license consists of your order details, the terms and conditions provided by John Wiley and Sons, and the payment terms and conditions.

All payments must be made in full to CCC. For payment instructions, please see information listed at the bottom of this form.

License Number	2847211355021
License date	Feb 13, 2012
Licensed content publisher	John Wiley and Sons
Licensed content publication	Computer Animation & Virtual Worlds
Licensed content title	A breast modeler based on analysis of breast scans
Licensed content author	Hyewon Seo, Frederic Cordier & Junghi Hong
Licensed content date	May 1, 2007
Start page	141
End page	151
Type of use	Dissertation/Thesis
Requestor type	University/Academic
Format	Print and electronic
Portion	Figure/table
Number of figures/tables	1
Number of extracts	
Original Wiley figure/table number(s)	Figure 1
Will you be translating?	No
Order reference number	
Total	0.00 USD

SPRINGER LICENSE
TERMS AND CONDITIONS

Feb 13, 2012

This is a License Agreement between Krzysztof J Rechowicz ("You") and Springer ("Springer") provided by Copyright Clearance Center ("CCC"). The license consists of your order details, the terms and conditions provided by Springer, and the payment terms and conditions.

All payments must be made in full to CCC. For payment instructions, please see information listed at the bottom of this form.

License Number	2847201262872
License date	Feb 13, 2012
Licensed content publisher	Springer
Licensed content publication	Springer eBook
Licensed content title	The Facial Soft Tissue Simulation of Orthograthic Surgery using Biomechanical Model
Licensed content author	Unaizah Obaidellah
Licensed content date	Jan 1, 2008
Type of use	Thesis/Dissertation
Portion	Figures
Author of this Springer article	No
Order reference number	
Title of your thesis / dissertation	Development and Validation of the Nuss Procedure Surgical Planner
Expected completion date	Aug 2012
Estimated size(pages)	200
Total	0.00 USD
Terms and Conditions	

If you would like to pay for this license now, please remit this license along with your payment made payable to "COPYRIGHT CLEARANCE CENTER" otherwise you will be invoiced within 48 hours of the license date. Payment should be in the form of a check or money order referencing your account number and this invoice number RLNK500718157.
Once you receive your invoice for this order, you may pay your invoice by credit card. Please follow instructions provided at that time.

Make Payment To:
Copyright Clearance Center
Dept 001
P.O. Box 843006
Boston, MA 02284-3006

ELSEVIER LICENSE
TERMS AND CONDITIONS

Feb 13, 2012

This is a License Agreement between Krzysztof J Rechowicz ("You") and Elsevier ("Elsevier") provided by Copyright Clearance Center ("CCC"). The license consists of your order details, the terms and conditions provided by Elsevier, and the payment terms and conditions.

All payments must be made in full to CCC. For payment instructions, please see information listed at the bottom of this form.

Supplier	Elsevier Limited
	The Boulevard,Langford Lane
	Kidlington,Oxford,OX5 1GB,UK
Registered Company Number	1982084
Customer name	Krzysztof J Rechowicz
Customer address	1104 ECSB
	Norfolk, VA 23529
License number	2847210732428
License date	Feb 13, 2012
Licensed content publisher	Elsevier
Licensed content publication	The Journal of Thoracic and Cardiovascular Surgery
Licensed content title	Stress distribution on the thorax after the Nuss procedure for pectus excavatum results in different patterns between adult and child patients
Licensed content author	Tomohisa Nagasao,Junpei Miyamoto,Tamotsu Tamaki,Kazuhiko Ichihara,Hua Jiang,Toshihiko Taguchi,Ryohei Yozu,Tatsuo Nakajima
Licensed content date	December 2007
Licensed content volume number	134
Licensed content issue number	6
Number of pages	6
Start Page	1502
End Page	1507
Type of Use	reuse in a thesis/dissertation
Intended publisher of new work	other
Portion	figures/tables/illustrations
Number of figures/tables /illustrations	1

Format	both print and electronic
Are you the author of this Elsevier article?	No
Will you be translating?	No
Order reference number	
Title of your thesis/dissertation	Development and Validation of the Nuss Procedure Surgical Planner
Expected completion date	Aug 2012
Estimated size (number of pages)	200
Elsevier VAT number	GB 494 6272 12
Permissions price	0.00 USD
VAT/Local Sales Tax	0.0 USD / 0.0 GBP
Total	0.00 USD
Terms and Conditions	

INTRODUCTION

1. The publisher for this copyrighted material is Elsevier. By clicking "accept" in connection with completing this licensing transaction, you agree that the following terms and conditions apply to this transaction (along with the Billing and Payment terms and conditions established by Copyright Clearance Center, Inc. ("CCC"), at the time that you opened your Rightslink account and that are available at any time at http://myaccount.copyright.com)

GENERAL TERMS

2. Elsevier hereby grants you permission to reproduce the aforementioned material subject to the terms and conditions indicated

3. Acknowledgement: If any part of the material to be used (for example, figures) has appeared in our publication with credit or acknowledgement to another source, permission must also be sought from that source. If such permission is not obtained then that material may not be included in your publication/copies. Suitable acknowledgement to the source must be made, either as a footnote or in a reference list at the end of your publication, as follows

"Reprinted from Publication title, Vol/edition number, Author(s), Title of article/title of chapter, Pages No., Copyright (Year), with permission from Elsevier [OR APPLICABLE SOCIETY COPYRIGHT OWNER]." Also Lancet special credit - "Reprinted from The Lancet, Vol number, Author(s), Title of article, Pages No., Copyright (Year), with permission from Elsevier"

4. Reproduction of this material is confined to the purpose and/or media for which permission is hereby given

SPRINGER LICENSE
TERMS AND CONDITIONS

Feb 13, 2012

This is a License Agreement between Krzysztof J Rechowicz ("You") and Springer ("Springer") provided by Copyright Clearance Center ("CCC"). The license consists of your order details, the terms and conditions provided by Springer, and the payment terms and conditions

All payments must be made in full to CCC. For payment instructions, please see information listed at the bottom of this form.

License Number	2847200589392
License date	Feb 13, 2012
Licensed content publisher	Springer
Licensed content publication	International Journal of Computer Assisted Radiology and Surgery
Licensed content title	Maxillofacial surgery simulation using a mass-spring model derived from continuum and the scaled displacement method
Licensed content author	G San Vicente
Licensed content date	Jan 1, 2009
Volume number	4
Issue number	1
Type of use	Thesis/Dissertation
Portion	Figures
Author of this Springer article	No
Order reference number	
Title of your thesis / dissertation	Development and Validation of the Nuss Procedure Surgical Planner
Expected completion date	Aug 2012
Estimated size(pages)	200
Total	0.00 USD

Terms and Conditions

If you would like to pay for this license now, please remit this license along with your payment made payable to "COPYRIGHT CLEARANCE CENTER" otherwise you will be invoiced within 48 hours of the license date. Payment should be in the form of a check or money order referencing your account number and this invoice number RLNK500718145.
Once you receive your invoice for this order, you may pay your invoice by credit card. Please follow instructions provided at that time.

Make Payment To:
Copyright Clearance Center

ELSEVIER LICENSE
TERMS AND CONDITIONS

Feb 13, 2012

This is a License Agreement between Krzysztof J Rechowicz ("You") and Elsevier
("Elsevier") provided by Copyright Clearance Center ("CCC"). The license consists of your
order details, the terms and conditions provided by Elsevier, and the payment terms and
conditions.

**All payments must be made in full to CCC. For payment instructions, please see
information listed at the bottom of this form.**

Supplier	Elsevier Limited
	The Boulevard,Langford Lane
	Kidlington Oxford,OX5 1GB,UK
Registered Company Number	1982084
Customer name	Krzysztof J Rechowicz
Customer address	1104 ECSB
	Norfolk, VA 23529
License number	2847191365397
License date	Feb 13, 2012
Licensed content publisher	Elsevier
Licensed content publication	Journal of Pediatric Surgery
Licensed content title	A 10-year review of a minimally invasive technique for the correction of pectus excavatum
Licensed content author	Donald Nuss,Robert E Kelly,Daniel P Croitoru,Michael E Katz
Licensed content date	April 1998
Licensed content volume number	33
Licensed content issue number	4
Number of pages	8
Start Page	545
End Page	552
Type of Use	reuse in a thesis/dissertation
Portion	figures/tables/illustrations
Number of figures/tables/illustrations	1
Format	both print and electronic
Are you the author of this Elsevier article?	No

Will you be translating?	No
Order reference number	
Title of your thesis/dissertation	Development and Validation of the Nuss Procedure Surgical Planner
Expected completion date	Aug 2012
Estimated size (number of pages)	200
Elsevier VAT number	GB 494 6272 12
Permissions price	0.00 USD
VAT/Local Sales Tax	0.0 USD / 0.0 GBP
Total	0.00 USD
Terms and Conditions	

INTRODUCTION

1. The publisher for this copyrighted material is Elsevier. By clicking "accept" in connection with completing this licensing transaction, you agree that the following terms and conditions apply to this transaction (along with the Billing and Payment terms and conditions established by Copyright Clearance Center, Inc. ("CCC"), at the time that you opened your Rightslink account and that are available at any time at http://myaccount.copyright.com).

GENERAL TERMS

2. Elsevier hereby grants you permission to reproduce the aforementioned material subject to the terms and conditions indicated.

3. Acknowledgement: If any part of the material to be used (for example, figures) has appeared in our publication with credit or acknowledgement to another source, permission must also be sought from that source. If such permission is not obtained then that material may not be included in your publication/copies. Suitable acknowledgement to the source must be made, either as a footnote or in a reference list at the end of your publication, as follows:

"Reprinted from Publication title, Vol/edition number, Author(s), Title of article/title of chapter, Pages No., Copyright (Year), with permission from Elsevier [OR APPLICABLE SOCIETY COPYRIGHT OWNER]." Also Lancet special credit - "Reprinted from The Lancet, Vol number, Author(s), Title of article, Pages No., Copyright (Year), with permission from Elsevier."

4. Reproduction of this material is confined to the purpose and/or media for which permission is hereby given.

5. Altering/Modifying Material: Not Permitted. However figures and illustrations may be altered/adapted minimally to serve your work. Any other abbreviations, additions, deletions

SPRINGER LICENSE
TERMS AND CONDITIONS

Jun 26, 2012

This is a License Agreement between Krzysztof J Rechowicz ("You") and Springer ("Springer") provided by Copyright Clearance Center ("CCC"). The license consists of your order details, the terms and conditions provided by Springer, and the payment terms and conditions.

All payments must be made in full to CCC. For payment instructions, please see information listed at the bottom of this form.

License Number	2936780908710
License date	Jun 26, 2012
Licensed content publisher	Springer
Licensed content publication	Springer eBook
Licensed content title	Development of an Average Chest Shape for Objective Evaluation of the Aesthetic Outcome in the Nuss Procedure Planning Process
Licensed content author	K. J. Rechowicz
Licensed content date	Jan 1, 2010
Type of Use	Thesis/Dissertation
Portion	Figures
Author of this Springer article	Yes and you are the sole author of the new work
Order reference number	
Title of your thesis / dissertation	Development and Validation of the Nuss Procedure Surgical Planner
Expected completion date	Aug 2012
Estimated size(pages)	200
Total	0.00 USD
Terms and Conditions	

VITA

Krzysztof Jakub Rechowicz

Modeling, Simulation and Visualization Engineering Department

Old Dominion University

Norfolk, VA 23529

Educational Background

Ph.D.   : August 2012, Old Dominion University, Norfolk, VA, USA
Major   : Modeling and Simulation
Dissertation   : Development and Validation of the Nuss Procedure Surgical Planner

M.Sc.   : January 2006, Warsaw University of Technology, Warsaw, Poland
Major   : Production Engineering
Thesis   : Manufacturing Accuracy of SLA Prototypes with Application of Neural Networks

Major Publications

[1] K. J. Rechowicz, R. Kelly, M. Goretsky, F. W. Frantz, S. B. Knisley, D. Nuss, and F. D. McKenzie, "A Design for Simulating and Validating the Nuss Procedure for the Minimally Invasive Correction of Pectus Excavatum," in *Proceedings of Medicine Meets Virtual Reality 18*, Newport Beach, 2011.

[2] K. J. Rechowicz and F. D. McKenzie, "A strategy for simulating and validating the Nuss procedure for the minimally invasive correction of pectus excavatum," in *Biomedical Engineering and Informatics (BMEI), 2011 4th International Conference on*, 2011, pp. 2370-2374.

[3] K. J. Rechowicz, R. Kelly, M. Goretsky, F. Frantz, S. Knisley, D. Nuss, and F. D. McKenzie, "Development of an average chest shape for objective evaluation of the aesthetic outcome in the Nuss procedure planning process," in *Proceedings of Southern Biomedical Engineering Conference*, College Park, MD, USA, 2010.

[4] K. J. Rechowicz, F. D. McKenzie, S. Y. Bawab, and R. Obermeyer, "Application of CAD Analysis to Update the Design for a Pectus Excavatum Bar Extraction Tool," *Computer-Aided Design and Applications*, vol. 9, pp. 227-234, 2012.